

The JCMT Gould Belt Survey Complete Core Catalogue: Core mass function variations between nearby molecular clouds

Kate Pattle,^{1,2,3}★ James Di Francesco,^{4,5} Jenny Hatchell,⁶ Helen Kirk,^{4,5} Sarah Sadavoy,⁷ Derek Ward-Thompson,⁸ Doug Johnstone,^{4,5} Sammohith Nittala,^{9,4} Ronan Kerr,^{10,4} Jared Keown,^{4,5} Harold Butner,¹¹ Simon Coudé,^{12,13} Malcolm Currie,^{14,15} Rachel Friesen,¹⁰ Tim Jenness,^{17,15} Lewis Knee,⁴ and Glenn White^{18,14}

¹Department of Physics and Astronomy, University College London, Gower Street, London WC1E 6BT, UK

²Institute of Astronomy, Department of Physics, National Tsing Hua University, Guangfu Road, Hsinchu 30013, Taiwan

³Centre for Astronomy, School of Natural Sciences, University of Galway, University Road, Galway H91 TK33, Ireland

⁴NRC Herzberg Astronomy and Astrophysics Research Centre, 5071 West Saanich Road, Victoria, BC V9E 2E7, Canada

⁵Department of Physics and Astronomy, University of Victoria, 3800 Finnerty Road, Victoria, BC, V8P 5C2, Canada

⁶Physics and Astronomy, University of Exeter, Stocker Road, Exeter EX4 4QL, UK

⁷Department of Physics, Engineering Physics and Astronomy, Queens University, Kingston, ON, K7L 3N6, Canada

⁸Jeremiah Horrocks Institute, University of Lancashire, Preston PR1 2HE, UK

⁹Center for the Physics of Materials, Department of Physics, McGill University, 3600 Rue University, Montreal, QC, H3A 2T8, Canada

¹⁰Dunlap Institute for Astronomy & Astrophysics, University of Toronto, Toronto, ON M5S 3H4, Canada

¹¹Department of Physics and Astronomy, James Madison University, MSC 4502, 901 Carrier Drive, Harrisonburg, Virginia 22807, USA

¹²Department of Earth, Environment, and Physics, Worcester State University, Worcester, MA 01602, USA

¹³Center for Astrophysics | Harvard & Smithsonian, 60 Garden Street, Cambridge, MA 02138, USA

¹⁴RAL Space, Rutherford Appleton Laboratory, Harwell Campus, Didcot, Oxfordshire, OX11 0QX, UK

¹⁵East Asian Observatory, 660 N. A'ohōkū Place, University Park, Hilo, HI 96720, USA

¹⁶Vera C. Rubin Observatory, 950 North Cherry Avenue, Tucson, AZ 85719, USA

¹⁷Department of Physical Sciences, The Open University, Milton Keynes MK7 6AA, UK

Accepted XXX. Received YYY; in original form ZZZ

ABSTRACT

We present a catalogue of dense cores identified in James Clerk Maxwell Telescope (JCMT) Gould Belt Survey SCUBA-2 observations of nearby star-forming clouds. We identified 2257 dense cores using the *getsources* algorithm, of which 59% are starless, and 41% are potentially protostellar. 71% of the starless cores are prestellar core candidates, suggesting a prestellar core lifetime similar to that of Class 0/I YSOs. Higher-mass clouds have a higher fraction of prestellar cores compared to protostars, suggesting a longer average prestellar core lifetime. We assessed completeness by inserting critically-stable Bonnor–Ebert spheres into a blank SCUBA-2 field: completeness scales as distance squared, with an average mass recovery fraction of $73 \pm 6\%$ for recovered sources. We calculated core masses and radii, and assessed their gravitational stability using the Bonnor–Ebert criterion. Maximum starless core mass scales with cloud complex mass with an index 0.58 ± 0.13 , consistent with the behaviour of maximum stellar masses in embedded clusters. We performed least-squares and Monte Carlo modelling of the core mass functions (CMFs) of our starless and prestellar core samples. The CMFs can be characterised using log-normal distributions: we do not sample the full range of core masses needed to create the stellar Initial Mass Function (IMF). The CMFs of the clouds are not consistent with being drawn from a single underlying distribution. The peak mass of the starless core CMF increases with cloud mass; the prestellar CMF of the more distant clouds has a peak mass $\sim 3\times$ the log-normal peak for the system IMF, implying a $\sim 33\%$ prestellar core-to-star efficiency.

Key words: stars: formation – submillimetre: ISM – ISM: clouds – catalogues – surveys

1 INTRODUCTION

This paper presents a catalogue of cores identified from the Submillimetre Common-User Bolometer Array 2 (SCUBA-2; [Holland et al. 2013](#)) 850 μm and 450 μm data taken by the James Clerk

Maxwell Telescope (JCMT) Gould Belt Survey (GBS), a JCMT Legacy Program designed to map across regions of high extinction in 13 star-forming molecular clouds within 500 pc distance that are visible from Maunakea, Hawai‘i. The JCMT GBS was first presented to the community in an overview paper by [Ward-Thompson et al. \(2007\)](#). Since then, several papers have presented results from the Heterodyne Array Receiver Program (HARP; [Buckle et al. 2009](#))

★ E-mail: k.pattle@ucl.ac.uk

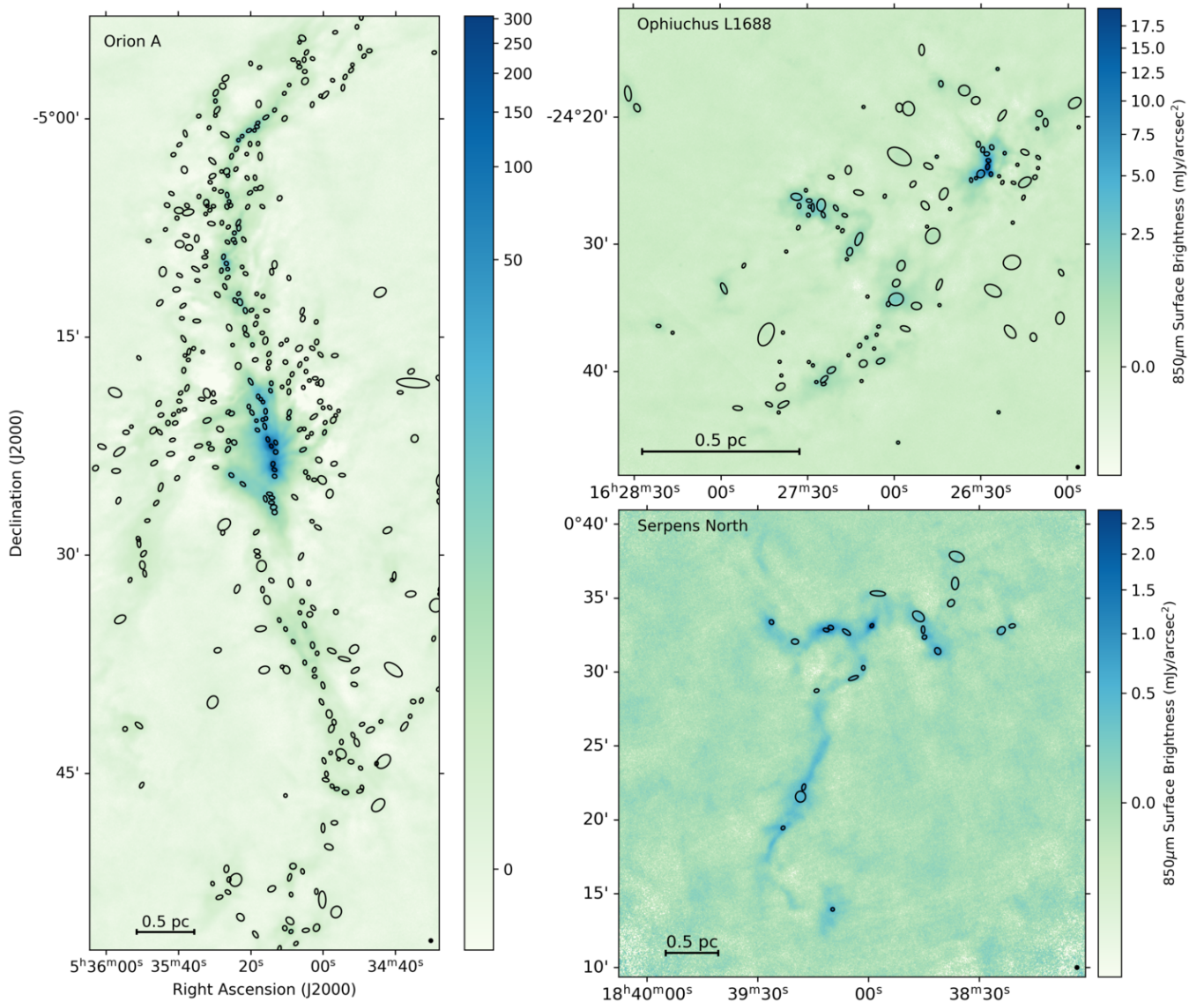


Figure 1. Extracts from three of the regions which we observed with SCUBA-2 as part of the JCMT Gould Belt Survey: the Integral Filament in Orion A (left), the L1688 region of the Ophiuchus Molecular Cloud (top right), and the Serpens North region (bottom right). Each panel shows SCUBA-2 850 μm emission, fourth-root scaled in the case of Orion A, and cube-root scaled for the other regions. Cores identified in our catalogue are marked with black ellipses, with ellipse diameter marking the FWHM size of the core. A 0.5 pc scale bar is shown in the lower left-hand corner of each panel; the JCMT 850 μm beam size is shown as a filled black circle in the lower right-hand corner. The full set of regions observed are shown in Appendix A.

and SCUBA-2 components of the GBS (see Table 1 for references). The GBS originally had a planned polarimetric mapping component, which due to the delayed commissioning of SCUBA-2’s POL-2 polarimeter (Friberg et al. 2016) instead became the basis for the JCMT B-Fields in Star-forming Region Observations (BISTRO; Ward-Thompson et al. 2017) Survey. In this current paper, we examine the GBS SCUBA-2 data for all of the target clouds, to identify the cores within them in a self-consistent way.

Cores are the interface between larger molecular clouds and the star formation within them. Physically, they are compact locations of high gas and dust density in clouds. Functionally, they have been identified from observations of the optically thin millimetre/submillimetre continuum emission from dust (e.g. Ladd et al. 1991) or specific, largely optically thin, line emission of molecules excited at moderate densities (e.g., 10^4 cm^{-3} or higher) that are still abundant in

cold ($\sim 10 \text{ K}$), dense environments (e.g. Benson & Myers 1989). In these investigations, locally bright emission is considered to indicate the presence of a locally dense configuration of gas and dust. Cores can therefore teach us about the star-formation process, as gas and dust can be accumulated within them to a point where they collapse from their own gravity to form young stellar objects (YSOs), which themselves eventually become stars. Those cores without YSOs are named “starless cores” (Benson & Myers 1989) and the subset of these that appear to be gravitationally bound are named “prestellar cores” (Ward-Thompson et al. 1994). Meanwhile, those with YSOs are named “protostellar cores”, with the detected mass comprising the extended envelopes of the embedded Class 0 or I YSOs (see Di Francesco et al. 2007; Ward-Thompson et al. 2007; André et al. 2014, for reviews).

A robust catalogue of cores within a star-forming cloud can be use-

ful because it provides the locations of objects with which further, more detailed investigations of ongoing star formation can be performed, e.g., examinations of the internal physical or chemical structures of specific cores. Such catalogues are also useful for identifying the populations of cores, i.e., snapshots of the current star-forming activity in various clouds. Moreover, comparing core populations between clouds of different character (e.g., mass, temperature, dense gas fraction, metallicity) can in principle provide us with insights into any similarities and differences of star formation over different environments. A key goal of the JCMT GBS was to address this latter point, by acquiring extensive and highly sensitive submillimetre continuum maps of nearby star-forming clouds to identify their core populations.

Many previous investigations of molecular cloud core populations have focused on the number distributions of core masses, i.e., their Core Mass Functions (CMFs). The earliest studies of core populations in nearby clouds from their millimetre or submillimetre emission (Motte et al. 1998; Testi & Sargent 1998; Johnstone et al. 2000, 2001; Stanke et al. 2006) found remarkable similarities between the shape of the CMFs and that of the Initial Mass Function (IMF; Salpeter 1955; Kroupa 2001; Chabrier 2003), with power-law slopes at the high-mass ends of the CMFs being statistically similar to that of the IMF, i.e., -1.35 in log-log space (Salpeter 1955). Attention was given to the higher-mass ends of the CMFs due to the relatively limited sensitivities of the instruments involved, and little distinction was made between starless and protostellar cores in these studies. However, an early multi-cloud comparison of the CMFs of five nearby clouds by Sadavoy et al. (2010) drew on archival SCUBA data and distinguished between their starless and protostellar cores, finding consistency within errors between slopes of the starless CMFs of the five clouds and the Salpeter IMF slope, although accurately distinguishing between starless and protostellar cores remains difficult.

More recently, more sensitive instruments such as SCUBA-2 on the JCMT, SPIRE and PACS on the *Herschel* Space Observatory, and the Atacama Large Millimetre Array (ALMA) have enabled more thorough investigations of the CMF and its relationship to the IMF (e.g. Offner et al. 2014). These studies have allowed the high-mass end of the CMF to be well-constrained, and characterizations of them to go beyond the high-mass power-law slope to probe the lower-mass regime where the majority of cores must lie. Notably, *Herschel* data of the Aquila Rift showed that its prestellar CMF has a log-normal shape consistent with that of the Chabrier system IMF (Chabrier 2003), but one shifted to higher overall masses by a factor of 2–4 (André et al. 2010; Könyves et al. 2015). Similar CMF results were found with *Herschel* data of other clouds, e.g., Orion B (Könyves et al. 2020) and the Cepheus Flare clouds (Di Francesco et al. 2020). In contrast, ALMA studies of more distant Giant Molecular Clouds (GMCs) have suggested the presence of “top-heavy” CMFs, e.g., in W43-MM1 (Motte et al. 2018). A recent study by the ALMA-IMF Large Project (Motte et al. 2022; Ginsburg et al. 2022), which identified core populations in the protocluster regions of 15 GMCs at 2.0–5.5 kpc distance, has revealed other “top-heavy” CMFs, including all core types, but curiously the high-mass-end slopes of these are more Salpeter-like for arguably more-evolved protocluster regions (Pouteau et al. 2023). In addition, a recent ALMA-IMF study of the CMFs specifically of W43, i.e., its three subregions MM1, MM2 and MM3, shows that the slope of W43’s prestellar CMF is consistent with that of the high-mass end of the Salpeter IMF (Nony et al. 2023).

Recent investigations of the stellar IMF based on *Gaia* samples conclude that it varies little between nearby star-forming regions – the low-mass Taurus molecular cloud has the same IMF as the massive

Orion Nebula cluster (Luhman 2018). However, if a sub-sample is drawn from the IMF, then the maximum stellar mass increases with the size of the sample (Weidner & Kroupa 2006; Weidner et al. 2010; Elmegreen 2006). Only the largest clouds (with masses above around $10^4 M_\odot$) sample the full mass distribution and include the highest mass stars. In a hierarchical star-formation model, clusters build from star formation in smaller components, such as the clouds and filaments that are evident in the SCUBA-2 and *Herschel* data (Parker & Alves de Oliveira 2017). Each of these components contributes a fraction of the mass of the final cluster. These smaller samples of stars do not fully represent the IMF, and we might expect that smaller samples of cores might likewise under-represent the full mass distribution of the CMF. This possibility is something we can test with the GBS dataset, which covers a range of cloud masses from 200 to 20 000 M_\odot .

In this work, we describe the core populations of 12 nearby clouds drawn from the JCMT GBS SCUBA-2 data, in order to provide further insight into their nature and their CMFs. In Section 2, we summarize the observations and data reduction steps taken to produce the maps used in the subsequent analysis. In Section 3, we describe how the cores were extracted from the dataset, and how catalogue completeness was determined. In Section 4, we present the JCMT GBS core catalogue, describing its contents, core classification, and determination of individual core properties such as temperature, mass and density. In Section 5, we describe the overall characteristics of the core populations, including mass vs. size, relative numbers of starless and protostellar sources, and core stability. In Section 6 we construct CMFs for the clouds that we survey, and in Section 7 we discuss the implications of these CMFs. In Section 8, we summarize the conclusions of this paper.

2 OBSERVATIONS AND DATA REDUCTION

The JCMT Gould Belt Survey carried out SCUBA-2 observations of nearby molecular clouds between October 2011 and January 2015. The observing strategy is described in more detail by Kirk et al. (2018). In brief, each field was observed between four and six times depending on the weather conditions to obtain comparable sensitivities at 850 μm . Weather has a larger impact on the 450 μm data, and hence there is a larger variation in the sensitivities of those maps. Several observing modes were tested during the science verification phase, but the main survey used the PONG1800 (Kackley et al. 2010) mapping mode. We consider only the PONG1800 observations here. The PONG1800 mode produces a circular field of 0.5° diameter with near-uniform sensitivity (Holland et al. 2013). For large GBS fields, several PONG1800 maps were stitched together using the *ccd-pack makemos* tool in the *Starlink* software package. A summary of the regions mapped, their central coordinates, coverage area, and associated publications are given in Table 1. The data used in this paper were taken under project codes MJLSG31 (Orion A), MJLSG32 (Ophiuchus), MJLSG33 (Aquila and Serpens), MJLSG34 (Lupus), MJLSG35 (Corona Australis), MJLSG36 (IC 5146), MJLSG37 (Auriga and Taurus), MJLSG38 (Perseus), MJLSG39 (Pipe Nebula), MJLSG40 (Cepheus) and MJLSG41 (Orion B).

All ground-based submillimetre telescopes are unable to map large-scale emission structures, due to the bright and varying emission from the Earth’s atmosphere. Newer instrumentation and observing techniques have resulted in better recovery of such larger structures than was previously possible, and the JCMT GBS team spent significant effort testing different data reduction schemes to maximize the recovery of large-scale emission, as summarized by

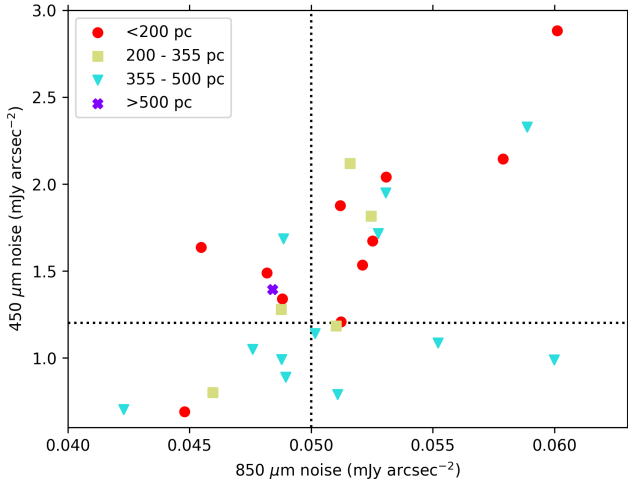


Figure 2. Representative rms values per mosaic at 850 μm and 450 μm . The dashed lines show the median rms per observing field (see text for more details). The points are colour-coded to the approximate distance to each cloud, as used in later analysis.

Kirk et al. (2018). Since these reduction techniques were developed alongside the science analysis of the survey data, some published papers from the survey listed in Table 1 used earlier reduction methods. Maps of all regions using the best reduction method are available for public download through Kirk et al. (2018), or directly at the DOI¹. In this work, we extract sources for the JCMT GBS core catalogue from this specific set of maps.

Figure 2 shows representative $1\text{-}\sigma$ rms values for each mosaic at 850 μm and 450 μm . We calculated these values by taking the median of the rms values per observing area (PONG1800 area) included in each mosaic. The dashed lines show the median rms of 0.050 mJy arcsec⁻² and 1.2 mJy arcsec⁻² at 850 μm and 450 μm respectively as measured from all individual PONG1800 observing areas. Note that the larger mosaics, such as in Orion and Perseus, had more high-priority fields observed in better weather conditions with fewer integrations needed to reach the same 850 μm noise level. With their greater sensitivity to the sky conditions, the 450 μm observations tend therefore to have lower noise levels in the larger mosaics. Since Figure 2 plots the noise over a per-mosaic area rather than per-PONG area, and there are a greater number of small-area mosaics compared to the large-area mosaics, the median of all 450 μm noise levels is at a noticeably lower value than the median of the per-region values shown in the figure.

2.1 Mapping Completeness

One important aspect that all surveys need to consider is how complete or how representative their mapped areas are. For the JCMT GBS, our goal was to map as much as possible of the highest column density material in the Gould Belt (nearby) molecular clouds visible from the JCMT. At the time, evidence suggested that most dense cores were found in clouds with $A_V \gtrsim 5 - 7$ mag (e.g., Johnstone et al. 2004; Hatchell et al. 2005; Kirk et al. 2006; Enoch et al. 2006; Froebrich & Rowles 2010; Belloche et al. 2011), so the GBS team targeted these areas, as were best known at the time. Here,

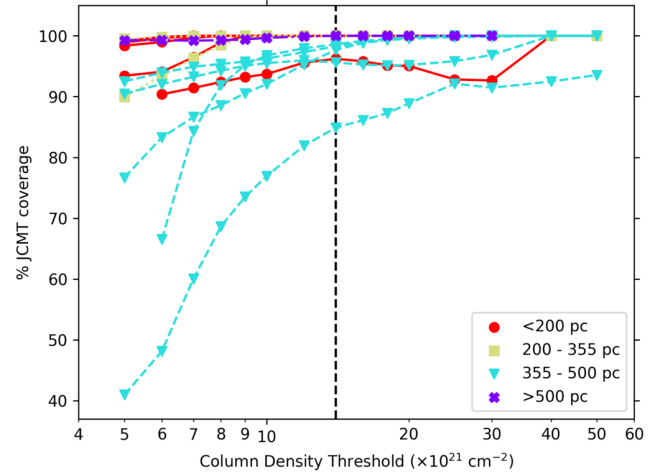


Figure 3. The fraction of material at a given *Herschel* Gould Belt Survey column density or higher mapped by the JCMT GBS. The vertical dashed line shows a column density of $N(\text{H}_2) = 1.4 \times 10^{22} \text{ cm}^{-2}$, which corresponds approximately to the JCMT GBS mapping goal of $A_V \gtrsim 7$ mag. Each line represents a different cloud complex that we consider.

we examine how complete our final mapped areas are, in the context of column densities of the Gould Belt clouds as derived by the *Herschel* Gould Belt Survey (André et al. 2010; Palmeirim et al. 2013; Schneider et al. 2013; Polychroni et al. 2013; Rygl et al. 2013; Könyves et al. 2015; Bresnahan et al. 2018; Arzoumanian et al. 2019; Di Francesco et al. 2020; Ladjelate et al. 2020; Pezzuto et al. 2021; Fiorellino et al. 2021), which generally mapped all of the clouds in the JCMT GBS over a larger area. For further details see the notes in Table A1. In general, the JCMT GBS maps cover all or nearly all of the higher column density material seen in the corresponding *Herschel* field: many of the JCMT maps lie near the 100% line running across the top of Figure 3, and are difficult to distinguish. To convert between column density and A_V , the *Herschel* GBS assumes that $N(\text{H}_2) (\text{cm}^{-2}) = 0.94 \times 10^{21} A_V (\text{mag})$ (Bohlin et al. 1978). This produces good agreement with 2MASS-based extinction maps in some regions (e.g. Könyves et al. 2015), but elsewhere can produce discrepancies of up to a factor ~ 2 (e.g. Könyves et al. 2020; Di Francesco et al. 2020; Pezzuto et al. 2021). Figure 3 therefore shows a line at $N(\text{H}_2) = 1.4 \times 10^{22} \text{ cm}^{-2}$, or a *Herschel* GBS A_V of 14 mag, broadly corresponding to a 2MASS-derived A_V of about 7 mag. As can be seen in Figure 3, our mapping completeness above this level is $> 90\%$ everywhere other than in the extremely dispersed Auriga molecular cloud (see Figure A2 in Appendix A), where it is $> 80\%$, indicating that the JCMT GBS met its mapping completeness goals. Table A1 in Appendix A provides the full set of mapping completeness values shown in Figure 3.

3 SOURCE EXTRACTION

3.1 getsources

We identified sources in the final JCMT GBS data release data products at 450 μm and 850 μm from Kirk et al. (2018) using *getsources* (Men'shchikov et al. 2012), an algorithm developed to identify and characterise sources in multi-wavelength submillimetre data sets. We use version 1.140127 of *getsources*, the same version used by the *Herschel* Gould Belt Survey for their source extractions, for consistency

¹ <https://doi.org/10.11570/18.0005>

Table 1. Regions observed by the Gould Belt Survey.

Region	R.A. (J2000)	Dec.	Coverage (deg ²)	JCMT GBS Publication	Distance (pc)	Dist. Ref.
Auriga-California	04 ^h 20 ^m 40 ^s 29	+37°44′53″7	1.68	Broekhoven-Fiene et al. (2018)	470	Zucker et al. (2019)
Cepheus L1228	20 ^h 57 ^m 51 ^s 78	+77°38′18″4	3.34	Pattle et al. (2017)	352	Zucker et al. (2019)
Cepheus L1251	22 ^h 33 ^m 43 ^s 74	+75°14′52″0	0.56	Pattle et al. (2017)	352	Zucker et al. (2019)
Cepheus South	20 ^h 50 ^m 03 ^s 94	+67°57′44″1	2.01	Pattle et al. (2017)	341	Zucker et al. (2020)
Corona Australis	19 ^h 05 ^m 57 ^s 95	−37°04′34″0	1.51	Pattle et al. (2025)	151	Zucker et al. (2019)
IC 5146	21 ^h 49 ^m 41 ^s 31	+47°26′24″9	1.56	Johnstone et al. (2017)	741	Zucker et al. (2020)
Lupus	15 ^h 42 ^m 27 ^s 00	−34°22′55″7	1.59	Mowat et al. (2017)	151	Zucker et al. (2019)
Ophiuchus L1688	16 ^h 32 ^m 05 ^s 01	−24°27′14″8	3.95	Pattle et al. (2015)	139	Zucker et al. (2019)
Ophiuchus L1689					147	Ortiz-León et al. (2017b)
Oph/Sco N2	16 ^h 47 ^m 38 ^s 77	−12°02′58″5	0.58	—	134	Zucker et al. (2020)
Oph/Sco N3	16 ^h 50 ^m 51 ^s 73	−15°21′40″0	0.57	—	151	Zucker et al. (2020)
Oph/Sco N6	16 ^h 21 ^m 13 ^s 76	−20°08′20″9	0.57	—	—	—
Orion A	05 ^h 37 ^m 58 ^s 03	−06°55′21″4	6.18	Salji et al. (2015a) Salji et al. (2015b) Coudé et al. (2016) Mairs et al. (2016) Lane et al. (2016)	432	Zucker et al. (2020) Kounkel et al. (2017)
Orion B L1622	05 ^h 54 ^m 32 ^s 80	+01°49′31″7	0.57	Kirk et al. (2016a) Kirk et al. (2016b)	423	Zucker et al. (2019)
Orion B N2023	05 ^h 42 ^m 05 ^s 02	−01°44′04″8	2.10	Kirk et al. (2016a)	423	Zucker et al. (2019) Kounkel et al. (2017)
Orion B N2068	05 ^h 46 ^m 51 ^s 30	+00°19′16″5	1.71	Kirk et al. (2016b) Kirk et al. (2016a) Kirk et al. (2016b)	423	Zucker et al. (2019)
Perseus IC348	03 ^h 43 ^m 42 ^s 75	+32°22′04″2	1.99	Chen et al. (2016)	321	Ortiz-León et al. (2018) Zucker et al. (2020)
Perseus West	03 ^h 30 ^m 53 ^s 54	+30°45′55″6	3.98	Hatchell et al. (2013) (NGC1333) Sadavoy et al. (2013) (B1) Dodds et al. (2015) (NGC1333) Chen et al. (2016)	294	Zucker et al. (2019)
Pipe B59	17 ^h 11 ^m 31 ^s 94	−27°26′27″7	0.57	—	180	Zucker et al. (2020)
Pipe E1	17 ^h 34 ^m 05 ^s 46	−25°39′19″9	0.56	—	180	Zucker et al. (2020)
Serpens Aquila	18 ^h 30 ^m 52 ^s 27	−02°05′50″3	1.68	Rumble et al. (2016) (W40)	484	Zucker et al. (2019)
Serpens East	18 ^h 37 ^m 29 ^s 09	−01°27′05″4	1.32	—	484	Zucker et al. (2019)
Serpens Main	18 ^h 29 ^m 36 ^s 20	+00°52′05″4	1.12	—	436	Ortiz-León et al. (2017a)
Serpens MWC297	18 ^h 28 ^m 13 ^s 80	−03°43′55″3	0.59	Rumble et al. (2015)	383	Herczeg et al. (2019)
Serpens North	18 ^h 39 ^m 05 ^s 20	+00°27′56″6	0.57	—	484	Zucker et al. (2019)
Taurus South	04 ^h 17 ^m 30 ^s 23	+27°50′08″0	2.86	—	141	Zucker et al. (2019)
Taurus L1495	04 ^h 29 ^m 20 ^s 91	+24°35′42″8	2.72	Buckle et al. (2015) Ward-Thompson et al. (2016)	141	Zucker et al. (2019)
Taurus TMC1	04 ^h 40 ^m 01 ^s 45	+26°00′42″2	1.67	—	141	Zucker et al. (2019)

with and to aid with future comparisons with their catalogues (e.g., Könyves et al. 2015, 2020; Di Francesco et al. 2020). We included SCUBA-2 maps at both 850 μ m and 450 μ m from the final JCMT GBS data release (Kirk et al. 2018) as input to *getsources*.

The *getsources* algorithm consists of two distinct stages. In the first “detection” stage, *getsources* smooths the input maps to successively lower resolution, subtracts maps at adjacent resolutions, and identifies positions of significant residual emission in the dif-

ference maps. These latter maps allow sources to be assembled and evaluated over ranges of scale and at each wavelength. At the end of the monochromatic evaluation, *getsources* combines the output from each wavelength to build an initial catalogue. In the second “measurement” stage, *getsources* determines the fluxes and sizes of detected sources using the original input images at each wavelength at their native resolutions. It further uses information from data at higher resolution to assist in deblending sources that overlap at lower

resolution. Background levels determined via linear interpolation under source footprints are subtracted to determine the measured fluxes at each wavelength. Unlike for the Herschel Gould Belt Survey catalogues, aperture corrections were not applied to the measured fluxes, because SCUBA-2 aperture corrections were not available in *getsources*. Possible effects of this are discussed in Section 3.4.3, below.

3.2 Source selection criteria

The *getsources* algorithm initially identified 4546 sources across the GBS regions. Applying the source selection criteria described below, determined through extensive visual inspection of the initial *getsources* output, resulted in a final core catalogue of 2257 sources considered reliable.

getsources determines the significance of a detection at a given wavelength using a metric known as “monochromatic significance”, an analogue to peak signal-to-noise ratio (SNR) determined by measuring SNRs over the multiple size scales on which *getsources* makes measurements (Men’shchikov et al. 2012). Similarly, the overall significance of a detection is quantified by its “global significance”, which is the quadrature sum of the monochromatic significances. *Getsources* also provides a “global goodness parameter” combining the global significance and global SNR parameters. We removed sources for which any of the following criteria were met:

- (i) Global goodness < 1
- (ii) $850\ \mu\text{m}$ monochromatic significance ≤ 7
- (iii) Global significance ≤ 10

These criteria were chosen as *getsources* documentation advises that only sources with a global goodness > 1 and monochromatic significances > 7 be retained. The global significance criterion results from the quadrature sum of the $850\ \mu\text{m}$ and $450\ \mu\text{m}$ monochromatic significances; a global significance of 10 approximately equates to monochromatic significances of 7 in both wavelengths. For blended sources, the *getsources* monochromatic significance should be a better measure of source reliability than a conventional SNR determined from the final *getsources* catalogue values (Men’shchikov et al. 2012). As a backstop for the more stringent criteria (i)–(iii), we also excluded sources where:

- (iv) $850\ \mu\text{m}$ peak flux density SNR ≤ 2
- (v) $850\ \mu\text{m}$ total (integrated) flux density SNR ≤ 1

We further excluded sources where *getsources* had judged either the peak or total flux density (or the uncertainties on either of these parameters) to be too small to measure at $850\ \mu\text{m}$:

- (vi) $850\ \mu\text{m}$ peak flux density OR $850\ \mu\text{m}$ peak flux density uncertainty OR $850\ \mu\text{m}$ total flux density OR $850\ \mu\text{m}$ total flux density uncertainty = 9.999E-31

The output from *getsources* includes a “monochromatic flag” (FM) parameter, which provides information on the reliability of a source based on its size, SNR, sub-structure, significance, etc., at a given wavelength. We excluded sources where

- (vii) $850\ \mu\text{m}$ FM = 1 AND ($450\ \mu\text{m}$ FM = 31 OR $450\ \mu\text{m}$ FM > 200)

FM = 1 indicates that a source is larger than the characteristic size scale, while FM = 31 indicates both FM = 1 holds for a source and that its total flux and peak flux density both have SNR < 1 (FM = 30). FM > 200 indicates a monochromatic significance < 3.5 . This

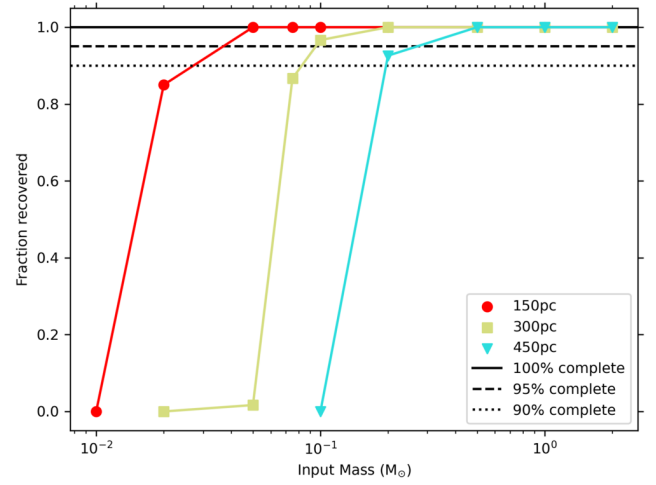


Figure 4. Fraction of input BEC spheres returned by *getsources* as a function of input source mass, for sources at distances of 150 pc (red circles), 300 pc (green squares) and 450 pc (blue triangles). Solid black line marks 100% completeness; dashed line marks 95% completeness; dotted line marks 90% completeness.

final criterion thus excludes large diffuse $850\ \mu\text{m}$ sources if there is no hint of a detection at $450\ \mu\text{m}$.

3.3 Known CO artefacts

As the SCUBA-2 $850\ \mu\text{m}$ band includes the rest frequency of the CO $J = 3 - 2$ line, observed $850\ \mu\text{m}$ fluxes may be artificially increased at locations of bright CO line emission (Drabek et al. 2012; Sadavoy et al. 2013). Maps of CO $J = 3 - 2$ emission obtained with the JCMT HARP instrument by the JCMT GBS can be used to remove CO emission in some locations – see Kirk et al. (2018) for more information. However, the JCMT GBS HARP coverage was not as extensive as the SCUBA-2 coverage. We thus do not use CO-subtracted $850\ \mu\text{m}$ maps in this work, both so that all of the regions that we consider are treated consistently, and in order to avoid edge effects at the interfaces between regions with CO data and without. We expect the contribution of CO emission to the $850\ \mu\text{m}$ fluxes in our catalogue to be generally $< 20\%$ (e.g., Pattle et al. 2015). However, CO contamination is most significant toward bright outflows (Johnstone et al. 2003; Coudé et al. 2016), and a small number of knots of bright compact CO emission have been identified by *getsources* in our maps. Knowing these locations from experience (near the bright protostellar sources L1147-mm and IRAS 16293-2422; Pattle et al. 2015, 2017), five associated sources were flagged and removed from the final catalogue by hand.

3.4 Catalogue completeness

In order to interpret the distribution of core properties which we measure, it is vital to understand the mass completeness of our catalogue: both the fraction of sources that are recovered as a function of core mass (the source recovery fraction), and the fraction of true source mass that is recovered in our catalogue (the mass recovery fraction).

We expect mass completeness to be a strong function of distance. For example, lower-mass sources should be fainter and smaller, and (for a given core temperature) will therefore be significantly easier

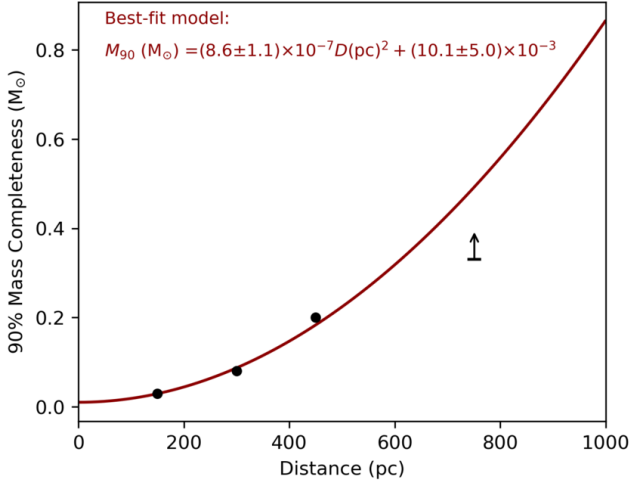


Figure 5. Our estimated 90% mass completenesses as a function of distance. A quadratic fit to the data is shown. The lowest-mass source detected in IC 5146 is shown as a lower limit for mass completeness at this distance.

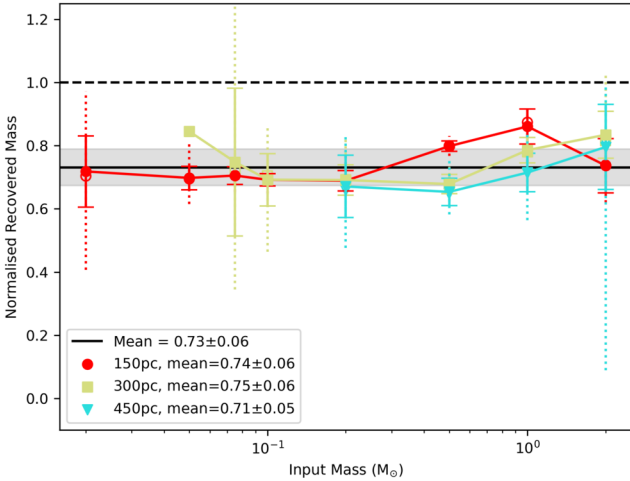


Figure 6. Fraction of input source mass recovered by *getsources*, as a function of input source mass. Colour and shape of data points are as in Figure 4. Symbols mark mean recovered mass fraction; solid error bars mark $1-\sigma$ variation around the mean, while dotted error bars mark the full range of values. The solid black line marks the ‘mean of means’: the average mass recovery fraction; grey shading marks the $1-\sigma$ variation on this value. Dashed line marks a recovered mass fraction of 1.0.

to detect in nearer clouds. Throughout this work, we thus divide the sample clouds into four distance ranges:

- (i) **Near (<200 pc), representative distance 150 pc:** Corona Australis, Lupus, Ophiuchus, Oph/Sco North, Pipe and Taurus.
- (ii) **Mid-distance clouds (200–355 pc), representative distance 300 pc:** Cepheus and Perseus.
- (iii) **Far clouds (355–500 pc), representative distance 450 pc:** Auriga-California, Orion A and B, and Serpens.
- (iv) **Very far clouds (>500 pc):** IC 5146.

IC 5146 the only cloud at a distance > 500 pc, placed at 751 pc by Zucker et al. (2020) using *Gaia* measurements. The distance to

this cloud has been revised upward significantly since the GBS was designed, from a previous value of 460 pc (Lada et al. 1999), and the cloud is typically no longer considered to be a member of the Gould Belt (e.g. Dzib et al. 2018). Given the lack of clouds at comparable distance for comparison, and the relatively small number of sources (71) detected in the region, we include this cloud and its cores in our catalogue, but largely exclude it from our discussion of typical core properties.

3.4.1 Method for determining mass completeness

We determined the completeness of our core catalogue by running a series of tests in which we inserted artificial critically-stable Bonnor–Ebert (BEC) spheres (Ebert 1955; Bonnor 1956) into the Oph/Sco N6 field. This field contains no detectable sources, and has previously been used for GBS completeness testing (Kirk et al. 2018). We tested masses in the range $0.01\text{--}2\text{ }M_{\odot}$, placing our input BEC spheres at the representative distances for the near-, mid- and far-distance clouds: 150 pc, 300 pc, and 450 pc. We converted the mass distributions of our BEC spheres into flux densities using the Hildebrand (1983) relationship, taking dust opacity index $\beta = 1.8$, consistent with Planck observations (Juvela et al. 2015) and joint *Herschel*/SCUBA-2 fits to GBS data (Chen et al. 2016; Sadavoy et al. 2013). The process for creating these BEC sphere models is described in detail in Appendix B, and the python code used to do so is publicly available².

We repeated the data reduction process for Oph/Sco N6, using the *fakemap* parameter³ in *makemap* (Chapin et al. 2013) to insert each of our fields of model BEC spheres. We then used the *getsources* algorithm, with the same parameters as described in Section 3.1 above, to search for the cores which we had inserted. We then applied the same selection criteria to the *getsources* catalogues as described in Section 3.2, above. Our completeness testing procedure is described in detail in Appendix B. Here, we highlight the key results.

3.4.2 Source recovery completeness fraction

Figure 4 shows the fraction of input sources that are recovered as a function of input mass, for each of our three representative distances. As expected, more massive sources are more easily recovered, and mass completeness is better at nearer distances. We find > 90% completeness limits for the three distance ranges of $0.03\text{ }M_{\odot}$, $0.075\text{ }M_{\odot}$ and $0.2\text{ }M_{\odot}$ for 150 pc, 300 pc and 450 pc, respectively. These limits are shown as a function of distance in Figure 5, and are quite well-fitted by a quadratic function, $M_{90}\text{ (}M_{\odot}\text{)} \approx (8.6 \pm 1.1) \times 10^{-7} D(\text{pc})^2$. We choose to fit a quadratic function as the flux density of a source of given mass and temperature scales as D^{-2} (Hildebrand 1983), where D is the distance of the source.

The mass completeness limit in IC 5146 is $\geq 0.33\text{ }M_{\odot}$, as this is the lowest-mass source that we detect (see Section 4.2.2, below). Extrapolation of our best-fit quadratic model suggests a > 90% mass completeness limit in IC 5146 of $\approx 0.5\text{ }M_{\odot}$, consistent with our observations.

There are a number of reasons to expect that these completeness limits are somewhat conservative. In our completeness testing, we

² BEC code is available at: <https://github.com/KatePattle/bonnor-ebert-sphere>

³ The *fakemap* parameter allows the user to provide an image of the sky that will produce corresponding additional astronomical signal in the SCUBA-2 bolometer time series; see <http://starlink.eao.hawaii.edu/docs/sun258.pdf>

place our model sources directly onto the noisy background of the Oph/Sco N6 field. In reality, many sources are embedded within filaments or other structures, as can be seen in Figure 1, and so may be sufficiently boosted above the background to be detected. We further note that we have performed our completeness testing for critically-stable Bonnor–Ebert spheres, whereas gravitationally bound and collapsing cores should be more centrally condensed, and so more easily detectable. Moreover, the Oph/Sco N6 field was observed in Band 2 weather; regions observed in Band 1 weather will have somewhat better SNR, particularly at 450 μm , and so fainter sources will be more easily detected in these regions. Particularly in the far-distance fields, a non-negligible number of sources are detected below the nominal completeness limit (cf. Section 6, below).

3.4.3 Mass recovery fraction

We calculated the recovered mass of each of our recovered sources from the 850 μm flux densities returned by *getsources* and the assumed temperature and dust properties described above (cf. eqs. 1 and 2, below). Figure 6 shows the fraction of input mass recovered for a given source as a function of the true input mass, for each of our three representative distances.

Our global mass recovery fraction – the typical fraction of input mass recovered above the 90% source recovery completeness limit – is 0.73 ± 0.06 . The mean recovered mass fractions for each input mass and distance are shown in Figure 6. We took the mean of these mean values, for input masses above the 90% completeness level in each field, in order to calculate our global mass recovery fraction. We therefore excluded the single $0.05 M_{\odot}$ source recovered at 300 pc as the 90% completeness limit at 300 pc is $0.075 M_{\odot}$.

There are several effects that are likely to be resulting in loss of input flux, and so the decrease in recovered mass. (1) A BEC sphere is characterised by a relatively flat central plateau at small radii, with a power-law drop-off in density beyond a critical radius (Ebert 1955; Bonnor 1956). We further convolve the BEC sphere surface brightness profiles which we generate with the JCMT beam (Dempsey et al. 2013). At low masses, we simply expect the fainter material associated with the source to be undetectable above the noise in the field. (2) In more extended higher-mass sources, we expect that some fraction of the flux loss is likely due to the effects of performing submillimetre continuum measurements below the atmosphere. The SCUBA-2 iterative map-making process *makemap* (Chapin et al. 2013) is unable to distinguish between atmospheric and astrophysical signal on sizes comparable to the SCUBA-2 array ($\sim 600''$; Holland et al. 2013), and we expect this behaviour to result in loss of extended structure in both our real and our synthetic observations. This effect has been discussed extensively in previous SCUBA-2 papers (Sadavoy et al. 2013; Pattle et al. 2015; Mairs et al. 2015; Kirk et al. 2018). We further note that as we have chosen to model BEC spheres, as we go to higher masses, the sources both get larger and have lower peak brightnesses: these effects may conspire to make the sources harder to recover. A direct comparison with the Gaussian mass (total flux) recovery results from Kirk et al. (2018) suggests that for all but the few highest mass BEC models, filtering has a $< 10\%$ effect when the core’s peak flux is at or above 5 times the local noise. (3) The lack of appropriate SCUBA-2 aperture corrections available in *getsources* may result in some loss of extended emission.

Figure 6 shows a peak in mass recovery fraction at $1 M_{\odot}$ at 150 pc, followed by a slight drop-off for $2 M_{\odot}$, likely due to a combination of these effects. The 300 pc and 450 pc sources appear to show a similar trend, displaced to higher masses; both have their highest mass recovery fraction at the highest mass tested, $2 M_{\odot}$, with the

$2 M_{\odot}$ mass recovery fraction being slightly higher at 300 pc than at 450 pc, although the two agree within their respective error bars. However, despite this variation, the fraction of mass recovered is quite constant across the range of masses which we consider. Thus, we adopt our mean mass recovery fraction, 0.73 ± 0.06 , wherever a correction is required in the following analysis. Masses are presented as measured by *getsources* (without any correction for flux loss) unless otherwise stated.

3.4.4 Comparison to Herschel Gould Belt Survey completeness

The dense core catalogues produced by the *Herschel* GBS (André et al. 2010) provide a natural point of comparison to our JCMT GBS catalogue. However, direct comparison between individual sources in the JCMT and *Herschel* catalogues is non-trivial, due to the many differences between observations made by the two instruments, particularly the differing instrumental responses to large-scale structure between the *Herschel* photometers and SCUBA-2 (Sadavoy et al. 2013; Ward-Thompson et al. 2016), and the differences in wavelength between the two instruments (note that the emission peak within a single source may vary with wavelength; e.g., Encalada et al. 2024). Nonetheless, we find that the mass completeness limits of our catalogue and the *Herschel* GBS catalogues are comparable.

Herschel Gould Belt Survey observations are cirrus confusion limited (André et al. 2010), meaning that their source completeness is dependent on environment (Könyves et al. 2015). Most *Herschel* GBS papers model their completeness for prestellar cores on a high-column-density background, with cores modelled as having critically-stable Bonnor–Ebert-like density profiles, with a significant drop in temperature towards the centre (Könyves et al. 2015).

The masses at which the *Herschel* GBS achieves 80–90% completeness for recovery of prestellar cores in dense environments are comparable to but somewhat higher than our own values at comparable distances due to their need to disentangle dense cores from the extended structure to which SCUBA-2 is not sensitive. The 80–90% mass completeness limit for prestellar cores is consistently found to occur at $0.1 M_{\odot}$ in nearby (130–200 pc) clouds (Marsh et al. 2016; Benedettini et al. 2018; Bresnahan et al. 2018; Ladjelate et al. 2020; Kirk et al. 2024), 0.3 – 0.4 at 300–400 pc (Di Francesco et al. 2020; Könyves et al. 2020; Pezzuto et al. 2021), and $0.8 M_{\odot}$ at the maximum distance the HGBS considers, 484 pc (Fiorellino et al. 2021). We note that these mass completeness limits are typically corrected for the estimated 20–30% underestimation of source mass that arises from fitting a single-temperature modified blackbody model to the spectral energy distribution of a non-isothermal core (Könyves et al. 2015).

The *Herschel* GBS typically recovers significantly larger numbers of low-mass cores in low-column-density regions than are detectable in SCUBA-2 observations (Ward-Thompson et al. 2016; Könyves et al. 2020), due to SCUBA-2’s lack of sensitivity to extended emission. Marsh et al. (2016) found a mass completeness limit in Taurus of $> 85\%$ at $0.015 M_{\odot}$ for unbound starless cores on a low-column-density background at a distance of 140 pc, two orders of magnitude better than their completeness for deeply embedded prestellar cores at the same distance, and comparable to but notably better than our 90% mass completeness at 150 pc of $0.03 M_{\odot}$.

The complexity of interpreting the differences in source identification and completeness means that a detailed core-by-core comparison of the JCMT and *Herschel* GBS catalogues is beyond the scope of this work. However, we have chosen to use the same source extraction algorithm as the *Herschel* GBS in order to perform this work in the

future; we note that the similar completeness levels between the two surveys suggests that such a comparison would be meaningful.

4 THE JCMT GBS CATALOGUE

The JCMT Gould Belt Survey core catalogue contains 2257 sources. A sample of the measured source properties is given in Table 2. The key derived source properties for the same source sample is given in Table 3. The data available in the catalogue is summarized in Table 4. The full catalogue is available online, along with the output of the *getsources* algorithm without our selection criteria applied.

4.1 Source categorization

We categorize our sources as starless cores ('C'); protostellar ('P'), i.e. those sources cross-matched with a known YSO or YSO candidate; heated ('H'), i.e. those sources cross-matched with a *Spitzer* 24 μm detection and so potentially protostellar; or as a potential contaminant extragalactic source ('G'). A source is categorized as a starless core by elimination, i.e. if it is not categorized as protostellar, heated or potentially extragalactic.

4.1.1 Potential extragalactic contaminants

To identify any potential extragalactic contaminants in our catalogue, we queried the NED database⁴ within a circular area around each peak source position of radius equal to the geometric mean of the major and minor FWHM axes of the source. If the query returned any objects classified as galaxies, galaxy groups or galaxy clusters (i.e., having a 'G', 'GClstr', 'GGroup', 'GPair', 'GTrpl' or 'G_Lens' designation in NED), we initially categorized the source as a potential extragalactic contaminant.

Of the 2257 sources in our catalogue, 65 had NED matches. We note that all of these sources are associated with nearby molecular clouds, and so their true status as extragalactic sources is doubtful. When comparing against protostellar catalogues (as described in Section 4.1.2, below), 45 of the sources with NED matches were also identified with a protostellar source. We classified these 45 sources as protostellar, as the more probable identification. We investigated the remaining 20 NED matches individually, comparing the name given in the NED database with their equivalent entries (if any) in the SIMBAD⁵ database (Wenger et al. 2000). One source, JCMTLSG183004.0-020306, is known to be a small protostellar cluster (Kern et al. 2016), and was clearly misidentified in NED. This source was also associated with 24 μm emission (cf. Section 4.1.3). We thus classified this source as protostellar. Of the remaining 19 sources, two were identified in SIMBAD as radio sources, two as low-mass stars, and one as a Herbig–Haro object. The remainder had no match in SIMBAD, and appear to have been classified as galaxies in the 2MASS eXtended (Skrutskie et al. 2006) or allWISE (Cutri et al. 2021) catalogues. We excluded all 19 of these sources from further consideration in the interest of ensuring an uncontaminated catalogue of dense cores. However, all sources appear in the final catalogue, with their NED and, where relevant, SIMBAD identifiers noted.

⁴ <https://ned.ipac.caltech.edu/>

⁵ <http://simbad.u-strasbg.fr/simbad/>

4.1.2 Protostellar sources

A source is categorized as protostellar if it contains at least one protostar or YSO within its area. We searched the *Spitzer* and WISE protostellar catalogues for matches within a circular area around each peak source position with a radius equal to the geometric mean of the major and minor FWHM axes of the source.

The revised *Spitzer* c2d catalogue (Dunham et al. 2015) lists protostars and YSOs detected by *Spitzer* in Lupus, Ophiuchus, Perseus, Serpens (except Serpens East), and Chamaeleon (not covered by our observations). Protostars in Orion A and B were surveyed by Megeath et al. (2012), and in Taurus by (Rebull et al. 2010). The *Spitzer* Gould Belt Survey lists protostars in Auriga-California (Broekhoven-Fiene et al. 2014), Cepheus (Kirk et al. 2009), Corona Australis (Peterson et al. 2011), IC 5146 (Harvey et al. 2008), and Ophiuchus North (Hatchell et al. 2012). The only region observed by the GBS not covered by a *Spitzer* protostellar catalogue is Serpens East.

We further performed cross-matching with the Wide-Field Infrared Survey Explorer (WISE) All-Sky Survey YSO catalogue (Marton et al. 2016). We cross-matched our sources with their list of Class I and II sources only. We did not consider their Class III sources, as these will no longer be embedded.

We did not cross-match with *Herschel* protostellar catalogues (e.g. Könyves et al. 2015; Bresnahan et al. 2018; Könyves et al. 2020) because these catalogues are not available for all of the regions that we consider, and so we could not do so self-consistently.

4.1.3 Cross-matching with *Spitzer* 24 μm detections

Cores containing low-luminosity embedded protostars sometimes escape classification as YSOs but can still be identified by their *Spitzer* 24 μm emission, as can bright galaxies and AGB stars. To remove these potential contaminants from the starless core catalogue, the *Spitzer* Cores to Disks and *Spitzer* Gould Belt full high reliability catalogues were searched for 24 μm matches with offsets from the SCUBA-2 peak within the core deconvolved radius or half the JCMT 850 μm beam FWHM, whichever was the greater. To be considered as a match, the 24 μm source had to have an SNR of at least 3 (quality flag MP1_Q_det_c = 'A' or 'B'; Evans et al. 2007).

The separation distributions of 24 μm matches for protostellar cores and for starless cores both peak at small separations of ~ 0.01 pc as shown in Fig. 7 (top panel), but whereas for protostellar cores the peak is at small fractions (0.3–0.4) of the deconvolved radius, for starless cores the peak is further out (0.5–0.6) and rises again at separations close to the deconvolved radius (Fig. 7 bottom panel). This second peak suggests that some of the 24 μm matches are bright cloud rims or background sources. To reduce such false positives due to background confusion, we calculated the 95% percentile of the separation distribution for 24 μm matches with protostellar cores (bona fide 24 μm matches) and applied this as an additional separation cutoff to the starless core candidates. This criterion was applied to physical (projected) distance, rather than angular distance, so that the distribution reflects the real physical separations between dust peaks and 24 μm emission in protostars e.g. due to outflow cavities. As a result, we only consider separations below 0.0525 pc as genuine associations. Using this revised criterion reduced the number of reclassified cores by roughly a quarter. In total, 80 cores (just under 5%) were reclassified from starless to 'heated' (i.e. potentially protostellar) due to 24 μm associations, with a separation distribution shown in Fig. 7. 10 of these cores were later excluded by the selection criteria described in Section 3.2, leaving 70 heated cores in the final catalogue.

Table 2. Measured properties of the first ten JCMT GBS sources in our catalogue. The abbreviation “mJy/sqa” is used for the unit mJy arcsec⁻². The full catalogue is available in the online material associated with this paper.

Running No.	Region	Source ID (JCMTLSG...)	850μm				450μm			
		R.A., Dec. (J2000)	Peak F.D.	Total F.D.	FWHM	P.A.	Peak F.D.	Total F.D.	FWHM	P.A.
		HHMMSS.S+DDMMSS	(mJy/sqa)	(mJy)	(arcsec)	(deg)	(mJy/sqa)	(mJy)	(arcsec)	(deg)
1	Aquila	183004.0-020306	3.70 ± 0.08	5.8 ± 0.1	16.3 × 14.1	29	13.2 ± 0.3	61.1 ± 0.9	18.0 × 14.2	22
2	Aquila	183002.4-020249	1.44 ± 0.08	3.1 ± 0.1	23.2 × 14.1	164	5.8 ± 0.3	17.6 ± 0.6	16.0 × 9.7	178
3	Aquila	182937.6-015101	0.65 ± 0.05	0.79 ± 0.06	14.1 × 14.1	–	3.0 ± 0.1	4.6 ± 0.2	9.6 × 9.6	–
4	Aquila	182908.1-013049	0.82 ± 0.05	0.93 ± 0.05	14.1 × 14.1	–	4.5 ± 0.1	5.5 ± 0.2	9.6 × 9.6	–
5	Aquila	183109.5-020624	0.62 ± 0.04	0.76 ± 0.04	14.1 × 14.1	–	3.0 ± 0.2	5.6 ± 0.2	11.2 × 9.6	92
6	Aquila	183001.4-021027	0.69 ± 0.03	1.05 ± 0.03	15.5 × 14.1	167	3.0 ± 0.1	5.8 ± 0.2	11.4 × 9.6	171
7	Aquila	183121.3-020658	0.53 ± 0.08	0.62 ± 0.08	14.1 × 14.1	–	2.3 ± 0.3	4.0 ± 0.4	11.6 × 9.6	16
8	Aquila	183110.4-020350	0.51 ± 0.06	0.67 ± 0.06	20.3 × 14.1	3	2.3 ± 0.2	4.0 ± 0.2	15.3 × 9.6	2
9	Aquila	182903.6-013907	0.56 ± 0.03	0.60 ± 0.03	14.1 × 14.1	–	2.4 ± 0.1	2.5 ± 0.1	9.6 × 9.6	–
10	Aquila	183121.0-020623	0.76 ± 0.08	1.5 ± 0.1	20.7 × 14.1	12	3.0 ± 0.2	11.1 ± 0.3	18.5 × 11.8	15

Table 3. Derived properties of the first ten JCMT GBS sources in our catalogue. The full catalogue is available in the online material associated with this paper.

Running No.	Type	R_{deconv} (pc)	T (K)	M (M_{\odot})	$N(\text{H}_2)$ ($\times 10^{22} \text{ cm}^{-2}$)	$n(\text{H}_2)$ ($\times 10^4 \text{ cm}^{-3}$)	M_{BE} (M_{\odot})	α_{BE} (–)	$M_{\text{BE}}(10 \text{ K})$ (M_{\odot})	$\alpha_{\text{BE}}(10 \text{ K})$ (–)
1	P	0.013	17.5	10.7 \pm 0.2	87 \pm 1	1610 \pm 30	0.59 \pm 0.07	0.055 \pm 0.006	0.34 \pm 0.04	0.012 \pm 0.001
2	P	0.027	17.4	5.8 \pm 0.2	11.5 \pm 0.5	105 \pm 4	0.95 \pm 0.09	0.16 \pm 0.02	0.55 \pm 0.05	0.035 \pm 0.004
3	P	–	16.2	1.7 \pm 0.1	–	–	0.21 \pm 0.05	0.13 \pm 0.03	0.13 \pm 0.03	0.033 \pm 0.007
4	H	–	15.5	2.1 \pm 0.1	–	–	0.21 \pm 0.04	0.10 \pm 0.02	0.13 \pm 0.03	0.028 \pm 0.006
5	H	–	31.9	0.60 \pm 0.03	–	–	0.42 \pm 0.09	0.7 \pm 0.2	0.13 \pm 0.03	0.035 \pm 0.008
6	C	0.010	17.3	1.96 \pm 0.07	25.1 \pm 0.8	590 \pm 20	0.51 \pm 0.06	0.26 \pm 0.03	0.30 \pm 0.04	0.056 \pm 0.007
7	C	–	57.8	0.24 \pm 0.03	–	–	0.8 \pm 0.2	3.2 \pm 0.8	0.13 \pm 0.03	0.04 \pm 0.01
8	C	0.022	28.2	0.62 \pm 0.05	1.8 \pm 0.2	20 \pm 2	1.3 \pm 0.1	2.2 \pm 0.3	0.48 \pm 0.05	0.14 \pm 0.02
9	C	–	15.6	1.34 \pm 0.08	–	–	0.21 \pm 0.04	0.15 \pm 0.03	0.13 \pm 0.03	0.04 \pm 0.01
10	C	0.023	58.5	0.58 \pm 0.04	1.6 \pm 0.1	17 \pm 1	2.8 \pm 0.3	4.9 \pm 0.6	0.49 \pm 0.05	0.063 \pm 0.008

We note that the *Spitzer* MIPS 24 μ m channel is saturated in the brightest parts of the Orion Molecular Cloud. We manually flagged the Orion BN/KL region in Orion A (JCMTLSG 053514.3-052231) and the centre of Orion B NGC 2074 (JCMTLSG 054144.6-015540) as protostellar.

4.1.4 Final classification

Of our 2257 sources, 1321 are classed as starless (‘C’), 847 as containing an embedded protostar (‘P’), 70 as heated (24 μ m-bright; ‘H’), and 19 as potential extragalactic contaminants (‘G’). We consider anything with a P or H classification as potentially protostellar in nature. It is important to note that ‘protostellar’ thus effectively means that the source has an infrared association. Our aim is to create an uncontaminated catalogue of starless cores, and so some of the objects identified as protostellar may in fact be shocked knots, or other externally heated objects without embedded sources.

4.2 Derived properties

The derived properties of our sources are listed in Table 3, and in the full catalogue which is supplied as an online resource.

4.2.1 Source Temperature

To calculate core masses, a dust temperature estimate is required. Dust temperatures vary between cores and within them, depending on the strength and penetration of the interstellar radiation field in

the absence of internal heating (Evans et al. 2001). Isolated prestellar cores have been measured and modelled to have central dust temperatures as low as 7–9 K (e.g. Leung 1975; Evans et al. 2001; Nielbock et al. 2012). The *Herschel* surveys of Serpens and Aquila find core average temperatures of 10–11 K for robust prestellar cores and 15 K for unbound cores, from SED fitting with an opacity-modified black-body (Fiorellino et al. 2021; Könyves et al. 2015). From Bayesian modelling, core-containing filaments in Ophiuchus and Taurus have mass-weighted temperatures of 10–15 K in Taurus and 14–20 K in Ophiuchus (Howard et al. 2019, 2021). Higher temperatures are produced by an enhanced radiation field, for example due to proximity to OB stars. In particular, dust temperatures in Orion A reach more than 40 K due to heating by the Orion Nebula Cluster and multiple other OB stars in the region (Schuller et al. 2021).

The GBS has previously mapped dust colour temperature from the ratio of the SCUBA-2 450 μ m to 850 μ m intensities (Rumble et al. 2021), assuming a fixed dust opacity index of $\beta = 1.8$. These maps do not cover the whole area mapped by the JCMT GBS, as this method requires a high-SNR 450 μ m detection, achievable only in bright regions observed in good weather, and so are insufficient to extract temperatures for the individual cores considered here. However, where there is coverage, the average dust colour temperature of an unheated dust clump is 15 K, rising to 20 K or more in the vicinity of OB stars (within 1 pc for early B type, 2.4 pc of O-type). This effect can be modelled based on plane-of-the-sky proximity to the dominant OB star and its stellar spectral classification. Temperatures of 15 K are consistent with the *Herschel*-based estimates for unbound starless cores. The lower, 10–11 K, temperatures for bound prestel-

Table 4. A list of the quantities and information given in the JCMT Gould Belt Survey core catalogue, available as online material associated with this paper. See Section 4.2.5 for a detailed description of columns 31–39, and Section 4.1 for a detailed description of columns 40–44.

Column number	Units	Description
(1)	–	Running number
(2)	–	Region
(3)	–	Source ID ^a
(4, 5)	mJy arcsec ⁻²	Peak 850 μ m flux density and associated uncertainty
(6, 7)	mJy	Total 850 μ m flux density and associated uncertainty
(8, 9)	arcsec	850 μ m major and minor FWHMs
(10)	deg	850 μ m position angle ^b
(11, 12)	mJy arcsec ⁻²	Peak 450 μ m flux density and associated uncertainty
(13, 14)	mJy	Total 450 μ m flux density and associated uncertainty
(15, 16)	arcsec	450 μ m major and minor FWHMs
(17)	deg	450 μ m position angle ^b
(18)	–	Source classification ^c
(19)	–	Resolved/unresolved flag ^d
(20)	pc	Deconvolved radius
(21, 22)	K	Assumed temperature and associated uncertainty
(23, 24)	M _⊙	Derived mass and associated uncertainty
(25, 26)	cm ⁻²	Column density of H ₂ and associated uncertainty
(29, 30)	cm ⁻³	Volume density of H ₂ and associated uncertainty
(31, 32)	M _⊙	Critical Bonnor–Ebert (BEC) mass and associated uncertainty
(33, 34)	–	BEC stability ratio and associated uncertainty
(35, 36)	M _⊙	BEC mass at 10 K and associated uncertainty
(37, 38)	–	BEC stability ratio at 10 K and associated uncertainty
(39)	–	Boundedness flag ^e
(40)	–	Best match to source in <i>Spitzer</i> 24 μ m catalogue
(41)	–	Best match to source in <i>Spitzer</i> protostellar catalogues
(42)	–	Best match to source in WISE all-sky YSO catalogue (Marton et al. 2016)
(43)	–	Best match to source in NED database
(44)	–	For sources with a NED match, classification of source in SIMBAD database

^a Format “JCMTLSG HHMMSS.S+DDMMSS”; where the source name comprises the J2000 coordinates of the source.

^b Position angles are measured East of North.

^c See Section 4.1.

^d 1 = resolved at 850 μ m, and 0 = unresolved at 850 μ m.

^e –1 = not a starless core; 0 = unbound, 1 = candidate starless core, bound at 10 K, 2 = robust prestellar core, bound at ≥ 15 K.

lar cores are not seen because the clumps in Rumble et al. (2021) are typically larger (median flux-weighted clump size 0.08 pc) and estimates include the warmer dust in the surrounding filament.

For regions without OB stars, we assume $T = 15$ K for our cores, which is consistent with the mean temperature of unheated clumps in the GBS temperature maps and with the temperature of unbound cores in the *Herschel* studies of Serpens/Aquila (Fiorellino et al. 2021; Könyves et al. 2015).

For regions with OB stars, we estimate temperatures based on proximity to the irradiating source using the Rumble et al. (2021) formula, which assumes a base temperature of 15 K and temperature increases based on proximity to the main OB star in the neighbourhood.

Orion A is complicated by the presence of many OB stars, so we assume temperatures of 40 K in the vicinity of the Trapezium cluster, of 20 K at declinations $> -5.277^\circ$, and of 15 K at declinations $< -5.525^\circ$, following the NH₃ gas temperatures measured by Friesen et al. (2017) and the dust temperatures measured by Schuller et al. (2021).

4.2.2 Source Masses

We calculate source masses from their 850- μ m flux densities using the Hildebrand (1983) relationship,

$$M = \frac{F_\nu D^2}{\kappa_\nu B_\nu(T)}, \quad (1)$$

where F_ν is integrated flux density at 850 μ m, D is distance to the source, κ_ν is the dust opacity and $B_\nu(T)$ is the Planck function, where T is determined as discussed above. We determine dust opacity at 850 μ m using the Beckwith et al. (1990) relationship,

$$\kappa_\nu = 0.1 \left(\frac{\nu}{10^{12} \text{ Hz}} \right)^\beta \text{ cm}^2 \text{ g}^{-1}, \quad (2)$$

again taking $\beta = 1.8$ (cf. Sadavoy et al. 2013; Juvela et al. 2015; Chen et al. 2016), consistent with Planck observations (Juvela et al. 2015) and joint *Herschel*/SCUBA-2 fits to GBS data (Chen et al. 2016; Sadavoy et al. 2013). While some localised variation in β around this value is seen in some GBS regions (Sadavoy et al. 2013; Chen et al. 2016; Pattle et al. 2025), $\beta = 1.8$ is a good representative value for determining the masses of the cores in our catalogue. In our choice of $\kappa_\nu(10^{12} \text{ Hz}) = 0.1 \text{ cm}^2 \text{ g}^{-1}$, we have implicitly assumed a dust-to-gas mass ratio of 1:100 (Beckwith et al. 1990).

Our assumed distances to the various clouds surveyed are taken from recent *Gaia* measurements, and are listed in Table 5. Cloud

Table 5. A summary of the classification of the sources in our catalogue by region.

Region	Total Sources	Starless	Protostellar	24 μ m-bright ('Heated')	Galaxy	Resolved	Unresolved
Aquila	312	191	85	34	2	284	28
Auriga	93	44	43	6	0	79	14
Cepheus L1228	8	5	2	1	0	7	1
Cepheus L1251	14	8	5	0	1	14	0
Cepheus South	21	9	12	0	0	16	5
CrA	33	15	16	2	0	25	8
IC5146	71	33	32	5	1	67	4
Lupus	9	5	4	0	0	9	0
Ophiuchus L1688	119	60	52	6	1	91	28
Oph L1689/1709/1712	34	22	10	2	0	27	7
Oph/Scorpius N2	1	0	0	1	0	1	0
Orion A	731	418	305	0	8	685	46
Orion B L1622	11	4	7	0	0	11	0
Orion B N2023	187	143	44	0	0	172	15
Orion B N2068	169	113	55	0	1	146	23
Perseus IC348	39	21	15	2	1	32	7
Perseus West	146	77	61	5	3	125	21
Pipe B59	10	1	9	0	0	4	6
Pipe E1	1	1	0	0	0	1	0
Serpens East	68	64	4	0	0	66	2
Serpens Main	73	31	38	4	0	63	10
Serpens MWC297	19	9	9	1	0	13	6
Serpens North	23	18	5	0	0	22	1
Taurus B18 East	17	9	8	0	0	12	5
Taurus B18 West	1	0	1	0	0	0	1
Taurus L1495	32	15	16	0	1	23	9
Taurus TMC1	15	5	9	1	0	9	6
Total	2257	1321	847	70	19	2004	253

distances vary from 134 pc (Oph/Sco N2) to 751 pc (IC 5146). With the exception of IC 5146, all clouds are located within 500 pc of the Solar System.

4.2.3 Deconvolved source sizes

We calculate deconvolved source sizes for sources extended relative to the beam at 850 μ m. The deconvolved radius, R , is taken to be the geometric mean of the major and minor FWHMs measured at 850 μ m, with the JCMT 850 μ m effective beam FWHM subtracted in quadrature, i.e.

$$R = D \tan \left(\text{FWHM}_A \text{FWHM}_B - \theta_{\text{eff}}^2 \right)^{\frac{1}{2}}, \quad (3)$$

where $\theta_{\text{eff}} = 14.4''$ is the effective FWHM beam size of the JCMT at 850 μ m (Dempsey et al. 2013) and D is the distance to the source.

Unresolved sources (i.e. those which are not extended along either axis relative to the 850 μ m beam) are classified as such in Table 3. Their 'deconvolved' size is taken to be the spatial extent of the FWHM 850 μ m beam at the distance of the source, although we largely excluded these sources from our discussions of source size (see Section 5.4, below). We find that 266 sources are unresolved, 11.8% of the catalogue. Of these, 208 are protostellar sources (24.7% of the protostellar sample), and 58 are starless cores (4.4% of the starless core sample).

4.2.4 Column and volume density

We determine mean H_2 column densities for our sources using the equation

$$N(\text{H}_2) = \frac{M}{\pi \mu_{\text{mol}} R^2}, \quad (4)$$

and mean H_2 volume densities using the equations

$$n(\text{H}_2) = \frac{M}{\frac{4}{3} \pi \mu_{\text{mol}} R^3}, \quad (5)$$

taking a mean molecular weight of $\mu_{\text{mol}} = 2.86$ (assuming the gas is 70% H_2 by mass; Kirk et al. 2013). Assuming a mean particle mass of 2.3 amu, our H_2 number densities can be converted to total gas particle number densities by multiplication by a factor of 1.24.

4.2.5 Bonnor–Ebert mass

We assess the stability of the starless cores in our catalogue using the Bonnor–Ebert (BE) stability criterion. The BE model (Ebert 1955; Bonnor 1956) treats a core as an isothermal, self-gravitating, polytropic sphere bounded by external pressure. The mass at which an isothermal BE sphere of temperature T is critically stable against gravitational collapse is a widely-used proxy for the virial mass (e.g. Könyves et al. 2015, and refs. therein), and is given by

$$M_{\text{BEC}} = 2.4 \frac{c_s^2}{G} R_{\text{BEC}} = 2.4 \frac{k_B T}{\mu_{\text{mol}} m_H G} R_{\text{BEC}}, \quad (6)$$

where $c_s = \sqrt{k_B T / \mu_{\text{mol}} m_H}$ is the sound speed and R_{BEC} is the radius at which the critically-stable Bonnor–Ebert (BEC) sphere is bounded by the gas pressure of its surroundings.

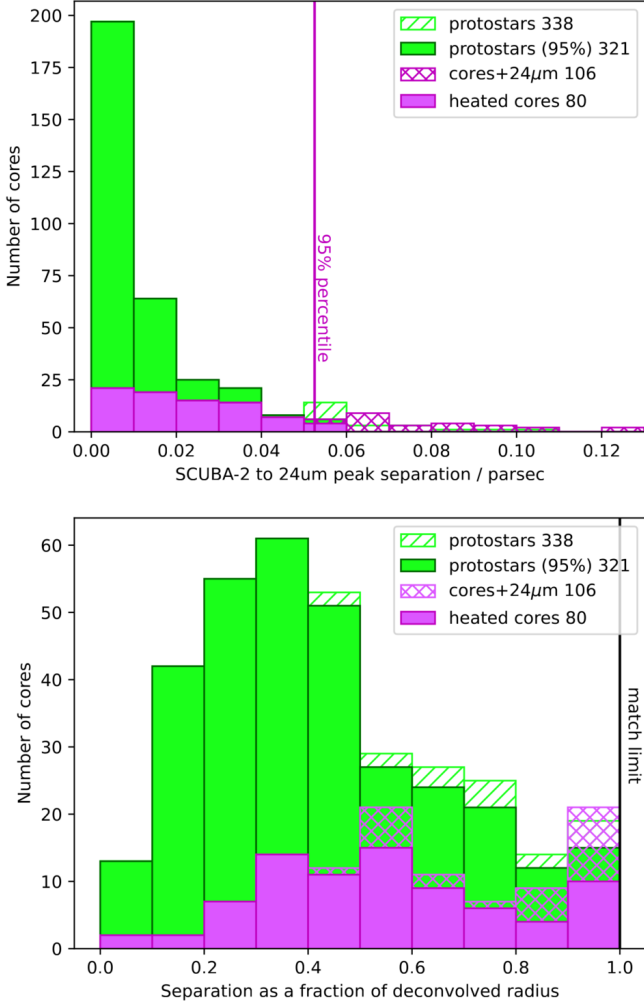


Figure 7. The distribution of separations between the SCUBA-2 core peak and the nearest $24\ \mu\text{m}$ *Spitzer* source as a function of distance (top panel) and as a fraction of core effective diameter (bottom panel). Cores already classified as protostellar are shown in green and cores reclassified from starless to ‘heated’ (i.e. potentially protostellar) due to a $24\ \mu\text{m}$ counterpart are shown in magenta, before (hashed) and after (solid) applying a 95% percentile separation cut. Only those starless cores which remain associated with $24\ \mu\text{m}$ emission after the 95% separation cut are reclassified as heated in the final catalogue.

The ratio of a core’s BEC mass to its measured mass,

$$\alpha_{\text{BEC}} = \frac{M_{\text{BEC}}}{M}, \quad (7)$$

is thus analogous to the virial stability ratio. A value of $\alpha_{\text{BEC}} < 1$ implies that a core is gravitationally unstable, while $\alpha_{\text{BEC}} > 1$ implies that a core can be supported against collapse by its internal thermal pressure. In keeping with standard practice, we consider those cores with $\alpha_{\text{BEC}} < 2$ as being potentially gravitationally unstable (e.g. Könyves et al. 2015). This choice follows from a similar assumption, that cores with a virial ratio < 2 can be considered likely to be gravitationally bound (cf. Bertoldi & McKee 1992). We emphasise that we are not suggesting that the cores in our catalogue have Bonnor–Ebert density profiles; we are simply comparing their masses to those of BEC spheres of the same size, and from this widely-used comparison identifying the cores most likely to be gravitationally bound.

To infer the BEC masses of our cores, we first needed to determine

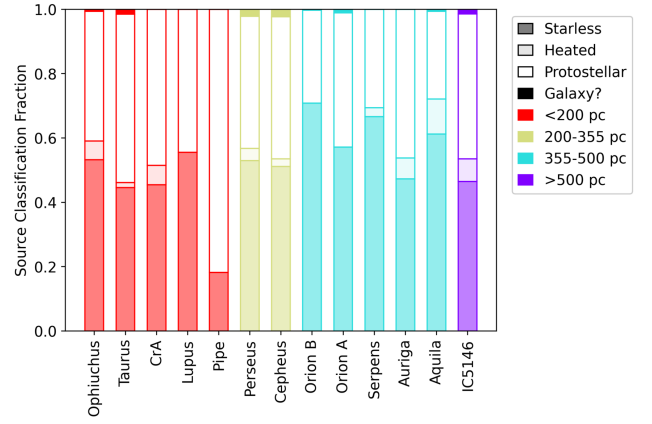


Figure 8. Bar chart summarizing source classification statistics for each cloud complex. The complexes are plotted in order of average distance from the Sun. Bars are colour-coded by distance, with opacity denoting source classification.

the relationship between *getsources* FWHM and R_{BEC} . For this purpose, we compared the geometric mean of the source sizes returned in our completeness fields, deconvolved with the JCMT beam, with their input BEC radii. The results are shown in Figure 9. We found

$$\langle \text{FWHM} \rangle_{\text{deconv}} (") = (0.75 \pm 0.03) \theta_{\text{BEC}} (") - (3.60 \pm 0.97), \quad (8)$$

and so,

$$\theta_{\text{BEC}} (") = (1.33 \pm 0.01) \langle \text{FWHM} \rangle_{\text{deconv}} (") + (4.80 \pm 0.97). \quad (9)$$

Note that this equation gives an effective BEC radius for an unresolved source ($\langle \text{FWHM} \rangle_{\text{deconv}} = 0$) of $4.8''$, approximately 1/3 of the $850\ \mu\text{m}$ primary beam size. We adopt this angular radius for unresolved sources in the following stability analysis, noting that only 4.4% of our starless core sample is unresolved.

We further note that our completeness testing indicates that typically, $73 \pm 6\%$ of the mass of a BEC sphere will be recovered by SCUBA-2. We therefore empirically define the effective BEC masses of the sources we detect to be

$$M_{\text{BEC,eff}} = 0.73 \times 2.4 \frac{c_s^2}{G} D \tan \theta_{\text{BEC}}. \quad (10)$$

Although 15 K is a typical temperature for unheated cores, a gravitationally-bound prestellar core may have temperatures as low as ~ 10 K, as discussed in Section 4.2.1. In order to identify starless cores which are good candidates for being gravitationally bound (‘prestellar’), we therefore calculate α_{BEC} if the core were at a temperature of 10 K,

$$\alpha_{\text{BEC},10\text{K}} = \frac{M_{\text{BEC,eff}}(T = 10\text{K})}{M(T = 10\text{K})}. \quad (11)$$

We consider cores with $\alpha_{\text{BEC},10\text{K}} < 2$ (i.e. bound at 10 K) to be ‘candidate’ prestellar cores.

We further consider a more stringent criterion for core boundedness by calculating α_{BEC} at the temperature assigned to the core in our catalogue (15 K, or greater if the core is heated), such that

$$\alpha_{\text{BEC},\geq 15\text{K}} = \frac{M_{\text{BEC,eff}}(T)}{M(T)}, \quad (12)$$

where T is the temperature listed in Table 3. We consider those cores with $\alpha_{\text{BEC},\geq 15\text{K}} < 2$ to be ‘robust’ prestellar cores.

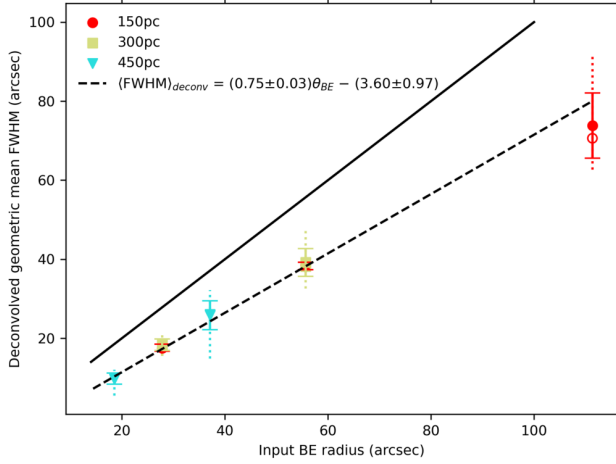


Figure 9. Measured deconvolved geometric mean FWHM vs input BEC radius, from completeness testing. Solid symbols show means, open symbols show medians, error bars show $1-\sigma$ uncertainties, dotted line shows full range. The straight lines show the 1:1 relationship (solid) and best fit (dashed).

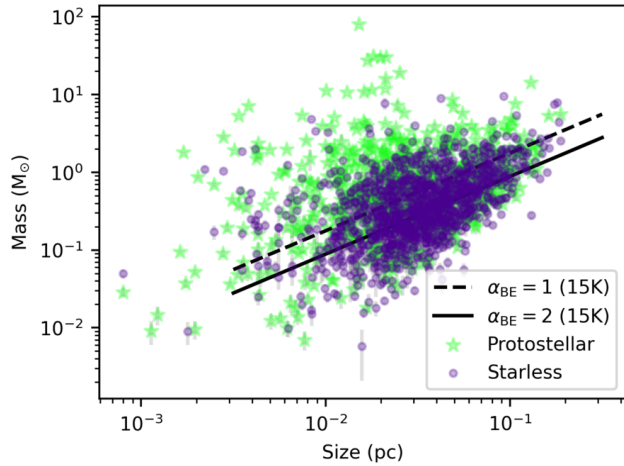


Figure 10. Source mass as a function of source size for the resolved sources in our catalogue. Blue circles mark starless cores; green stars mark protostellar sources. The solid black line marks the locus of a 15 K core with a BEC mass ratio of 2, while the dashed black line marks that of a 15 K core with a BEC mass ratio of 1.

5 DISCUSSION OF CORE PROPERTIES

To increase the sample sizes of starless cores to statistically meaningful levels, we considered our set of observed fields to represent 12 ‘cloud complexes’: Aquila, Auriga, Cepheus (Cepheus L1228, L1251 and South), IC 5146, Lupus, Ophiuchus (Ophiuchus L1688, L1689/1709/1712, and Oph/Sco N2), Orion A, Orion B (L1622, N2023 and N2068), Perseus (IC348 and Perseus West), Pipe, Serpens (Serpens East, Main and MWC297), and Taurus (Taurus B18, L1495 and TMC-1). We estimated the mass of potentially star-forming gas in each cloud complex using column density maps created from *Herschel* SPIRE and PACS measurements by the *Herschel* Gould

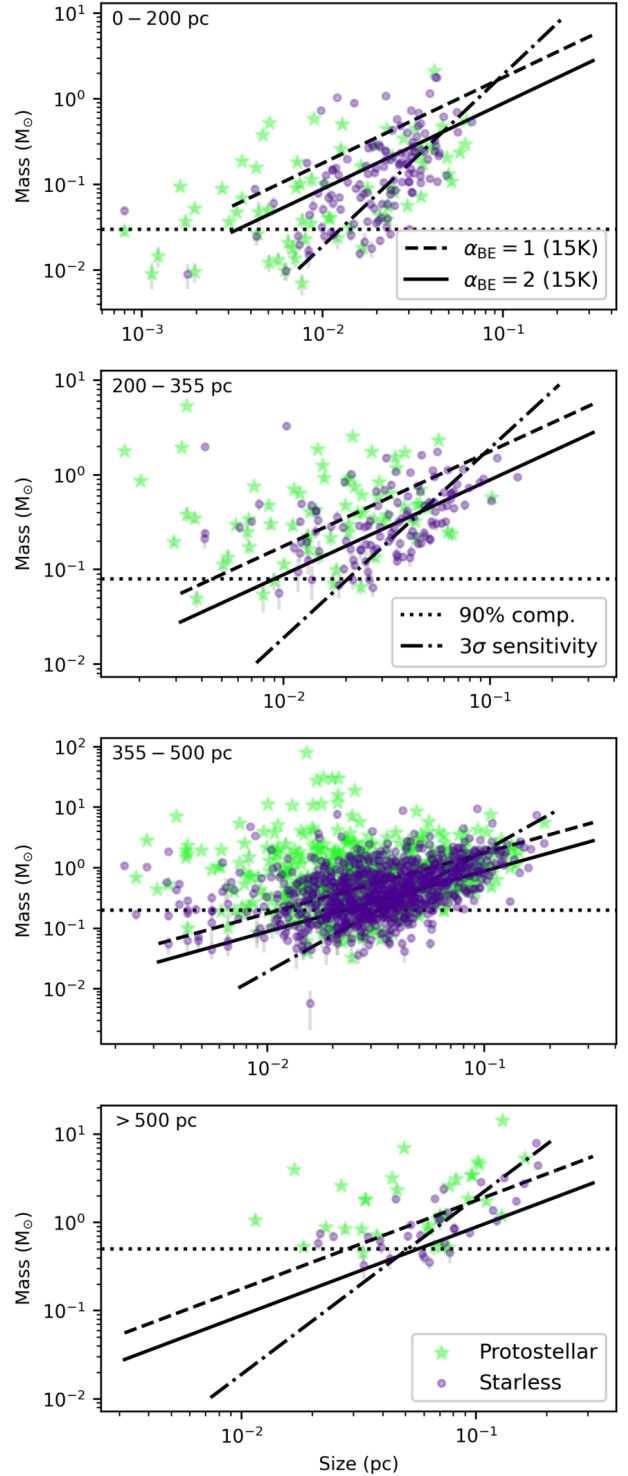


Figure 11. Source mass as a function of source size for resolved sources, separated by source distance. *Top panel:* near (< 200 pc), *second panel:* mid-distance (200–355 pc), *third panel:* far (355–500 pc), *bottom panel:* very far (> 500 pc). Data points are as in Figure 10. Solid black lines mark the locus of a 15 K core with a BEC mass ratio of 2, dashed black lines mark that of a 15 K core with a BEC mass ratio of 1, and the dotted black lines mark 90% mass completeness limit in each distance range.

Table 6. Potentially star-forming gas mass in each cloud complex, as measured from *Herschel* column density maps.

Cloud complex	Average distance (pc)	<i>Herschel</i> Mass (M_{\odot})	<i>Herschel</i> Reference
Aquila	484	14312	Könyves et al. (2015)
Auriga	470	6661	Harvey et al. (2013)
Cepheus	347	431	Di Francesco et al. (2020)
CrA	151	102	Bresnahan et al. (2018)
IC 5146	751	902	Arzoumanian et al. (2011)
Lupus	151	26	Rygl et al. (2013)
Ophiuchus	140	598	Ladjetate et al. (2020)
Orion A	432	12918	Roy et al. (2013)
			Polychroni et al. (2013)
Orion B	423	3919	Schneider et al. (2013)
Perseus	308	1543	Sadavoy et al. (2014)
			Pezzuto et al. (2021)
Pipe	180	34	Peretto et al. (2012)
Serpens	447	5443	Fiorellino et al. (2021)
Taurus	141	406	Kirk et al. (2013)
			Marsh et al. (2016)
			Kirk et al. (2024)
			J. Kirk (priv. comm.)

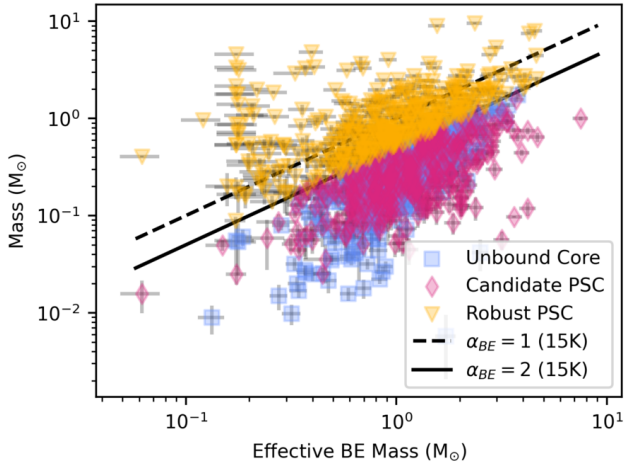


Figure 12. Source mass as a function of effective BEC mass, for the resolved starless cores in our sample. Blue squares mark unbound cores, red diamonds mark candidate prestellar cores ($\alpha_{\text{BEC}, 10\text{ K}} < 2$), and yellow triangles mark robust starless cores ($\alpha_{\text{BEC}, \geq 15\text{ K}} < 2$). The solid black line marks the locus of a 15 K core with a BEC mass ratio of 2, while the dashed black line marks that of a 15 K core with a BEC mass ratio of 1.

Belt Survey (André et al. 2010)⁶, except for the Auriga molecular cloud, for which we used column density maps published by Harvey et al. (2013). We summed the mass at column densities $N(\text{H}_2) > 7 \times 10^{21} \text{ cm}^{-2}$, to encompass the densest gas that is likely involved with star formation (e.g. Könyves et al. 2015; Di Francesco et al. 2020; Könyves et al. 2020; Pezzuto et al. 2021). These ‘star-forming’ gas masses are listed in Table 6 for each cloud complex.

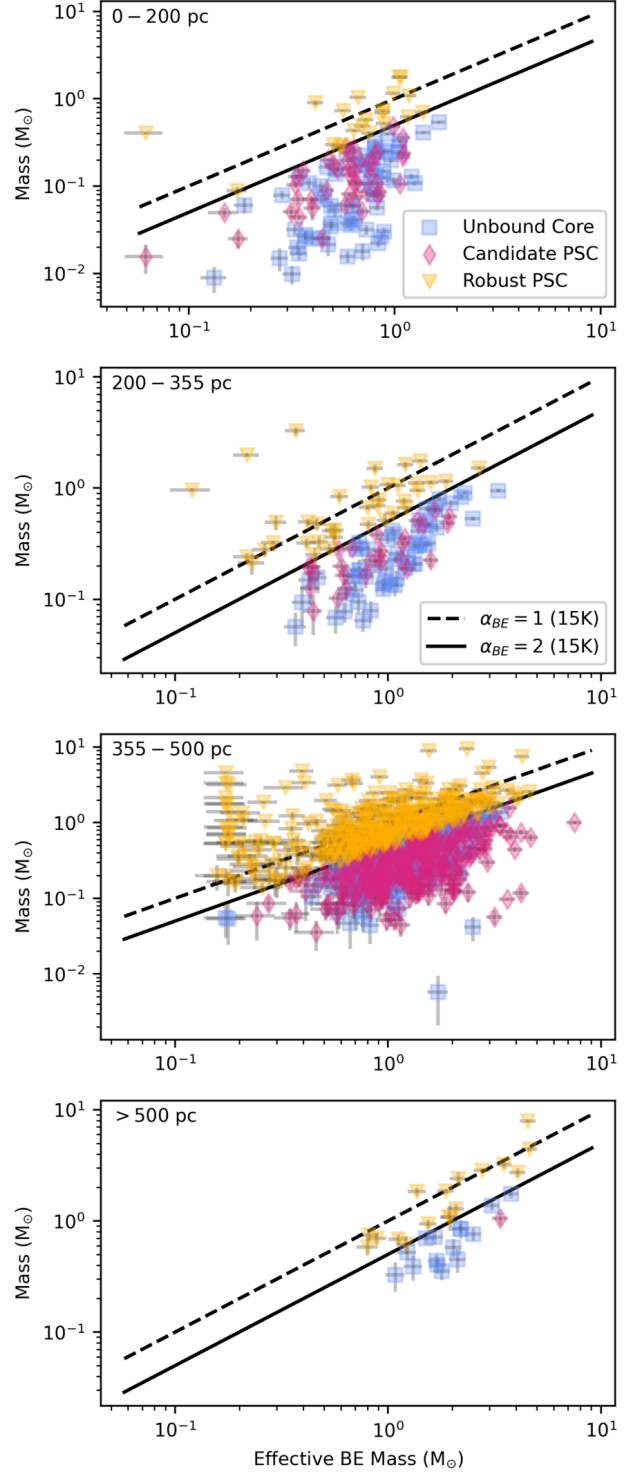


Figure 13. Source mass as a function of effective BEC mass, for the resolved starless cores in our sample, separated by source distance. *Top panel:* Near (< 200 pc). *Second panel:* Mid-distance (200–355 pc). *Third panel:* Far (355–500 pc). *Bottom panel:* Very far (> 500 pc). Data points are as in Figure 12. The solid black lines mark the locus of a 15 K core with a BEC mass ratio of 2, while the dashed black lines mark that of a 15 K core with a BEC mass ratio of 1.

⁶ Column density maps are available at <http://www.herschel.fr/cea/gouldbelt/en/>

Table 7. Core counts and classifications in each cloud complex.

Complex	Core Counts		Starless Core Classes		
	Protostellar	Starless	Robust Prestellar	Candidate Prestellar	Unbound
Aquila	119	191	47	141	3
Auriga	49	44	14	15	15
Cepheus	20	22	5	5	12
CrA	18	15	2	10	3
IC5146	37	33	17	1	15
Lupus	4	5	1	0	4
Ophiuchus	71	82	14	29	39
Orion A	305	418	157	149	112
Orion B	106	260	95	103	62
Perseus	83	98	32	22	44
Pipe	9	2	0	0	2
Serpens	61	122	66	4	52
Taurus	35	29	4	5	20
Total	917	1321	454	484	383

5.1 Mass vs. size

For our resolved sources, we plotted mass as a function of deconvolved geometric mean size. The mass/size diagram for our full sample of sources is shown in Figure 10, while the mass/size diagrams for each of our distance bins are shown in Figure 11. For each panel in Figure 11, our estimated 90% completeness limit is shown as a dotted line, while our estimated $3\text{-}\sigma$ sensitivity is shown as a dashed line.

We calculated our $3\text{-}\sigma$ mass sensitivity using an assumed per-pixel $1\text{-}\sigma$ mass sensitivity of $0.047 \text{ mJy arcsec}^{-2}$, which we measured using aperture photometry on the Oph/Sco N6 field (the field into which fake sources were inserted for the completeness testing, as described in Section 3.4 and Appendix B). The dashed lines shown in Figure 11 show the mass of a 15 K source at the nominal distance, in which each pixel has a $3\text{-}\sigma$ flux density.

We note that some sources appear below our $3\text{-}\sigma$ mass sensitivity limit. This apparent incongruity is likely to be due to some combination of non-uniform flux densities across real sources, many sources sitting on bright backgrounds, and so being easier to detect than sources sitting on the noisy background of the map, and slight differences in sensitivity between maps, due to combinations of mosaicking strategy, weather conditions in which the observations were made, and small differences in exposure time.

Gravitationally bound objects are expected to occupy the upper left-hand portion of the mass-size diagram, being massive and relatively compact. This characteristic is demonstrated in Figure 11 by the diagonal lines marking the effective BEC mass (and half of the effective BEC mass) for sources at 15 K. As distance increases, our completeness and mass sensitivity limits progressively exclude a larger area of the gravitationally unbound region of the mass-size plane, and so at greater distances we preferentially detect gravitationally bound and collapsing cores.

5.2 Core stability

We calculated effective BEC masses for all of the starless cores in our sample, as described in Section 4.2.5. Core mass is plotted as a function of effective BEC mass in Figure 12, with both measured mass and BEC mass calculated for $T \geq 15 \text{ K}$. Both robust ($\alpha_{\text{BEC}, \geq 15 \text{ K}} < 2$) and candidate ($\alpha_{\text{BEC}, 10 \text{ K}} < 2$) prestellar cores are marked on the fig-

ure. Core masses as a function of BEC mass are also plotted for each of our distance ranges in Figure 13. As expected, fewer unbound cores are detected in the more distant clouds, likely as a matter of sensitivity. Although more distant cloud complexes have a higher bound core fraction, there is no clear correlation with cloud mass within any given distance range (cf. Figure C2).

Note also that a large fraction of starless cores found in SCUBA-2 GBS maps have previously been found to be stable according to the BE criterion, or, in a virial analysis, confined by pressure rather than gravity (Pattle et al. 2015, 2017). This finding has been replicated in molecular line studies of dense cores (e.g. Kirk et al. 2017; Kerr et al. 2019). Magnetic fields may also play a significant role in supporting these cores against gravitational collapse (e.g. Myers & Basu 2021; Pattle et al. 2021). Thus, additional information is required to determine the exact virial state of the starless cores in our sample.

5.3 Relative numbers of protostellar and starless cores

The fraction of starless cores is plotted as a function of cloud mass for each cloud complex in Figure 14, based on numbers in Table 7. On average, 41% of the detected cores are protostellar and 59% are starless. Of the starless cores, 34% are robust prestellar cores, 37% are candidate prestellar cores, and 29% are unbound. Thus, 41% of our cores are protostellar and 42% are prestellar (either candidate or robust). Assuming all prestellar cores (candidate and robust) are the precursors of protostars, then similar source counts indicate similar lifetimes to Class 0/I embedded YSOs (0.5 Myr; Evans et al. 2009), which are consistently detected by the JCMT GBS as protostellar cores. If every core passes through the ‘robust’ prestellar core phase, then it lasts half as long on average (0.25 Myr).

The starless and prestellar core fractions vary between complexes, and the differences are statistically significant. We tested for consistency using a binomial distribution, checking core counts against the 95% confidence interval and the two-tailed binomial test with 5% significance, and with two hypotheses, setting the starless or prestellar core probability equal to the mean starless or prestellar core fraction, (1) averaged over all cores ($p = 0.59, 0.42, 0.20$ for starless, prestellar and robust prestellar cores respectively; note the core counts are dominated by Orion A); (2) averaged over all regions, with equal weight for each region ($p = 0.52, 0.30, 0.15$ for starless,

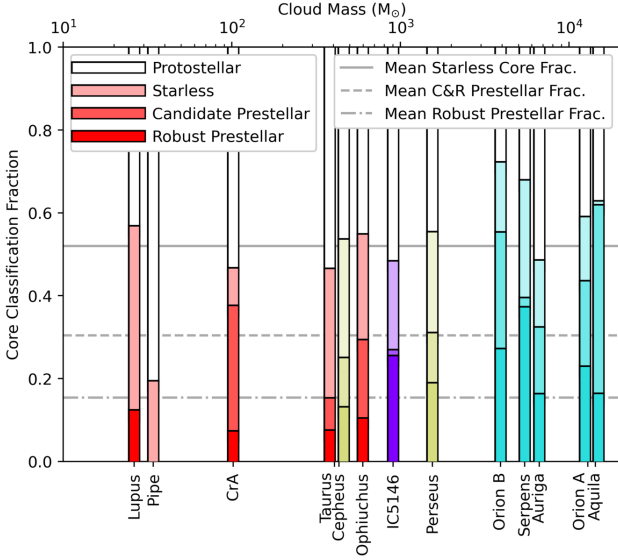


Figure 14. The fraction of cores within a cloud complex which are starless cores, candidate prestellar cores, robust prestellar cores, and protostellar cores as a function of cloud complex mass. Grey lines show the average fractions of starless (solid line), prestellar (candidate and robust; dashed line) and robust prestellar (dot-dashed line) cores averaged over all regions, as discussed in Section 5.3. Data points are colour-coded by cloud distance. Note that the bars for Taurus, Cepheus, Orion A and Aquila are slightly offset from their true positions, to avoid overlap. The tick marks associated with these bars show the exact cloud masses.

prestellar and robust prestellar cores respectively). For each hypothesis and type of core selected, at least four regions and up to eight regions had source counts that were not consistent with the average probability. Under both hypotheses, Serpens and Orion B have an excess of starless and prestellar cores, whereas Pipe and Taurus show a deficit.

Under Hypothesis (1), where average core counts are dominated by Orion A, many more of the lower and intermediate mass regions had a deficit of starless or prestellar cores (Auriga for starless cores; Auriga, Cepheus, Ophiuchus and Perseus for candidate prestellar cores; CrA and Ophiuchus for robust prestellar cores) while IC 5146 showed an excess but only for robust prestellar cores. Under Hypothesis (2), Orion A also had an excess of starless and prestellar cores (IC 5146 showed an excess and Ophiuchus a deficit for robust prestellar cores only).

The trend is for higher-mass regions to have a higher ratio of starless (or prestellar) cores compared to protostars (Fig. 14; see also Figure C1). Assuming candidate prestellar cores are the precursors of protostars, then a higher ratio indicates a longer lifetime for prestellar cores in higher mass regions, on average, compared to those in lower mass regions. This could be due to longer average freefall times in larger, lower average density clouds (see Pokhrel et al. 2021, and references therein). If this is the case, then prestellar cores should show a wider spatial distribution than protostars, with less concentration in high (column) density regions. There is already some evidence that this is the case: in Orion B, the surface density of prestellar cores follows a linear relationship with column density whereas the surface density of protostellar cores scales nonlinearly as the square of column density (Könyves et al. 2020; Lombardi et al. 2014; Pokhrel et al. 2020; Retter et al. 2021).

One might expect clouds with a large fraction of Class 0/I sources compared to more evolved YSOs also to have a large number of star-

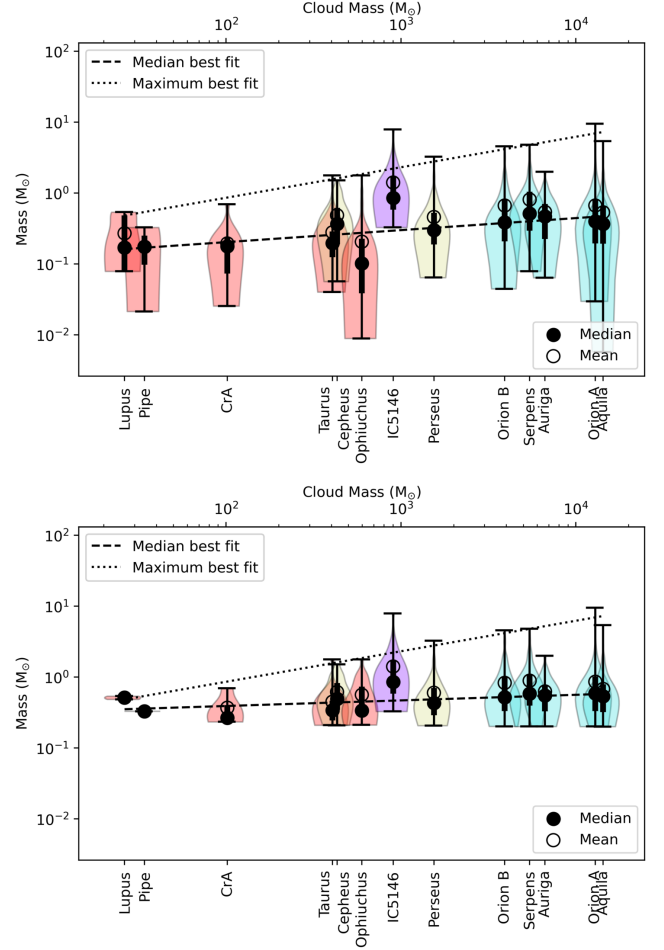


Figure 15. Mass distribution for each cloud complex, as a function of star-forming gas mass. Top: for all starless cores. Bottom: for starless cores with masses above the 90% completeness limit at 450 pc of $0.2 M_{\odot}$. Solid circles show median values; open circles show means. Thick black lines show the interquartile ranges. Dotted line shows the line of best fit to the maximum values in each cloud complex; dashed line shows the line of best fit to the median values.

less cores, as that could indicate a ramp-up in recent star formation. From the *Spitzer* Gould Belt survey, the highest fraction of Class 0/I YSOs occur in Auriga, IC 5146, and Perseus (Dunham et al. 2015). From the data presented here, there is nothing special about the starless core fractions in these clouds – only a slight indication that it might be low in Auriga – suggesting that star formation will continue at the same rate in the future.

5.4 Mass and radius distributions

We plot the distribution of starless core masses as a function of potentially star-forming gas mass for each complex in Figure 15. We find a moderately strong correlation between median starless core mass and cloud complex mass, with $M_{\text{median}} \propto M_{\text{cloud}}^{0.17 \pm 0.06}$ ($r = 0.62$, $p = 0.02$), determined using least-squares fitting. However, this relationship may be influenced by the differing mass completeness limits between the different cloud complexes, with more massive clouds typically being more distant, and so we plotted the starless core mass distributions for each complex above the mass completeness

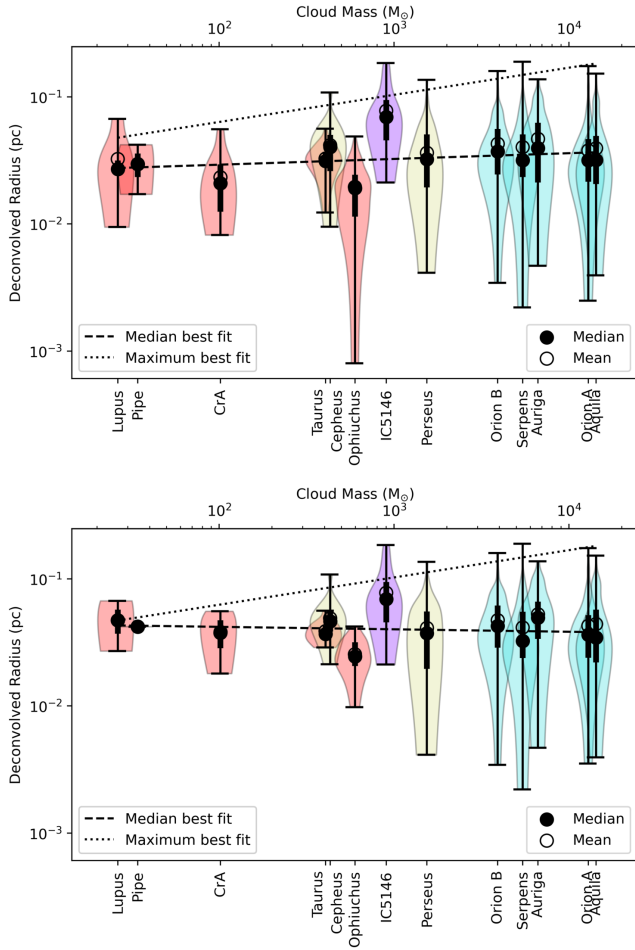


Figure 16. Deconvolved radius distribution for starless cores for each cloud complex, as a function of star-forming gas mass. Top: for all starless cores. Bottom: for starless cores with masses above the 90% completeness limit at 450 pc of $0.2 M_{\odot}$. Solid circles show median values; open circles show means. Thick black lines show the interquartile ranges. Dotted line shows the line of best fit to the maximum values in each cloud complex; dashed line shows the line of best fit to the median values.

limit at 450 pc of $0.2 M_{\odot}$. The best-fit relationship between cloud complex mass and median mass becomes shallower and less robust, with $M_{\text{median}}(> 0.2 M_{\odot}) \propto M_{\text{cloud}}^{0.08 \pm 0.04}$ ($r = 0.53$, $p = 0.06$).

At a later evolutionary stage, the maximum stellar mass in a cluster increases with embedded cluster mass (Weidner et al. 2010; Elmegreen 2006). The relationship between stellar and cluster mass was examined by Bonnell et al. (2004), who found the mass of the most massive star in a cluster scaled with cluster mass to a power of $2/3$. We investigated whether we see a similar relationship between cloud mass and maximum core mass in the cloud complexes that we consider. We find a strong correlation between maximum starless core mass (M_{max}) and cloud complex mass (M_{cloud}) with $M_{\text{max}} \propto M_{\text{cloud}}^{0.58 \pm 0.13}$ ($r = 0.80$, $p < 0.005$), consistent with the Bonnell et al. (2004) index. The mass of the most massive core in a cloud thus typically increases with cloud mass (Figure 15), although the extent to which this can be directly linked to the relationship between stellar and cluster mass is unclear, since the larger cloud complexes in our sample typically contain larger numbers of cores, and so are more likely to contain high-mass outliers.

We also see significant cloud-to-cloud variation in mass distributions in clouds at comparable distances. Notably, the Ophiuchus molecular cloud has significantly more low-mass sources than are seen in any of the other nearby clouds, and a significantly lower minimum core mass.

We note that there is also a correlation between maximum and median mass and cloud distance, as might be expected from eq. 1. These relationships are shown in Figure D1 in Appendix D. However, the relationships between mass and distance are shallower than D^2 , indicating that the correlation that we see between core and cloud masses is not solely due to more massive clouds on average being at a greater distance from us.

We further plotted the distribution of starless core deconvolved radii as a function of potentially star-forming gas mass for each complex, both for all starless cores and for cores above the 450 pc mass completeness limit, as shown in Figure 16. We see no correlation between the median deconvolved core size and the mass of the cloud in either case. However, in both cases we find a correlation between maximum deconvolved core size and cloud mass: for all cores, $R_{\text{max}} \propto M_{\text{cloud}}^{0.21 \pm 0.05}$ ($r = 0.81$, $p < 0.005$). For cores above the 450 pc mass completeness limit, $R_{\text{max}}(> 0.2 M_{\odot}) \propto M_{\text{cloud}}^{0.21 \pm 0.05}$ ($r = 0.79$, $p < 0.005$).

We also investigated the relationship between maximum and median deconvolved core radius, as shown in Figure D2 in Appendix D, and find that both median and maximum core radii are correlated with distance when all cores are considered, while when only cores above the 450 pc mass completeness limit are considered, there is no correlation between median core radius and cloud distance. However, in both cases, we find a relationship consistent within error with $R_{\text{max}} \propto D$. Despite this, we find considerable variation between core radius distributions for clouds at similar distances to one another: Ophiuchus has a significantly smaller minimum source size and a considerable excess of small cores compared to other nearby clouds, while Cepheus has a significantly smaller spread in core radii than does Perseus, despite the two clouds being at comparable distances.

6 CORE MASS FUNCTIONS

The mass distribution of starless, or prestellar, cores is typically characterised using the Core Mass Function (CMF). The form of the CMF is similar to that of the Initial Mass Function (IMF; Salpeter 1955; Kroupa 2001; Chabrier 2003), with a log-normal behaviour at low masses and a Salpeter-like power-law behaviour at high masses (e.g. Könyves et al. 2015) leading to the suggestion of a causal link between the CMF and the IMF (Motte et al. 1998). *Herschel* studies of dense cores in the Aquila molecular cloud have found that the characteristic mass of the prestellar CMF is $3\times$ that of the system IMF, suggesting a $\sim 33\%$ core-to-star mass conversion efficiency (Könyves et al. 2010, 2015). However, this relies on there being a 1:1 relationship between the CMF and the IMF, and so does not account for further core fragmentation (other than into bound multiple systems), or for the potential for further accretion of mass onto cores (Offner et al. 2014).

In keeping with standard practice, we visualised our measured CMFs by plotting histograms of the mass distributions of the starless cores in our catalogue, as shown in Figure 17, and Figures E2–E14 in Appendix E. In each case we used logarithmically-spaced bins, with the number of non-empty bins determined using Sturges’s Law, $N_{\text{bins}} = 1 + \log_2 N$, where N is the number of cores in the sample.

We modelled our measured starless core mass distributions, and

their candidate and robust prestellar subsets, using a log-normal mass distribution,

$$\frac{\Delta N}{\Delta \log_{10} M} \propto \exp\left(-\frac{(\log_{10} M - \log_{10} \mu)^2}{2\sigma^2}\right), \quad (13)$$

where μ is the mean core mass in units of M_{\odot} and σ is the width of the mass distribution in units of $\log_{10} M_{\odot}$. This distribution is comparable to the log-normal part of the Chabrier (2003) and Chabrier (2005) IMF.

6.1 Core Mass Functions by distance

CMFs for our four distance ranges, < 200 pc, $200 - 355$ pc, $355 - 500$ pc, > 500 pc, are shown in Figure 17. For the $355 - 500$ pc distance range, we also plotted the CMF with the heated cores of Orion A excluded, as shown in Figure E1 in Appendix E.

6.1.1 Least-squares fitting of CMFs by distance

We fitted a log-normal distribution to each of the CMFs for our four distance ranges, using the *scipy* least-squares fitting routine *curve_fit*. We fitted (i) the full distribution of starless cores, (ii) the distribution of prestellar cores (the combined candidate and robust samples; referred to as ‘C & R’), (iii) the distribution of unbound cores, (iv) the distribution of candidate prestellar cores, and (v) the distribution of robust prestellar cores. Note that samples (ii)–(v) are subsets of sample (i). The best-fit model CMFs for each distance range are plotted on Figures 17 and E1. The fitting results are shown in Table 8 for all starless cores and for prestellar cores (C & R). Fitting results for the unbound, candidate prestellar and robust prestellar samples are given in E1. In each case we fitted only those bins whose centres are above the mass completeness limit in that distance range. Where it is possible to fit the $355 - 500$ pc range with heated cores in Orion A excluded, in every case the results agree within error with those of the full far sample, and so we conclude that our choice of temperatures in Orion A makes little difference to the statistical properties of our sample. Henceforth, we use all cores in Orion A in our CMF fitting.

The near-, mid- and far-distance core mass distributions are well-modelled with log-normal distributions. No good log-normal fit could be found for the very far-distance starless CMF (i.e. IC 5146), likely because the peak of the starless CMF is below the completeness limit of the region. A log-normal fit can be found for the prestellar very far-distance CMF, albeit with very large uncertainties. Due to the difficulty in constraining the CMF of the very-far distance cores, and due to the high mass completeness limit at this distance, we do not consider this distance range further.

Our best-fit models show that the peak of the log-normal CMF model (the most probable core mass) increases with distance. The peak of the prestellar CMF is consistently higher than that of the starless core CMF, as expected, as more massive cores are more likely to be gravitationally bound. The starless and prestellar CMFs have similar widths in each case. We find that the near-distance CMFs are ≈ 0.1 dex – 0.15 dex wider than those of the mid- and far-distance CMFs, whose widths are consistent with one another.

The peak of the CMF is well above the mass completeness limit for both the near- and the mid-distance samples. We can see a clear downturn in the distribution of core masses before the completeness limit is reached, suggesting that we are accurately characterising the low-mass ends of these CMFs. However, the peak mass of the far-distance sample is near the completeness limit, suggesting that the

low-mass end of the CMF is less well-characterised here. The best-fit starless CMF for the far-distance sample follows the data below the completeness limit well, perhaps suggesting that our completeness limit is conservative. However, the best-fit prestellar CMF is narrower, and does not encompass the cores detected below the 90% completeness limit.

6.1.2 Similarity of CMFs at different distances

We wish to determine whether or not the near-, mid- and far-distance core samples could be drawn from the same underlying CMF, i.e. whether differences in the best-fit CMFs result from their differing completeness limits. To test this hypothesis, we first attempted to fit log-normal distributions to the cores in the near- and mid-distance samples only for masses above the $0.2 M_{\odot}$ completeness limit of the far-distance sample. In the near-distance case, there were too few cores with masses $> 0.2 M_{\odot}$ to produce a good fit, while in the mid-distance case the fits produced were poorly constrained, with lower peak masses and broader widths. The parameters of these fits are listed in Table 8.

6.1.3 Monte Carlo modelling of CMFs by distance

To further test the consistency of the starless and prestellar CMFs as a function of distance, we constructed a grid of log-normal CMFs, with parameters in the range $-1.5 \leq \log_{10} \mu \leq 0.0$ and $0.05 \leq \sigma \leq 1.2$, in steps of 0.0125 . From each of these CMFs we randomly drew a sample of ‘cores’ 100 times larger than the size of the far-distance starless or prestellar sample (this number was chosen arbitrarily to ensure that the sample had a total mass significantly greater than that of the far-distance sample). We then calculated the cumulative sum of the sample, and selected the cores whose cumulative mass was closest to the total mass of the near-distance starless or prestellar sample (Bonnell et al. 2011). We further selected the cores whose cumulative mass was closest to the total mass of the mid- and far-distance starless or prestellar samples.

For each of these mass distributions, we selected masses above the near-, mid-, or far-distance completeness limits as appropriate. We then performed two-sided Kolmogorov-Smirnov (KS) tests between the sub-sample and the the above-completeness-limit core masses in the observed near-, mid- and far-distance starless or prestellar sample, respectively. We repeated this exercise 1000 times for each CMF in the grid, and recorded the median p values for the three distance bins. These median values are shown in Figure 18, and the most probable (highest p -value) combinations of μ and σ are listed in Table 9. In each case, there is a well-defined most probable log-normal CMF, with a long tail of marginally consistent CMFs with lower peak masses and larger widths. We note that the most probable values that we find for each distance range are consistent with the best-fit values from our least-squares fitting, suggesting that both methods are robustly characterising the CMFs that we measure.

The three prestellar CMFs are only marginally consistent at the $p = 0.05$ level with being drawn from the same underlying log-normal distribution. In the starless case, the three CMFs are slightly more consistent at the $p = 0.05$ level, although the area of parameter space over which the probability distributions overlap remains small. For both the starless and the prestellar samples, the mid-distance CMF is consistent at $p > 0.1$ with being drawn from the same underlying distribution as either the near- or the far-distance CMF, but the three cannot be simultaneously reconciled with each other. The $p > 0.5$ values of μ and σ for the three distributions do not

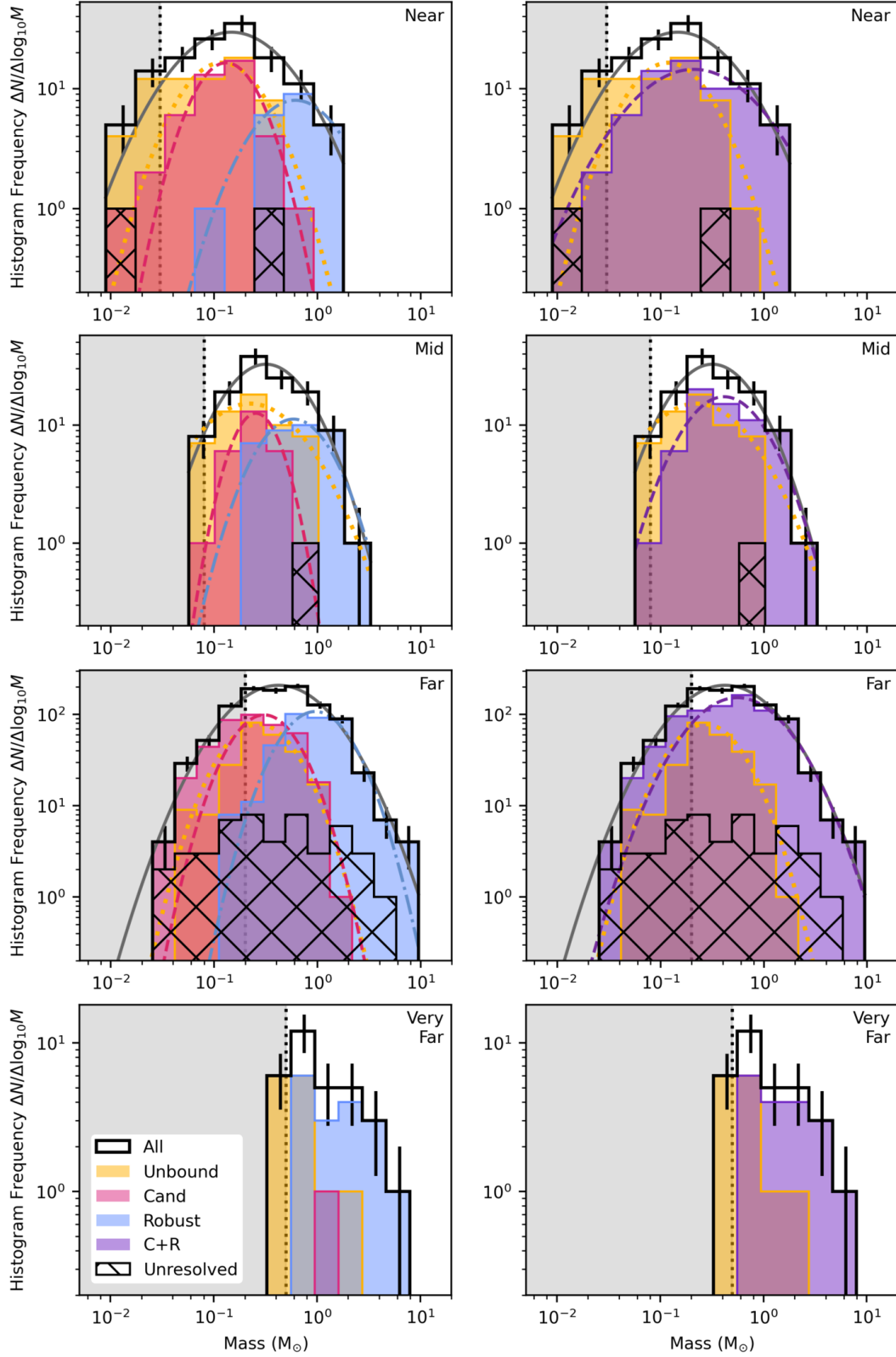


Figure 17. Starless CMFs for the distance ranges which we consider. Top to bottom: near, mid-distance, far and very far. Left column: CMFs with fits to full, unbound, candidate prestellar and robust prestellar samples shown. Right column: CMFs with fits to full, unbound, and combined candidate and robust (C & R) prestellar samples. In both columns, the unresolved sources are shown as a hatched histogram.

Table 8. Least-squares best-fit log-normal CMFs for each of our distance ranges, for all starless cores, and for prestellar cores (combined candidate and robust samples). The fitted parameters are A , maximum value of the log-normal, μ , mass at which the log-normal distribution peaks, and σ , log-normal width. The final two rows of the table show least-squares best fits to the near- and mid-distance samples, for cores above the far-distance mass completeness limit ($0.2 M_{\odot}$) only.

Range	Starless			Prestellar (C & R)		
	A	μ (M_{\odot})	σ ($\log_{10} M_{\odot}$)	A	μ (M_{\odot})	σ ($\log_{10} M_{\odot}$)
0 – 200 pc	30±3	0.15±0.02	0.48±0.05	15±2	0.21±0.04	0.53±0.09
200 – 355 pc	33±4	0.32±0.04	0.37±0.04	17±3	0.41±0.06	0.35±0.05
355 – 500 pc	208±13	0.42±0.05	0.42±0.03	150±10	0.56±0.05	0.39±0.03
no heated Orion A	205±4	0.48±0.02	0.41±0.01	151±3	0.64±0.02	0.38±0.01
> 500 pc	–	–	–	6 ± 2	0.7 ± 0.7	0.6 ± 0.3
For cores with masses > 0.2 M_{\odot} only						
0 – 200 pc	–	–	–	–	–	–
200 – 355 pc	36±7	0.2±0.1	0.4±0.1	19±4	0.3±0.2	0.4±0.1

Table 9. The most probable starless and prestellar CMFs for each distance range that we consider, as determined from Monte Carlo estimation and two-sided KS tests, using matched-mass sampling. p values show the probability that this model and our sample are drawn from the same underlying distribution.

Range	Starless			Prestellar (C & R)		
	μ (M_{\odot})	σ ($\log_{10} M_{\odot}$)	p	μ (M_{\odot})	σ ($\log_{10} M_{\odot}$)	p
0–200 pc	0.15	0.41	0.78	0.19	0.49	0.75
200–355 pc	0.32	0.36	0.70	0.41	0.36	0.68
355–500 pc	0.42	0.42	0.65	0.56	0.39	0.67

overlap in any case. It therefore seems unlikely that the CMFs of the three distance bins are drawn from the same underlying log-normal distribution, although we cannot rule this out entirely.

6.2 Core Mass Functions by cloud complex

6.2.1 Least-squares CMFs by cloud complex

We further fitted log-normal distributions to the CMFs of each of the cloud complexes which we observed. These distributions are shown in Figures E2–E14 in Appendix E, and their best-fit log-normal distributions are listed in Table 10. The Lupus and Pipe regions contain too few starless cores (< 10) to fit a CMF, and no prestellar cores. The Taurus region contains too few prestellar cores for a fit to be found. As discussed above, good log-normal fits cannot be found for IC 5146 (the very far-distance cores). We thus exclude IC 5146 from further consideration.

6.2.2 Monte Carlo CMFs by cloud complex

We performed the Monte Carlo modelling described in Section 6.1.3 for each of the cloud complexes which we observed. We did not attempt this modelling for complexes with sample sizes of less than 10. The results of this analysis are given in Table 11. The matched-mass sample contour plots are shown in Figures 19 (starless cores) and 20 (prestellar cores).

The most probable starless and prestellar CMFs are compared in Figure 21. The most probable prestellar CMF has a higher peak mass than the starless CMF in every cloud complex, as is expected as higher-mass cores are more likely to be gravitationally bound. In most complexes, the most probable prestellar CMF has a narrower

width than the starless CMF, with the exceptions of Ophiuchus and Perseus, both of which show a slight increase in width.

The best-fit least squares (LS) and most-probable Monte Carlo (MC)-derived CMFs are similar to one another; we compare them in more detail in Appendix E2.

6.2.3 CMF properties as a function of cloud mass

The peak starless and prestellar CMF masses, as determined from LS fitting, are plotted as a function of cloud complex mass (M_{cloud}) in Figure 22. The equivalent plots for the MC case are shown in Appendix E2. We see that in both cases there is a weak trend for peak mass to increase with cloud mass. Ophiuchus again has a considerably lower peak core mass than would be expected for a cloud of its mass.

We performed linear regressions on the data, fitting a power-law model, $\mu \propto M_{cloud}^{\gamma}$, to the data in logarithmic space. The best-fit values of γ are listed in Table 12, and the fits are plotted on Figures 22 and E17. We perform fits both with and without Ophiuchus; excluding Ophiuchus slightly reduces the best-fit value of γ in every case.

The values of γ listed in Table 12 are consistent with the relationship between cloud mass and median core mass, $M_{median} \propto M_{cloud}^{0.17 \pm 0.06}$, as shown in Figure 15. However, as discussed in Section 5.4, this latter trend is not robust when only cores above the 450 pc mass completeness limit are considered. The trend which we see in μ with M_{cloud} may therefore be in part a selection effect resulting from poor completeness of low-mass cores in the more distant clouds in our sample. Nonetheless, there is a lack of high-mass cores in the most nearby (typically lower-mass) clouds, suggesting that this trend is to some extent physical in origin.

Starless and prestellar CMF widths from LS fitting are plotted as a function of cloud complex mass in Figure 23, with the equivalent

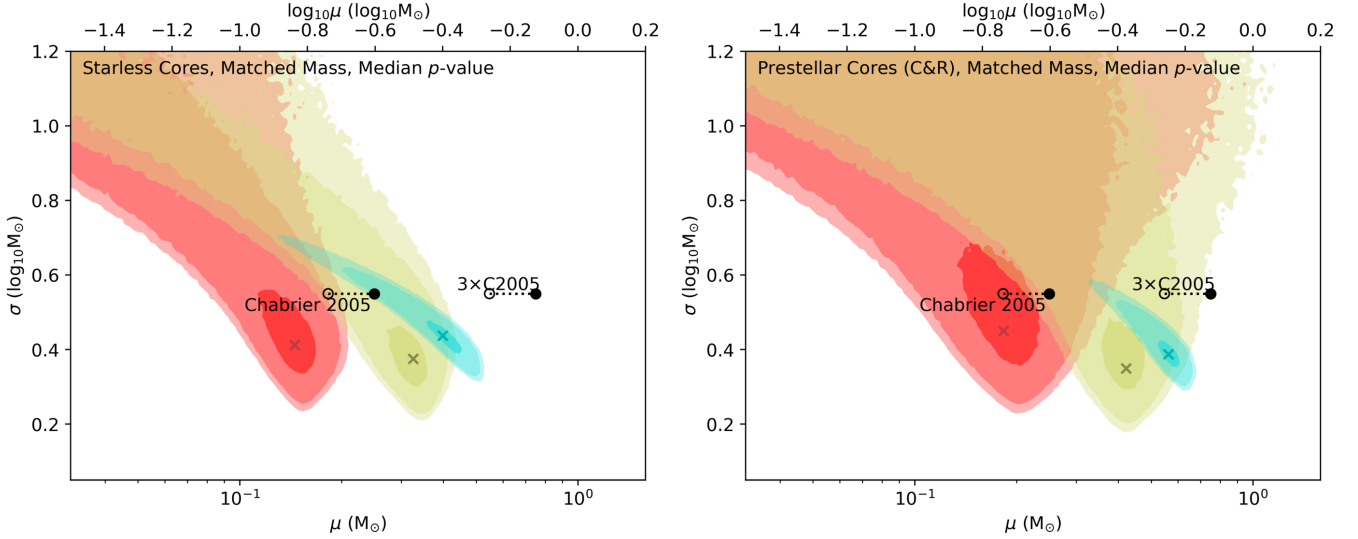


Figure 18. Median p -values for two-sided KS test between model CMFs and starless (left) and prestellar (right) CMFs, for matched-mass sampling. Contours show p values of 0.05, 0.1 and 0.5. Red marks near-, yellow mid- and cyan far-distance CMFs. Filled circles mark 1 and $3\times$ the Chabrier (2005) peak system mass ($0.25 M_{\odot}$). Open circles mark $0.73\times$ these values, accounting for the typical flux loss in our SCUBA-2 observations.

Table 10. Least-squares best-fit core mass functions for each of the cloud complexes that we consider.

Complex	Starless			C&R		
	A	μ (M_{\odot})	σ ($\log_{10} M_{\odot}$)	A	μ (M_{\odot})	σ ($\log_{10} M_{\odot}$)
Near						
CrA	3 ± 3	0.2 ± 0.2	0.7 ± 1.2	4.2 ± 1.1	0.19 ± 0.03	0.33 ± 0.10
Lupus	–	–	–	–	–	–
Pipe	–	–	–	–	–	–
Ophiuchus	19 ± 3	0.08 ± 0.06	0.6 ± 0.2	10 ± 2	0.13 ± 0.07	0.7 ± 0.3
Taurus	10 ± 1	0.20 ± 0.02	0.39 ± 0.04	–	–	–
Mid						
Cepheus	6 ± 1	0.4 ± 0.1	0.4 ± 0.1	–	–	–
Perseus	25 ± 3	0.30 ± 0.03	0.38 ± 0.03	15 ± 3	0.42 ± 0.05	0.36 ± 0.05
Far						
Aquila	48 ± 5	0.52 ± 0.06	0.32 ± 0.04	52 ± 3	0.45 ± 0.05	0.35 ± 0.03
Auriga	12 ± 4	0.5 ± 0.1	0.3 ± 0.1	8 ± 5	0.6 ± 0.2	0.2 ± 0.1
Orion A	100 ± 10	0.46 ± 0.08	0.41 ± 0.05	70 ± 10	0.6 ± 0.1	0.41 ± 0.07
Orion B	55 ± 4	0.25 ± 0.07	0.59 ± 0.07	43 ± 1	0.55 ± 0.04	0.45 ± 0.02
Serpens	31 ± 2	0.54 ± 0.08	0.43 ± 0.05	21 ± 5	1.0 ± 0.1	0.29 ± 0.04
Very Far						
IC5146	–	–	–	6 ± 2	0.7 ± 0.7	0.6 ± 0.3

plots for the MC case again shown in Appendix E2. There is no clear correlation with cloud complex mass or with distance in any case.

6.2.4 Comparisons between clouds

We find that the nearby clouds have different most-probable CMFs to those of the mid- and far-distance clouds. The mid-distance CMFs, while not particularly well-constrained, are broadly consistent with

the far-distance CMFs, all of which fall in the same area of $\mu - \sigma$ parameter space, as shown in Figures 21 and E16.

Nearby clouds: The starless core distributions of all of the nearby clouds are consistent with one another at the $p = 0.1$ level. Ophiuchus and Taurus are inconsistent with one another at the $p = 0.5$ level; however, CrA is consistent with both. In the prestellar case, CrA and Ophiuchus are again consistent at $p = 0.5$, while Taurus does not contain enough prestellar cores to be considered. It should be noted that CrA is not well-characterised; its low number statistics (15 starless cores) give it a very broad distribution, and so it is

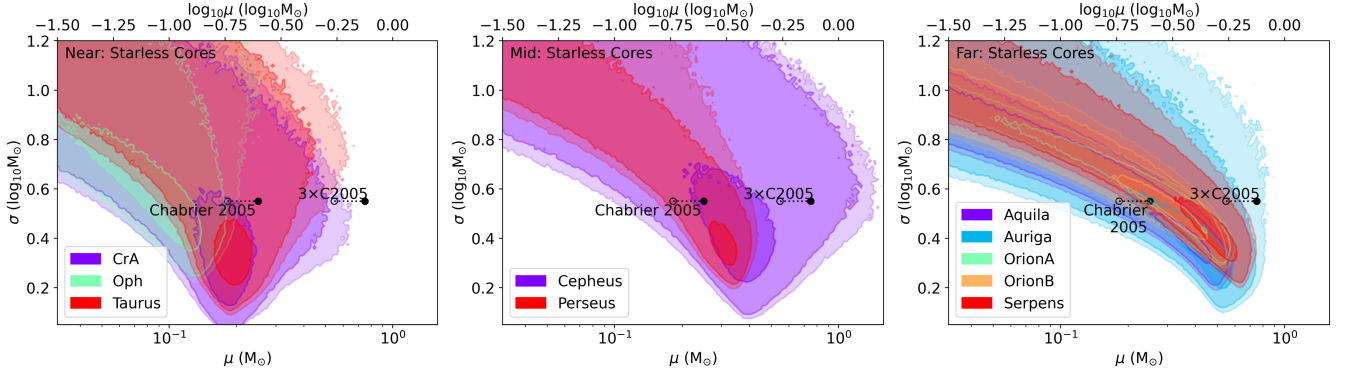


Figure 19. Median p -values for two-sided KS tests between model CMFs and starless CMFs, for matched-mass sampling. Left: near clouds. Centre: mid-distance clouds. Right: Far clouds. Contours show p values of 0.05, 0.1 and 0.5. Filled circles mark $1\times$ and $3\times$ the Chabrier (2005) peak system mass ($0.25 M_{\odot}$). Open circles mark $0.73\times$ these values, accounting for the typical flux loss in our SCUBA-2 observations.

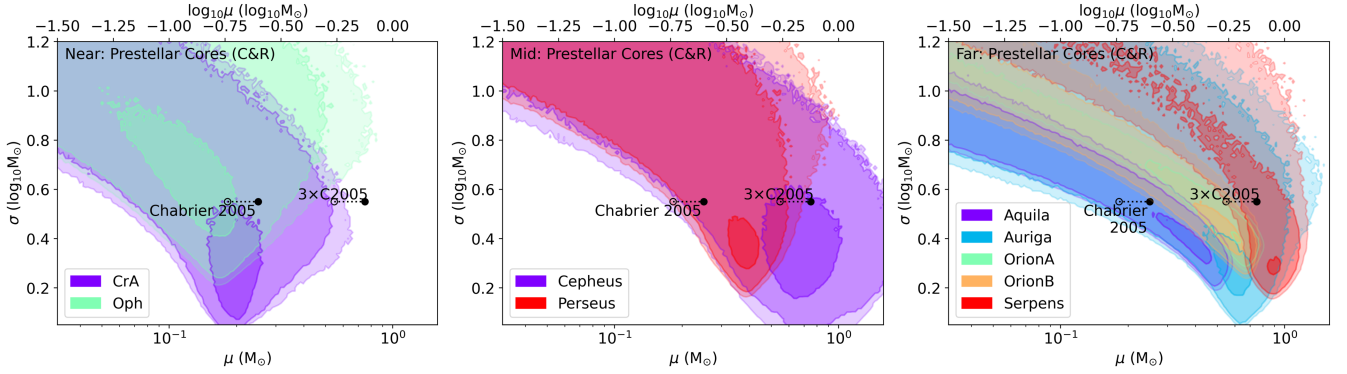


Figure 20. Median p -values for two-sided KS tests between model CMFs and prestellar CMFs, for matched-mass sampling. Left: near clouds. Centre: mid-distance clouds. Right: Far clouds. Filled circles mark $1\times$ and $3\times$ the Chabrier (2005) peak system mass ($0.25 M_{\odot}$). Open circles mark $0.73\times$ these values, accounting for the typical flux loss in our SCUBA-2 observations.

Table 11. The most probable starless and prestellar CMFs for each cloud complex that we consider, as determined from Monte Carlo estimation and two-sided KS tests, using matched-mass sampling. Values of μ and σ are given to the number of decimal places specified in our grid of input models. Median p values, showing the probability that this model and our sample are drawn from the same underlying distribution, are given.

Region	Starless			Prestellar (C & R)		
	μ (M_{\odot})	σ ($\log_{10} M_{\odot}$)	p	μ (M_{\odot})	σ ($\log_{10} M_{\odot}$)	p
Near						
CrA	0.17	0.26	0.77	0.19	0.20	0.80
Ophiuchus	0.11	0.49	0.78	0.15	0.54	0.69
Taurus	0.19	0.29	0.76	–	–	–
Mid						
Cepheus	0.40	0.35	0.75	0.63	0.29	0.74
Perseus	0.31	0.36	0.70	0.39	0.35	0.71
Far						
Aquila	0.37	0.40	0.66	0.37	0.40	0.64
Auriga	0.47	0.32	0.71	0.60	0.25	0.69
Orion A	0.45	0.42	0.51	0.61	0.40	0.53
Orion B	0.38	0.46	0.67	0.58	0.40	0.72
Serpens	0.52	0.40	0.72	0.89	0.29	0.58

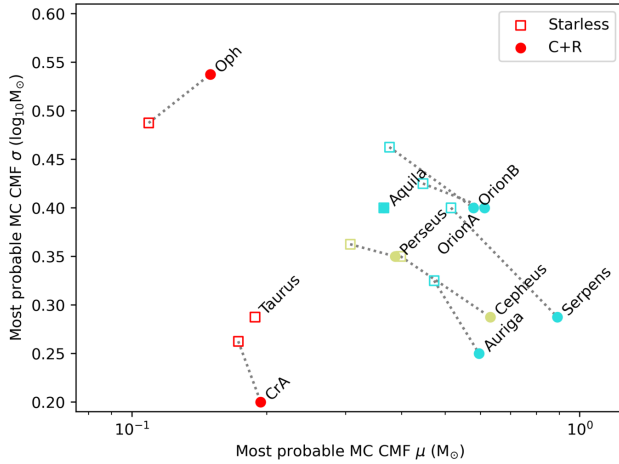


Figure 21. The most probable starless and prestellar CMF properties (as determined from median p -value) measured from matched-mass Monte Carlo modelling for each cloud complex. Open squares show starless core CMFs, closed circles show prestellar CMFs. Cloud complexes are colour-coded by their distance range. The parameter space explored in Figures 18–20 is here restricted to the region of interest.

Table 12. Results of linear regressions of the function $\mu \propto M_{\text{cloud}}^{\gamma}$ to our best-fit LS and most-probable MC CMFs. p_{LR} indicates the probability for a null hypothesis test that $\gamma = 0$ (i.e. no correlation between cloud mass and peak mass of the CMF). Unlike the p value used in previous discussions of the two-sided KS test, a lower p_{LR} indicates better agreement between the data and the model; we consider values $p_{LR} < 0.05$ to be statistically robust.

Case	With Oph		No Oph	
	γ	p_{LR}	γ	p_{LR}
Starless, LS	0.25 ± 0.10	0.03	0.20 ± 0.06	0.02
Starless, MC	0.22 ± 0.08	0.02	0.18 ± 0.05	0.01
Prestellar, LS	0.30 ± 0.10	0.03	0.23 ± 0.08	0.04
Prestellar, MC	0.21 ± 0.11	0.09	0.15 ± 0.09	0.14

consistent with both Taurus and Ophiuchus. However, Taurus and Ophiuchus appear to have different low-mass behaviours. Specifically, there is a lack of low-mass cores in Taurus, and a significant excess in Ophiuchus, despite the two clouds having a similar maximum core mass. Taurus is generally noted as a region of relatively dispersed star formation (e.g. Marsh et al. 2016), while Ophiuchus is considered to be relatively clustered (e.g. Friesen et al. 2009).

Mid-distance clouds: Cepheus and Perseus have quite similar starless core distributions, despite their different morphologies. There is a somewhat higher fraction of bound cores in Perseus than in Cepheus. The starless core CMFs are consistent at the $p = 0.5$ level, while the prestellar CMFs are consistent at the $p = 0.1$ level. However, the CMFs of Cepheus, which only contains 22 starless cores compared to 98 in Perseus, are not very well-constrained.

Far clouds: In the far clouds, the starless CMFs are quite consistent with one another, while the prestellar CMFs show more distinct variation. Auriga (44 starless cores) is less well-constrained than the other far-distance clouds, and so is consistent with all of the other far-distance cloud complexes. Orion A and Orion B agree well with each other in both the starless and prestellar cases (consistent at $p > 0.5$), as might be expected as they are physically associated with one another. However, Orion, Serpens and Aquila do not agree well with one another. In the prestellar case, Orion and Aquila agree at

$p = 0.1$, as do Orion and Serpens. However, Aquila and Serpens do not agree with one another at the $p = 0.05$ level in the prestellar case, and are only consistent at the $p = 0.1$ level in the starless case, despite the fact that Aquila is sometimes considered to be a subset of the Serpens Molecular Cloud (e.g., Pillai et al. 2020).

7 DISCUSSION OF CORE MASS FUNCTIONS

7.1 Comparison with the stellar IMF

Chabrier (2005) characterized the low-mass part of the system IMF with a log-normal distribution with peak mass $\mu_{\text{Chabrier}} = 0.25 M_{\odot}$, and width $\sigma_{\text{Chabrier}} = 0.55 \log_{10} M_{\odot}$.

The far-distance prestellar CMF which we measure, which is marginally consistent with the near- and mid- prestellar CMFs, has $\mu = 0.60 \pm 0.05 M_{\odot}$ and $\sigma = 0.37 \pm 0.02 \log_{10} M_{\odot}$ (best-fit LS), and $\mu = 0.58 M_{\odot}$ and $\sigma = 0.39 \log_{10} M_{\odot}$ (most probable MC). The LS and MC estimates are thus consistent with one another.

We estimate a typical mass recovery fraction in our observations of 73%, which would imply a corrected $\mu \approx 0.8 M_{\odot}$. This value suggests a prestellar CMF which peaks at $\sim 3\times$ the peak stellar system mass, and which is ~ 0.17 dex narrower. If we have correctly characterised the prestellar CMF, this implies a core-to-star star formation efficiency of $\approx 33\%$. This is very similar to that found by Könyves et al. (2010) in *Herschel* observations of the Aquila molecular cloud.

7.1.1 Sampling of the high-mass CMF

Our sample does not contain a sufficient number of high-mass cores to capture the power-law behaviour associated with the high-mass end of the IMF (Salpeter 1955). We can model the CMF adequately using only a log-normal, with the exception of two very massive sources in Orion A. The Chabrier (2005) IMF breaks to a power-law behaviour at $1 M_{\odot}$, while we can fit our CMFs with log-normal distributions up to masses $> 10 M_{\odot}$.

7.1.2 Sampling of the low-mass CMF

It is important to note that we may not be sampling the low-mass end of the CMF well enough to characterise it fully, particularly in the more distant clouds. It is possible to both broaden a CMF and lower its characteristic mass by adding more low-mass cores. Moreover, the MC plots above show a degeneracy between μ and σ ; many of the CMFs that we find could plausibly be drawn from distributions with a lower μ and broader σ than those of the highest-probability distribution. However, in both the near- and the mid-distance cases, the peak of the CMF is significantly above the mass completeness limit, and so should be well-characterised (see Figure 17). Additionally, the values of μ and σ determined for the CMFs of the mid-distance clouds are quite consistent with those determined for the far-distance clouds (see Figure E16). These results suggest that incomplete sampling of the low-mass end of the CMF cannot fully explain the differing widths of the IMF and the CMF which we measure.

7.1.3 Effect of unresolved cores

We note that we have a number of unresolved cores in our sample, for which we have assumed a uniform BEC angular radius of $4.8''$ (see Section 4.2.5). These cores could potentially create a bias in our results. However, we consider this effect to be minimal, because we see a fairly even spread in masses of unresolved cores (see Figure 17).

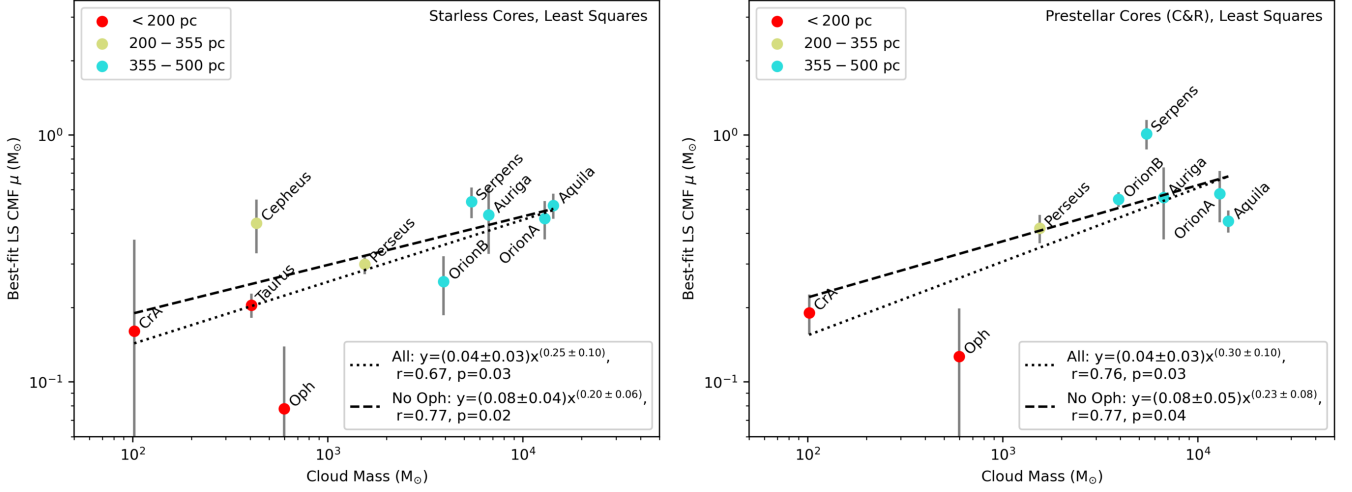


Figure 22. The peak mass of the starless (left) and prestellar (right) CMFs as a function of cloud complex mass, determined using least-squares fitting. Dotted line shows the power-law model producing the best fit to all data points; dashed line shows the power-law model producing the best fit to the data points with Ophiuchus, which has a notably low peak mass, excluded. Data points are colour-coded by their distance range.

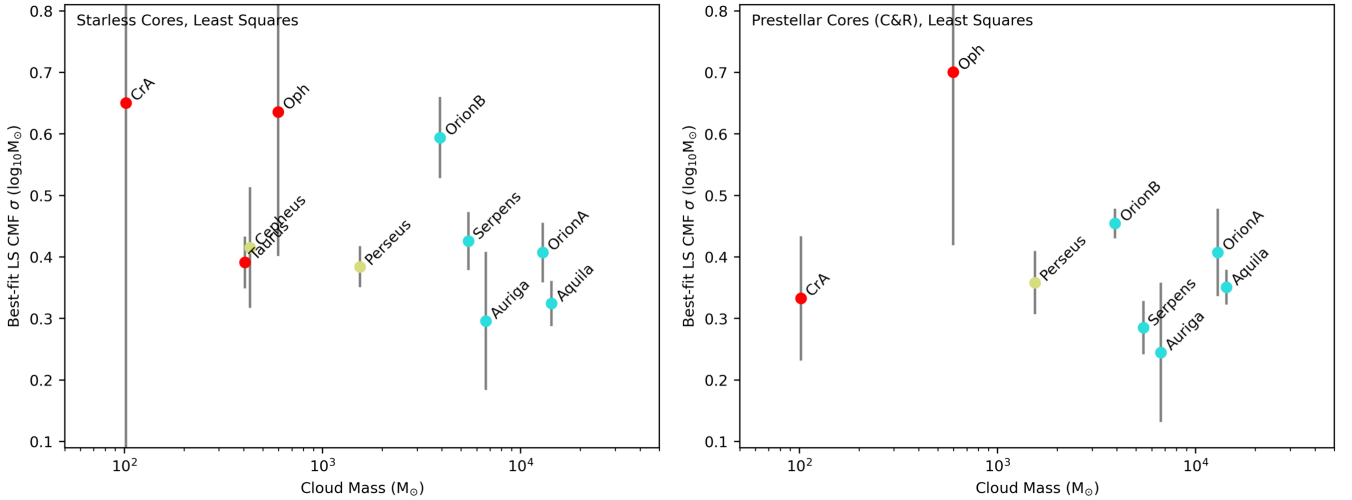


Figure 23. The width of the starless (left) and prestellar (right) CMFs as a function of cloud complex mass, determined using least-squares fitting. Data points are colour-coded by their distance range.

As a result, these cores are unlikely to be creating any significant biases in the CMFs. Moreover, only 4% of the starless in our sample are unresolved, so their impact on the statistics of our sample is likely small. The large majority of the unresolved cores are in the more distant clouds: there is only one unresolved core in the middle distance range, and the mid-distance Perseus and Cepheus prestellar CMFs are broadly consistent with those for the more distant clouds. These points again suggest that the effect of unresolved cores on our CMFs is minimal.

7.2 CMF variation between clouds

As discussed in Section 6.2.4 above, the CMFs of the nearby clouds appear to be different both from one another other and from the mid- and far-distance clouds. The mid- and far-distance clouds all appear to

be consistent with having similar underlying starless core CMFs. The mid- and far-distance clouds all have statistically similar prestellar core CMFs, but different most probable prestellar core CMFs.

The fact that the CMFs of the associated Orion A and Orion B clouds are extremely consistent with each other in both the starless and prestellar cases suggests that the variation between cloud CMFs which we see may not be only statistical scatter. There may be genuine physical differences in how the clouds fragment into cores, or how the cores in these clouds acquire further mass.

One such physical difference could be the timescale on which cores evolve. If higher-mass prestellar cores last longer than their low-mass counterparts (Offner et al. 2014), then the observed CMF would be weighted towards the longer-lived, more massive cores. The median mass of the CMF would also be biased upwards in more massive regions (and downwards in lower-mass regions). As

the far-distance clouds contain more massive sources than the near- or mid-distance regions in Figure 18, evolutionary timescales might go some way towards reconciling the differences in CMF and median mass between clouds.

7.2.1 Nearby clouds

The nearby clouds appear to occupy a different part of the CMF parameter space than do the mid-distance and far clouds (cf. Figure 21), likely with a lower peak mass. The nearby clouds also lack high-mass cores (cf. Figure 15). These differences suggest that, depending on the relative number of low-mass and high-mass clouds, low-mass clouds may be able to contribute a significant number of lower-mass stars to the IMF, potentially both broadening the IMF and lowering its peak mass. However, it should be noted that we are less sensitive to lower-mass sources in the more distant clouds, and so these more distant clouds are likely also contributing significant numbers of lower-mass stars to the IMF.

The nearby clouds, as well as lacking high-mass cores, also appear to have more significant intrinsic difference from one another than do the more distant clouds, although this finding is largely based on the well-known significant differences between the Ophiuchus and Taurus molecular clouds.

The Ophiuchus molecular cloud in particular appears to occupy a different part of the log-normal CMF parameter space than the rest of the clouds that we consider here, with a broader CMF and a lower peak mass (Figure 21). The cloud has a significant excess of low-mass cores (Figure 15) and small core radii (Figure 16). However, its maximum core mass and size are consistent with those of other clouds.

If the excess of low-mass cores in Ophiuchus is physical, fragmentation is proceeding differently in Ophiuchus than in the other clouds, and particularly the other nearby clouds. Alternatively, or additionally, the combination of being both nearby and undergoing clustered star formation may make the detection of low-mass cores easier in Ophiuchus than elsewhere, as small, low-mass cores are more likely to be positioned against a background of cloud material, and so be easier to detect than comparable cores in a region of more dispersed star formation.

Previous work has shown that Class I and II disc masses in Ophiuchus are low compared to those in other clouds. Williams et al. (2019) found that disc masses in Class II sources in Ophiuchus are on average lower-mass than those in Lupus, despite Lupus being older and disc masses being expected to decrease with age. Tobin et al. (2020) found that Class I and II disc masses in Ophiuchus are significantly lower than those in Orion, Taurus and Perseus. They consider whether this difference is due to mis-classification of disc types in Ophiuchus due to heavy foreground extinction, or to the Class I disc population in Ophiuchus being systematically older than that in Orion. However, they also consider the possibility that disc masses in Ophiuchus are genuinely physically lower than those in Orion (and other regions) due to differences in their initial formation conditions. Our finding that core masses are also systematically lower in Ophiuchus than elsewhere supports this latter interpretation, suggesting that fragmentation into cores may be proceeding differently in Ophiuchus than in other nearby clouds.

We note that Cazzoletti et al. (2019) similarly found low disc masses in CrA compared to the Chamaeleon and Lupus clouds. Although the CMF of CrA is not very well-constrained, we note that it has the second lowest peak mass of the clouds in our sample, after Ophiuchus. If CrA and Ophiuchus both have both a low average core mass and a low disc mass compared to other clouds at similar dis-

tance, we speculate that the lower core and disc masses in Ophiuchus may be due to differences in fragmentation (or in subsequent mass acquisition) between cores in regions of clustered and dispersed star formation.

We note that while Taurus has been thought to have an unusual IMF (e.g. Luhman et al. 2003; Goodwin et al. 2004; Luhman et al. 2009; Kraus et al. 2017), recent reanalysis with *Gaia* data has shown that its IMF is consistent with those of other nearby star-forming regions (Luhman 2018). Despite this, we find that like the other nearby clouds, the CMF of Taurus occupies a different part of parameter space than do the more distant clouds.

The differences both between the nearby low-mass clouds and the rest of our sample, and between the nearby clouds themselves, suggests that none can confidently be treated as a ‘typical’ star-forming region. The variation in behaviour that we see between the CMFs in these clouds may provide insights into the effects of environment and clustering on the properties of cores. The proximity of these clouds allows the effect of environment on core properties to be investigated with good mass sensitivity and physical resolution.

7.3 Effects of sample size

As discussed in Section 1, if a subsample is drawn from the stellar IMF, then the maximum stellar mass increases with the size of the sample (Weidner & Kroupa 2005; Weidner et al. 2010; Elmegreen 2006). Only the largest samples (above around $10^4 M_\odot$) sample the full mass distribution and include the highest-mass stars. The sum of the masses of the starless cores in our sample is $917 M_\odot$, and so for a core-to-star mass efficiency of $\sim 1/3$, we would expect them to form a total stellar mass of $\sim 300 M_\odot$, two orders of magnitude too low to sample the full IMF.

As discussed in Section 5.4, we find that the maximum starless core mass in a cloud complex scales with cloud complex mass as $M_{max} \propto M_{cloud}^{0.58 \pm 0.13}$. This relationship is consistent with the 2/3-power scaling between the mass of the most massive star in stellar cluster and the cluster mass found by Bonnell et al. (2004). Hence, there may be a relatively constant core-to-star mass conversion efficiency in the clouds in our sample. Furthermore, we need a significantly larger sample size in order to capture the behaviour of the CMF fully – if indeed there is a single CMF representative of all star-forming regions.

To characterise the high-mass CMF accurately, we require observations of higher-mass (and perforce more distant) star-forming regions. Orion A and Aquila, the most massive cloud complexes that we consider, while undergoing some high-mass star formation, are not high-mass star-forming regions in the sense that more distant massive hub-filament systems are (e.g., Motte et al. 2018). The form of the high-mass CMF in high-mass star-forming regions is being investigated by the ALMA-IMF Survey (Motte et al. 2022). The ALMA-IMF Survey has characterised the high-mass power-law slope of the CMF in some massive star-forming clouds (Pouteau et al. 2022), but their mass completeness limits (e.g. $0.8 M_\odot$ in W43) are too high to capture the behaviour of the low-mass CMF in these more distant regions.

In our sample, we see that the distributions of masses in nearby clouds appear to be more disparate than those in more distant, typically more massive, star-forming regions. This difference begs the question of whether larger and higher-mass clouds are genuinely more similar to one another than are smaller clouds, perhaps due to being less influenced by their local environment, or whether by virtue of their size they encompass the range of behaviours seen in low-mass clouds at different locations within them.

To answer these questions, and understand fully the form of the CMF, and how it varies between star-forming regions, we require the ability to detect, and ideally resolve, low-mass cores in more distant high-mass star-forming regions. To do so in sufficient numbers to sample the full CMF adequately will require the sensitivities and mapping speeds which are planned for next-generation submillimetre instrumentation such as 50-m-class single-dish telescopes or focal plane array interferometers.

8 CONCLUSIONS

In this paper we have presented a catalogue of dense cores identified in SCUBA-2 observations of nearby molecular clouds made as part of the JCMT Gould Belt Survey. We identified 2257 dense cores using the *getsources* algorithm, along with further selection criteria. Of these, 2004 were resolved. We identified 1323 sources as starless cores, 845 sources as protostellar cores, 70 sources as being heated (24- μ m-bright) starless cores, and 19 sources as being potential extragalactic contaminants. Of the starless cores, 456 were identified as robust prestellar cores, 484 as candidate prestellar cores, and 383 as unbound cores using the critical Bonnor–Ebert criterion.

Our key conclusions are as follows:

(i) On average, 59% of the detected cores are starless, and 41% are protostellar. 71% of the starless cores are prestellar cores (candidate or robust). This breakdown suggests that the lifetime for prestellar cores is ~ 0.5 Myr, similar to that of Class 0/I embedded YSOs (Evans et al. 2009).

(ii) We see statistically significant differences in starless and prestellar core fractions between cloud complexes. We found that both Serpens and Orion B have an excess of starless and prestellar cores, while Taurus and the Pipe Nebula have a deficit. The trend is for higher-mass regions to have a higher fraction of starless (or prestellar) cores compared to protostars, suggesting a longer average lifetime for prestellar cores in higher-mass clouds.

(iii) There is a weak correlation between median starless core mass and cloud complex mass. We find that maximum starless core mass scales with cloud complex mass, such that $M_{max} \propto M_{cloud}^{0.58 \pm 0.13}$. This relationship is consistent with the 2/3 scaling between maximum stellar mass in a cluster and cluster mass (Bonnell et al. 2004).

(iv) We found that the CMFs of clouds in our survey can be characterised using log-normal distributions. However, we do not sample a sufficiently large number of sources to recover the expected high-mass Salpeter-like power-law slope.

(v) We found that the CMFs of cores in our sample are not consistent with all being drawn from the same underlying distribution, both when considered as a function of distance and when considered by cloud complex. The mid-distance (200–355 pc) and far-distance (355–500 pc) CMFs are somewhat consistent with one another. However, the near-distance (< 200 pc) starless CMFs are only marginally consistent with the mid- and far-distance starless CMFs, while the near-distance prestellar CMF is marginally consistent with the mid-distance prestellar CMF, and almost entirely inconsistent with the far-distance prestellar CMF. Starless core CMFs for individual cloud complexes are typically consistent with one another in the mid- and far-distance ranges, but the prestellar core CMFs show greater variation. The CMFs of the near-distance clouds are less consistent both with one another and with the mid- and far-distance clouds.

(vi) The prestellar CMF of the far-distance clouds has a peak mass (μ) of approximately $3\times$ the Chabrier (2005) log-normal peak for the system IMF, consistent with the value seen in Aquila by the *Herschel*

Gould Belt Survey (Könyves et al. 2015). This implies a prestellar core-to-star efficiency of $\sim 1/3$. The prestellar and starless CMFs of both the mid- and far-distance clouds have a width systematically ≈ 0.15 dex lower than that of the Chabrier (2005) log-normal IMF.

(vii) We found that the CMF of the nearby Ophiuchus molecular cloud is noticeably different from those of the other clouds in our survey, being wide, and with a significantly lower peak mass. This difference appears to be due to an excess of low-mass cores in this cloud, but may be the result of a selection effect due to the proximity of the cloud and its clustered star formation. However, Ophiuchus also has unusually low disc masses, compared to region of non-clustered star formation at similar distances. This difference suggests that the excess of low-mass sources in Ophiuchus may be indicative of differences in fragmentation between regions of clustered and dispersed star formation.

We present this catalogue as a resource to the community, noting that many further analyses of the cores are possible, such as full energetic balance analyses for those cores for which appropriate spectroscopic and polarimetric data is available, and comparison with *Herschel* Gould Belt Survey catalogues, and other catalogues of Gould Belt sources.

Our analysis shows that the CMFs of the Gould Belt clouds are not consistent with being drawn from a single underlying CMF. The Gould Belt clouds do not contain a number – or mass – of cores sufficient to sample the full range of core masses needed to create the stellar IMF. However, they do give us insight into the variation of properties of low-mass cores within and between molecular clouds. Thus, the ability to detect cores with masses down to the brown dwarf mass limit in more distant, higher-mass, clouds, is required to understand the form, and the variability, of the Core Mass Function.

ACKNOWLEDGEMENTS

We thank Alexander Men’shchikov for helpful discussions on the *getsources* algorithm, and Jason Kirk for providing a complete *Herschel* column density map of the Taurus Molecular Cloud.

K.P. is a Royal Society University Research Fellow, supported by grant number URF/R1\211322, and at various points in the long history of this project has been supported by the Ministry of Science and Technology of Taiwan under grant number 106-2119-M-007-021-MY3, and by the Science and Technology Facilities Council (STFC) of the United Kingdom under grant numbers ST/K002023/1 and ST/M000877/1. J.D.F., H.K. and D.J. acknowledge support from separate NSERC Discovery Grants. H.K., J.D.F., S.N., and R.K. acknowledge support from the National Research Council of Canada co-op program at the Herzberg Astronomy and Astrophysics Research Centre which enabled S.N. and R.K. to participate in this research. D.W.T. acknowledges support from the UK STFC on grant number ST/R000786/1. The Dunlap Institute is funded through an endowment established by the David Dunlap family and the University of Toronto.

The James Clerk Maxwell Telescope (JCMT) is operated by the East Asian Observatory on behalf of the National Astronomical Observatory of Japan; the Academia Sinica Institute of Astronomy and Astrophysics; the Korea Astronomy and Space Science Institute; the National Astronomical Research Institute of Thailand; the Center for Astronomical Mega-Science (as well as the National Key R&D Program of China with grant no. 2017YFA0402700). Additional funding support is provided by the STFC of the UK and participating universities and organizations in the UK, Canada and Ireland. Additional funds for the construction of SCUBA-2 were provided by the Canada

Foundation for Innovation. The JCMT has historically been operated by the Joint Astronomy Centre on behalf of the STFC of the UK, the NRC of Canada and the Netherlands Organisation for Scientific Research.

This research has made use of:

- The Canadian Advanced Network For Astronomy Research (CAN-FAR; Gaudet et al. 2010), operated in partnership by the Canadian Astronomy Data Centre and The Digital Research Alliance of Canada with support from the National Research Council (NRC) of Canada, the Canadian Space Agency, CANARIE and the Canadian Foundation for Innovation.
- Starlink software (Currie et al. 2014), currently supported by the East Asian Observatory.
- Astropy (<http://www.astropy.org>), a community-developed core Python package and an ecosystem of tools and resources for astronomy (Astropy Collaboration et al. 2013, 2018, 2022).
- The NASA/IPAC Extragalactic Database (NED), which is funded by the National Aeronautics and Space Administration and operated by the California Institute of Technology.
- The SIMBAD database, operated at CDS, Strasbourg, France.
- Data products from the Wide-field Infrared Survey Explorer, which is a joint project of the University of California, Los Angeles, and the Jet Propulsion Laboratory/California Institute of Technology, funded by the National Aeronautics and Space Administration (NASA).
- Data from the Herschel Gould Belt Survey (HGBS) project (<http://gouldbelt-herschel.cea.fr>). The HGBS is a Herschel Key Programme jointly carried out by SPIRE Specialist Astronomy Group 3 (SAG 3), scientists of several institutes in the PACS Consortium (CEA Saclay, INAF-IFSI Rome and INAF-Arcetri, KU Leuven, MPIA Heidelberg), and scientists of the Herschel Science Center (HSC).
- NASA’s Astrophysics Data System.

The authors wish to recognize and acknowledge the very significant cultural role and reverence that the summit of Maunakea has always had within the indigenous Hawaiian community. We are most fortunate to have the opportunity to conduct observations from this mountain.

DATA AVAILABILITY

The raw data used to create the maps used in this paper are available in the JCMT data archive hosted by the Canadian Astronomy Data Centre (CADC) <https://www.cadc-ccda.hia-ihc.nrc-cnrc.gc.ca/en/>, under project codes MJLSG31 (Orion A), MJLSG32 (Ophiuchus), MJLSG33 (Aquila and Serpens), MJLSG34 (Lupus), MJLSG35 (Corona Australis), MJLSG36 (IC 5146), MJLSG37 (Auriga and Taurus), MJLSG38 (Perseus), MJLSG39 (Pipe Nebula), MJLSG40 (Cepheus) and MJLSG41 (Orion B). The maps of all regions used in this paper are available for public download through Kirk et al. (2018), or directly at the DOI <https://doi.org/10.11570/18.0005>. The JCMT Gould Belt Survey Core Catalogue is available at [DOI TBC], along with the output of the *getsources* algorithm without our selection criteria applied. The code used to create model Bonnor–Ebert spheres for completeness testing is available at <https://github.com/KatePattle/bonnor-ebert-sphere>.

REFERENCES

- Alves J. F., Lada C. J., Lada E. A., 2001, *Nature*, **409**, 159
 André P., et al., 2010, *A&A*, **518**, L102

- André P., Di Francesco J., Ward-Thompson D., Inutsuka S. I., Pudritz R. E., Pineda J. E., 2014, in Beuther H., Klessen R. S., Dullemond C. P., Henning T., eds, *Protostars and Planets VI*. p. 27 ([arXiv:1312.6232](https://arxiv.org/abs/1312.6232)), doi:10.2458/azu_uapress_9780816531240-ch002
- Arzoumanian D., et al., 2011, *A&A*, **529**, L6
- Arzoumanian D., et al., 2019, *A&A*, **621**, A42
- Astropy Collaboration et al., 2013, *A&A*, **558**, A33
- Astropy Collaboration et al., 2018, *AJ*, **156**, 123
- Astropy Collaboration et al., 2022, *apj*, **935**, 167
- Beckwith S. V. W., Sargent A. I., Chini R. S., Guesten R., 1990, *AJ*, **99**, 924
- Belloche A., et al., 2011, *A&A*, **527**, A145
- Benedettini M., et al., 2018, *A&A*, **619**, A52
- Benson P. J., Myers P. C., 1989, *ApJS*, **71**, 89
- Bertoldi F., McKee C. F., 1992, *ApJ*, **395**, 140
- Bohlin R. C., Savage B. D., Drake J. F., 1978, *ApJ*, **224**, 132
- Bonnell I. A., Vine S. G., Bate M. R., 2004, *MNRAS*, **349**, 735
- Bonnell I. A., Smith R. J., Clark P. C., Bate M. R., 2011, *MNRAS*, **410**, 2339
- Bonnor W. B., 1956, *MNRAS*, **116**, 351
- Bresnahan D., et al., 2018, *A&A*, **615**, A125
- Broekhoven-Fiene H., et al., 2014, *ApJ*, **786**, 37
- Broekhoven-Fiene H., et al., 2018, *ApJ*, **852**, 73
- Buckle J. V., et al., 2009, *MNRAS*, **399**, 1026
- Buckle J. V., et al., 2015, *MNRAS*, **449**, 2472
- Cazzoletti P., et al., 2019, *A&A*, **626**, A11
- Chabrier G., 2003, *PASP*, **115**, 763
- Chabrier G., 2005, in Corbelli E., Palla F., Zinnecker H., eds, *Astrophysics and Space Science Library Vol. 327, The Initial Mass Function 50 Years Later*. p. 41 ([arXiv:astro-ph/0409465](https://arxiv.org/abs/astro-ph/0409465)), doi:10.1007/978-1-4020-3407-7_5
- Chapin E. L., Berry D. S., Gibb A. G., Jenness T., Scott D., Tilanus R. P. J., Economou F., Holland W. S., 2013, *MNRAS*, **430**, 2545
- Chen M. C.-Y., et al., 2016, *ApJ*, **826**, 95
- Coudé S., et al., 2016, *MNRAS*, **457**, 2139
- Currie M. J., Berry D. S., Jenness T., Gibb A. G., Bell G. S., Draper P. W., 2014, in Manset N., Forshay P., eds, *Astronomical Society of the Pacific Conference Series Vol. 485, Astronomical Data Analysis Software and Systems XXIII*. p. 391
- Cutri R. M., et al., 2021, *VizieR Online Data Catalog*, **p. II/328**
- Dempsey J. T., et al., 2013, *MNRAS*, **430**, 2534
- Di Francesco J., Evans N. J. I., Caselli P., Myers P. C., Shirley Y., Aikawa Y., Tafalla M., 2007, in Reipurth B., Jewitt D., Keil K., eds, *Protostars and Planets V*. p. 17 ([arXiv:astro-ph/0602379](https://arxiv.org/abs/astro-ph/0602379))
- Di Francesco J., et al., 2020, *ApJ*, **904**, 172
- Dodds P., Greaves J. S., Scholz A., Hatchell J., Holland W. S., JCMT Gould Belt Survey Team 2015, *MNRAS*, **447**, 722
- Drabek E., et al., 2012, *MNRAS*, **426**, 23
- Dunham M. M., et al., 2015, *ApJS*, **220**, 11
- Dzib S. A., Loinard L., Ortiz-León G. N., Rodríguez L. F., Galli P. A. B., 2018, *ApJ*, **867**, 151
- Ebert R., 1955, *Z. Astrophys.*, **37**, 217
- Elmegreen B. G., 2006, *ApJ*, **648**, 572
- Encalada F. J., et al., 2024, *ApJ*, **968**, 101
- Enoch M. L., et al., 2006, *ApJ*, **638**, 293
- Evans II N. J., Rawlings J. M. C., Shirley Y. L., Mundy L. G., 2001, *ApJ*, **557**, 193
- Evans N. J. II., et al., 2007, Technical report, Final Delivery of Data from the c2d Legacy Project: IRAC and MIPS, https://irsa.ipac.caltech.edu/data/SPITZER/C2D/doc/c2d_del_document.ps. Spitzer Science Center, Pasadena, CA, https://irsa.ipac.caltech.edu/data/SPITZER/C2D/doc/c2d_del_document.ps
- Evans N. J. II., et al., 2009, *ApJS*, **181**, 321
- Fiorellino E., et al., 2021, *MNRAS*, **500**, 4257
- Friberg P., Bastien P., Berry D., Savini G., Graves S. F., Pattle K., 2016, in Holland W. S., Zmuidzinas J., eds, *Society of Photo-Optical Instrumentation Engineers (SPIE) Conference Series Vol. 9914, Millimeter, Submillimeter, and Far-Infrared Detectors and Instrumentation for Astronomy VIII*. p. 991403, doi:10.1117/12.2231943
- Friesen R. K., Di Francesco J., Shirley Y. L., Myers P. C., 2009, *ApJ*, **697**, 1457

- Friesen R. K., et al., 2017, *ApJ*, **843**, 63
- Frøberich D., Rowles J., 2010, *MNRAS*, **406**, 1350
- Gaudet S., et al., 2010, in Radziwill N. M., Bridger A., eds, Society of Photo-Optical Instrumentation Engineers (SPIE) Conference Series Vol. 7740, Software and Cyberinfrastructure for Astronomy. p. 77401I, doi:10.1117/12.858026
- Ginsburg A., et al., 2022, *A&A*, **662**, A9
- Goodwin S. P., Whitworth A. P., Ward-Thompson D., 2004, *A&A*, **419**, 543
- Harvey P. M., et al., 2008, *ApJ*, **680**, 495
- Harvey P. M., et al., 2013, *ApJ*, **764**, 133
- Hatchell J., Richer J. S., Fuller G. A., Qualtrough C. J., Ladd E. F., Chandler C. J., 2005, *A&A*, **440**, 151
- Hatchell J., et al., 2012, *ApJ*, **754**, 104
- Hatchell J., et al., 2013, *MNRAS*, **429**, L10
- Herczeg G. J., et al., 2019, *ApJ*, **878**, 111
- Hildebrand R. H., 1983, *QJRAS*, **24**, 267
- Holland W. S., et al., 2013, *MNRAS*, **430**, 2513
- Howard A. D. P., Whitworth A. P., Marsh K. A., Clarke S. D., Griffin M. J., Smith M. W. L., Lomax O. D., 2019, *MNRAS*, **489**, 962
- Howard A. D. P., Whitworth A. P., Griffin M. J., Marsh K. A., Smith M. W. L., 2021, arXiv e-prints, p. arXiv:2104.04007
- Johnstone D., Wilson C. D., Moriarty-Schieven G., Joncas G., Smith G., Gregersen E., Fich M., 2000, *ApJ*, **545**, 327
- Johnstone D., Fich M., Mitchell G. F., Moriarty-Schieven G., 2001, *ApJ*, **559**, 307
- Johnstone D., Boonman A. M. S., van Dishoeck E. F., 2003, *A&A*, **412**, 157
- Johnstone D., Di Francesco J., Kirk H., 2004, *ApJ*, **611**, L45
- Johnstone D., et al., 2017, *ApJ*, **836**, 132
- Juvela M., et al., 2015, *A&A*, **584**, A94
- Kackley R., Scott D., Chapin E., Friberg P., 2010, Society of Photo-Optical Instrumentation Engineers (SPIE) Conference Series, 7740
- Kern N. S., Keown J. A., Tobin J. J., Mead A., Gutermuth R. A., 2016, *AJ*, **151**, 42
- Kerr R., et al., 2019, *ApJ*, **874**, 147
- Kirk H., Johnstone D., Di Francesco J., 2006, *ApJ*, **646**, 1009
- Kirk J. M., et al., 2009, *ApJS*, **185**, 198
- Kirk J. M., et al., 2013, *MNRAS*, **432**, 1424
- Kirk H., et al., 2016a, *ApJ*, **817**, 167
- Kirk H., et al., 2016b, *ApJ*, **821**, 98
- Kirk H., et al., 2017, *ApJ*, **846**, 144
- Kirk H., et al., 2018, *ApJS*, **238**, 8
- Kirk J. M., et al., 2024, *MNRAS*, **532**, 4661
- Könyves V., et al., 2010, *A&A*, **518**, L106
- Könyves V., et al., 2015, *A&A*, **584**, A91
- Könyves V., et al., 2020, *A&A*, **635**, A34
- Kounkel M., et al., 2017, *ApJ*, **834**, 142
- Kraus A. L., Herczeg G. J., Rizzuto A. C., Mann A. W., Slesnick C. L., Carpenter J. M., Hillenbrand L. A., Mamajek E. E., 2017, *ApJ*, **838**, 150
- Kroupa P., 2001, *MNRAS*, **322**, 231
- Lada C. J., Alves J., Lada E. A., 1999, *ApJ*, **512**, 250
- Ladd E. F., Adams F. C., Casey S., Davidson J. A., Fuller G. A., Harper D. A., Myers P. C., Padman R., 1991, *ApJ*, **382**, 555
- Ladjetate B., et al., 2020, *A&A*, **638**, A74
- Lane J., et al., 2016, *ApJ*, **833**, 44
- Leung C. M., 1975, *ApJ*, **199**, 340
- Lombardi M., Bouy H., Alves J., Lada C. J., 2014, *A&A*, **566**, A45
- Luhman K. L., 2018, *AJ*, **156**, 271
- Luhman K. L., Briceño C., Stauffer J. R., Hartmann L., Barrado y Navascués D., Caldwell N., 2003, *ApJ*, **590**, 348
- Luhman K. L., Mamajek E. E., Allen P. R., Cruz K. L., 2009, *ApJ*, **703**, 399
- Mairs S., et al., 2015, *MNRAS*, **454**, 2557
- Mairs S., et al., 2016, *MNRAS*, **461**, 4022
- Marsh K. A., et al., 2016, *MNRAS*, **459**, 342
- Marton G., Tóth L. V., Paladini R., Kun M., Zahorec S., McGehee P., Kiss C., 2016, *MNRAS*, **458**, 3479
- Megeath S. T., et al., 2012, *AJ*, **144**, 192
- Men'shchikov A., André P., Didelon P., Motte F., Hennemann M., Schneider N., 2012, *A&A*, **542**, A81
- Motte F., Andre P., Neri R., 1998, *A&A*, **336**, 150
- Motte F., et al., 2018, *Nature Astronomy*, **2**, 478
- Motte F., et al., 2022, *A&A*, **662**, A8
- Mowat C., et al., 2017, *MNRAS*, **467**, 812
- Myers P. C., Basu S., 2021, *ApJ*, **917**, 35
- Nielbock M., et al., 2012, *A&A*, **547**, A11
- Nony T., et al., 2023, *A&A*, **674**, A75
- Offner S. S. R., Clark P. C., Hennebelle P., Bastian N., Bate M. R., Hopkins P. F., Moraux E., Whitworth A. P., 2014, in Beuther H., Klessen R. S., Dullemond C. P., Henning T., eds, Protostars and Planets VI. p. 53 (arXiv:1312.5326), doi:10.2458/azu_uapress_9780816531240-ch003
- Ortiz-León G. N., et al., 2017a, *ApJ*, **834**, 143
- Ortiz-León G. N., et al., 2017b, *ApJ*, **834**, 141
- Ortiz-León G. N., et al., 2018, *ApJ*, **865**, 73
- Palmeirim P., et al., 2013, *A&A*, **550**, A38
- Parker R. J., Alves de Oliveira C., 2017, *MNRAS*, **468**, 4340
- Pattle K., et al., 2015, *MNRAS*, **450**, 1094
- Pattle K., et al., 2017, *MNRAS*, **464**, 4255
- Pattle K., et al., 2021, *ApJ*, **907**, 88
- Pattle K., et al., 2025, *MNRAS*, **537**, 2127
- Peretto N., et al., 2012, *A&A*, **541**, A63
- Peterson D. E., et al., 2011, *ApJS*, **194**, 43
- Pezzuto S., et al., 2021, *A&A*, **645**, A55
- Pillai T. G. S., et al., 2020, *Nature Astronomy*, **4**, 1195
- Pokhrel R., et al., 2020, *ApJ*, **896**, 60
- Pokhrel R., et al., 2021, *ApJ*, **912**, L19
- Polychroni D., et al., 2013, *ApJ*, **777**, L33
- Pouteau Y., et al., 2022, *A&A*, **664**, A26
- Pouteau Y., et al., 2023, *A&A*, **674**, A76
- Rebull L. M., et al., 2010, *ApJS*, **186**, 259
- Retter B., Hatchell J., Naylor T., 2021, *MNRAS*, **507**, 1904
- Roy A., et al., 2013, *ApJ*, **763**, 55
- Rumble D., et al., 2015, *MNRAS*, **448**, 1551
- Rumble D., et al., 2016, *MNRAS*, **460**, 4150
- Rumble D., Hatchell J., Kirk H., Pattle K., 2021, *MNRAS*, **505**, 2103
- Rygl K. L. J., et al., 2013, *A&A*, **549**, L1
- Sadavoy S. I., et al., 2010, *ApJ*, **710**, 1247
- Sadavoy S. I., et al., 2013, *ApJ*, **767**, 126
- Sadavoy S. I., et al., 2014, *ApJ*, **787**, L18
- Salji C. J., et al., 2015a, *MNRAS*, **449**, 1769
- Salji C. J., et al., 2015b, *MNRAS*, **449**, 1782
- Salpeter E. E., 1955, *ApJ*, **121**, 161
- Schneider N., et al., 2013, *ApJ*, **766**, L17
- Schuller F., et al., 2021, *A&A*, **651**, A36
- Skrutskie M. F., et al., 2006, *AJ*, **131**, 1163
- Stanke T., Smith M. D., Gredel R., Khanzadyan T., 2006, *A&A*, **447**, 609
- Testi L., Sargent A. I., 1998, *ApJ*, **508**, L91
- Tobin J. J., et al., 2020, *ApJ*, **890**, 130
- Ward-Thompson D., Scott P. F., Hills R. E., Andre P., 1994, *MNRAS*, **268**, 276
- Ward-Thompson D., et al., 2007, *PASP*, **119**, 855
- Ward-Thompson D., et al., 2016, *MNRAS*, **463**, 1008
- Ward-Thompson D., et al., 2017, *ApJ*, **842**, 66
- Weidner C., Kroupa P., 2005, *ApJ*, **625**, 754
- Weidner C., Kroupa P., 2006, *MNRAS*, **365**, 1333
- Weidner C., Kroupa P., Bonnell I. A. D., 2010, *MNRAS*, **401**, 275
- Wenger M., et al., 2000, *A&AS*, **143**, 9
- Wilking B. A., Gagné M., Allen L. E., 2008, in Reipurth B., ed., , Vol. 5, Handbook of Star Forming Regions, Volume II. ASP Monograph Publications, p. 351, doi:10.48550/arXiv.0811.0005
- Williams J. P., Cieza L., Hales A., Ansdell M., Ruiz-Rodríguez D., Casassus S., Perez S., Zurlo A., 2019, *ApJ*, **875**, L9
- Zucker C., Speagle J. S., Schlafly E. F., Green G. M., Finkbeiner D. P., Goodman A. A., Alves J., 2019, *ApJ*, **879**, 125
- Zucker C., Speagle J. S., Schlafly E. F., Green G. M., Finkbeiner D. P., Goodman A., Alves J., 2020, *A&A*, **633**, A51

APPENDIX A: JCMT GBS DATA

In this appendix we present the JCMT GBS data that forms the basis of the catalogue in this paper. Table A1 presents the mapping completeness of the survey as a function of Herschel GBS column density. Figures A1–A27 present the 850 μm and 450 μm JCMT GBS data used in this work, available for public download through Kirk et al. (2018), or directly at <https://doi.org/10.11570/18.0005>.

Table A1. JCMT GBS mapping completeness as a function of Herschel-derived column density. The mapping completeness is calculated as the fraction of pixels/area in the Herschel column density map at or above the listed value which is covered by the JCMT GBS map.

Cloud ^a	$N(H_2)^b (\times 10^{21} \text{ cm}^{-3})$														
	5	6	7	8	9	10	12	14	16	18	20	25	30	40	50
Aquila	0.42	0.67	0.84	0.92	0.95	0.97	0.98	0.99	0.99	1.00	1.00	1.00	1.00	1.00	1.00
Auriga	0.41	0.48	0.60	0.69	0.74	0.77	0.82	0.85	0.86	0.87	0.89	0.92	0.92	0.93	0.94
Cepheus	0.90	0.93	0.96	0.99	1.00	1.00	1.00	1.00	1.00	1.00	1.00	1.00	1.00	1.00	1.00
CrA	0.98	0.99	1.00	1.00	1.00	1.00	1.00	1.00	1.00	1.00	1.00	1.00	1.00	1.00	1.00
IC 5146	0.99	0.99	0.99	0.99	0.99	1.00	1.00	1.00	1.00	1.00	1.00	1.00	1.00	-1	-1
Lupus	0.99	1.00	1.00	1.00	1.00	1.00	1.00	1.00	1.00	1.00	1.00	1.00	1.00	1.00	-1
Ophiuchus	0.99	1.00	1.00	1.00	1.00	1.00	1.00	1.00	1.00	1.00	1.00	1.00	1.00	1.00	1.00
Orion A	0.93	0.94	0.95	0.95	0.96	0.96	0.97	0.98	0.99	0.99	1.00	1.00	1.00	1.00	1.00
Orion B	0.90	0.92	0.93	0.94	0.95	0.95	0.96	0.96	0.95	0.95	0.95	0.96	0.97	1.00	1.00
Perseus	1.00	1.00	1.00	1.00	1.00	1.00	1.00	1.00	1.00	1.00	1.00	1.00	1.00	1.00	1.00
Pipe	0.93	0.94	0.96	0.99	1.00	1.00	1.00	1.00	1.00	1.00	1.00	1.00	1.00	-1	-1
Serpens	0.77	0.83	0.87	0.89	0.90	0.92	0.95	0.98	0.99	0.99	1.00	1.00	1.00	1.00	1.00
Taurus	0.89	0.90	0.91	0.92	0.93	0.94	0.96	0.96	0.96	0.95	0.95	0.93	0.93	1.00	-1

a: Most clouds have a one-to-one correspondence between the area on the sky included in the Herschel GBS (HGBS) map and the JCMT GBS map, but there are some exceptions which are noted here, in alphabetical cloud order. Aquila: the HGBS ‘Aquila’ field covers both the JGBS ‘Aquila’ and ‘SerpensMWC297’ fields, so we include both in the calculation. Auriga: we excluded some noisy artefacts from the edge of the HGBS map. Cepheus: This includes the HGBS map ‘cep11228’ matching the JGBS ‘CepheusL1228’ field, and similarly the HGBS map ‘cep11251’ matching the JGBS ‘CepheusL1251’ field. The JGBS ‘CepheusSouth’ map is covered partially in each of the HGBS maps ‘cep1172’ and ‘cep1157’. The HGBS map ‘cep1241’ was not covered by JGBS. Lupus: JGBS only covered part of the HGBS ‘LupI’ map, so only that field is used for comparison. We excluded some noisy artefacts from the edge of the HGBS LupI map. Ophiuchus: The HGBS ‘ophiuchus’ map does not include coverage for the L1712 area within the JGBS ‘OphScoMain’ map (see, e.g., Wilking et al. 2008), and the JGBS maps ‘OphScoN2’, ‘OphScoN3’ and ‘OphScoN6’ are also not included in the HGBS. Orion A: we excluded some noisy artefacts from the edge of the HGBS map. Taurus: we used the Herschel-based column density map derived by J. Kirk (priv. comm.), as this covered all three of our JGBS fields, while the published HGBS map only matched the JGBS ‘TaurusL1495’ map.

b: A value of -1 is used to denote instances when there are no pixels in the Herschel column density map at or above the specified value.

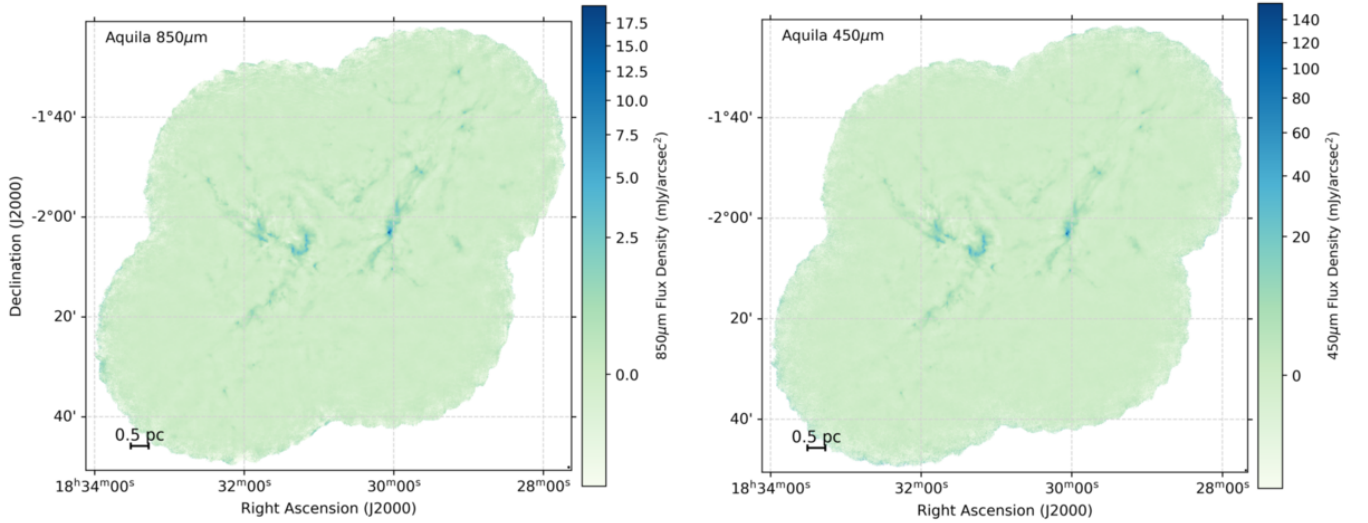


Figure A1. SCUBA-2 850 μm (left) and 450 μm (right) IR3 images of Aquila. Colour scale is cube-root stretched.

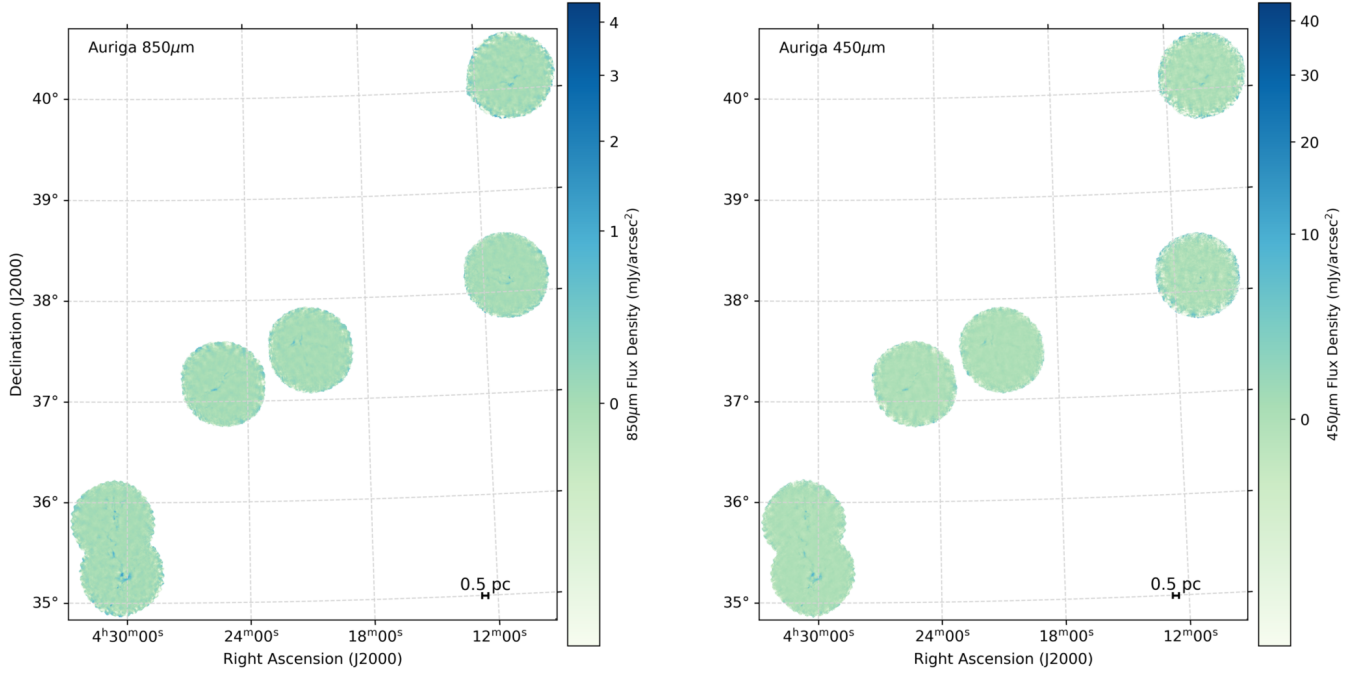


Figure A2. SCUBA-2 850 μm and 450 μm IR3 images of Auriga.

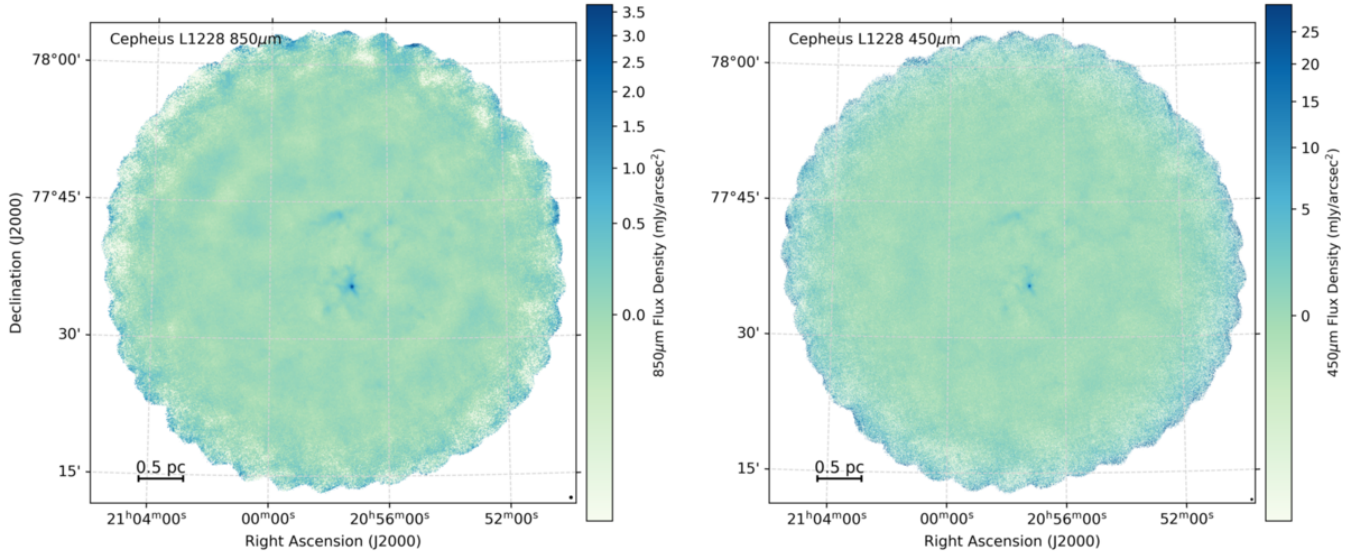


Figure A3. SCUBA-2 850 μm and 450 μm IR3 images of Cepheus L1228.

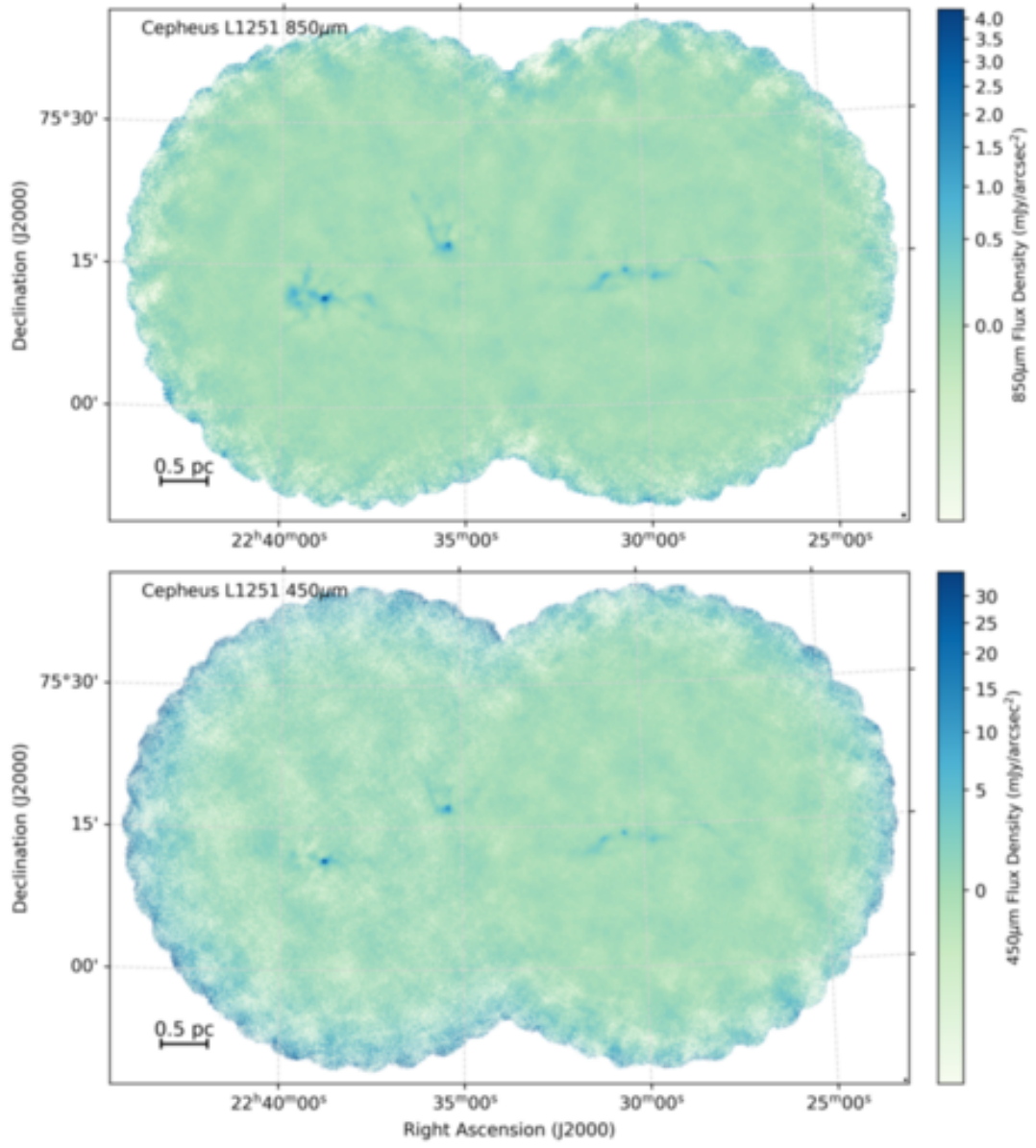


Figure A4. SCUBA-2 850 μm and 450 μm IR3 images of Cepheus L1251.

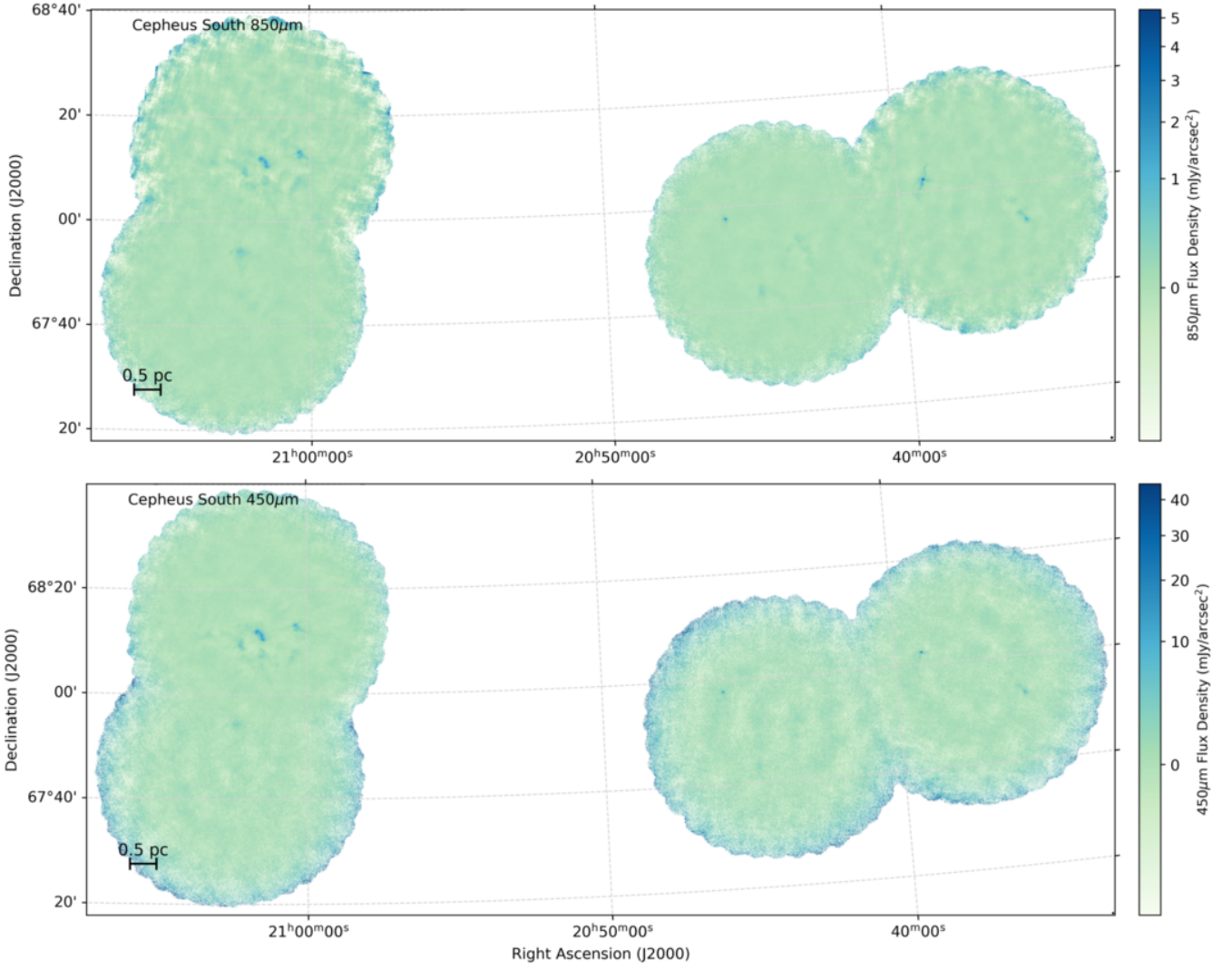


Figure A5. SCUBA-2 850 μm and 450 μm IR3 images of Cepheus South.

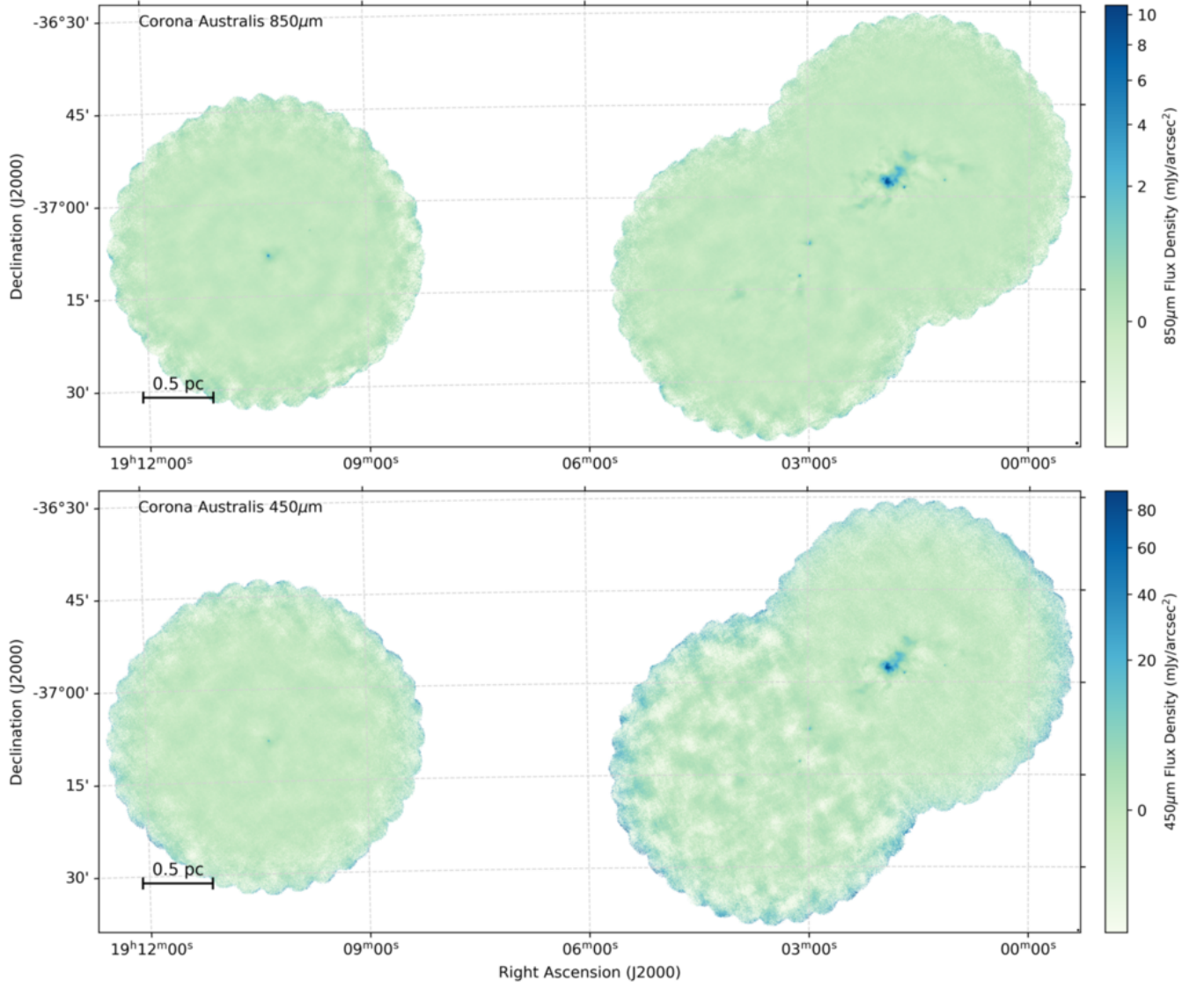


Figure A6. SCUBA-2 850 μ m and 450 μ m IR3 images of Corona Australis.

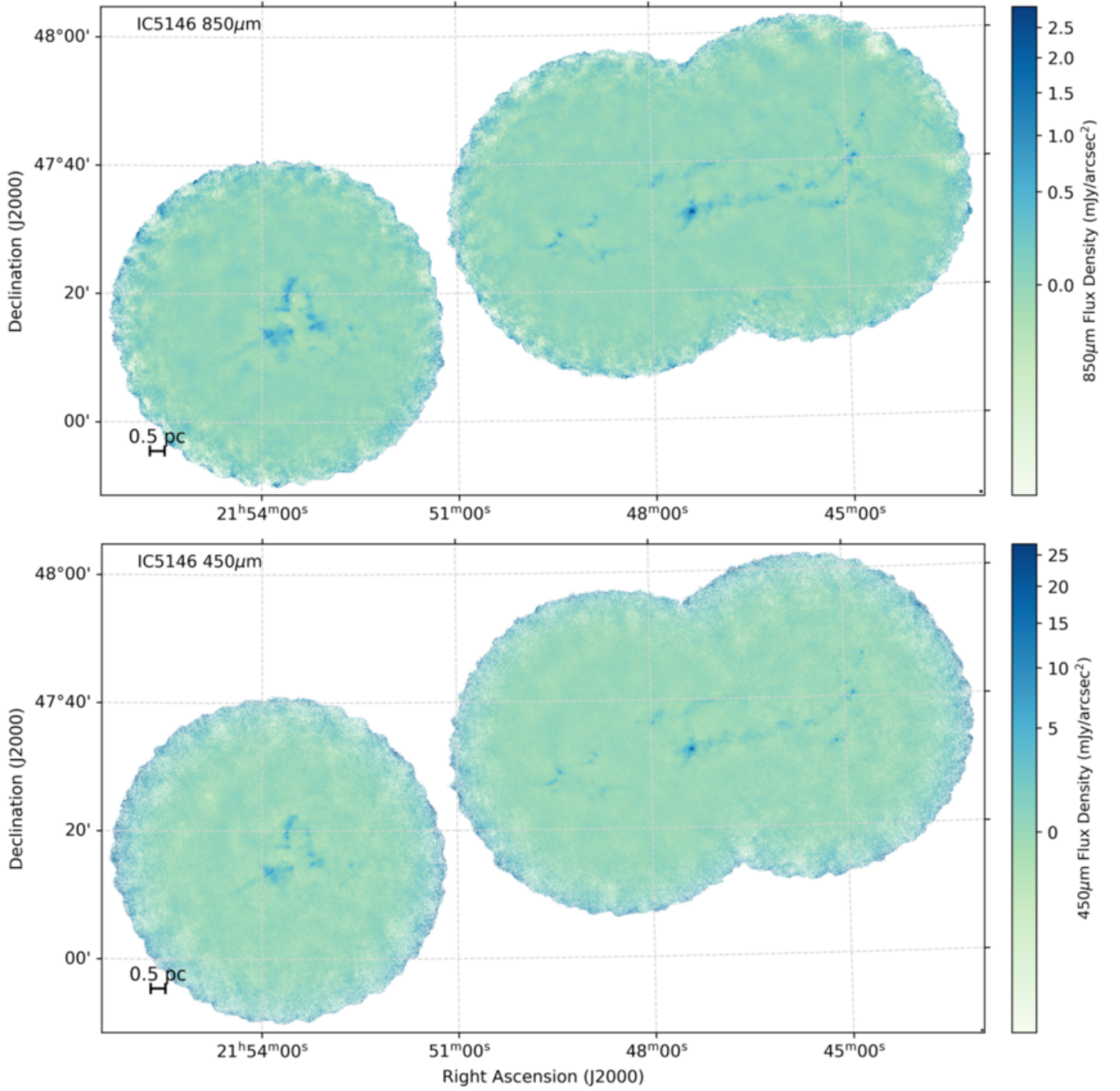


Figure A7. SCUBA-2 850 μm and 450 μm IR3 images of IC 5146.

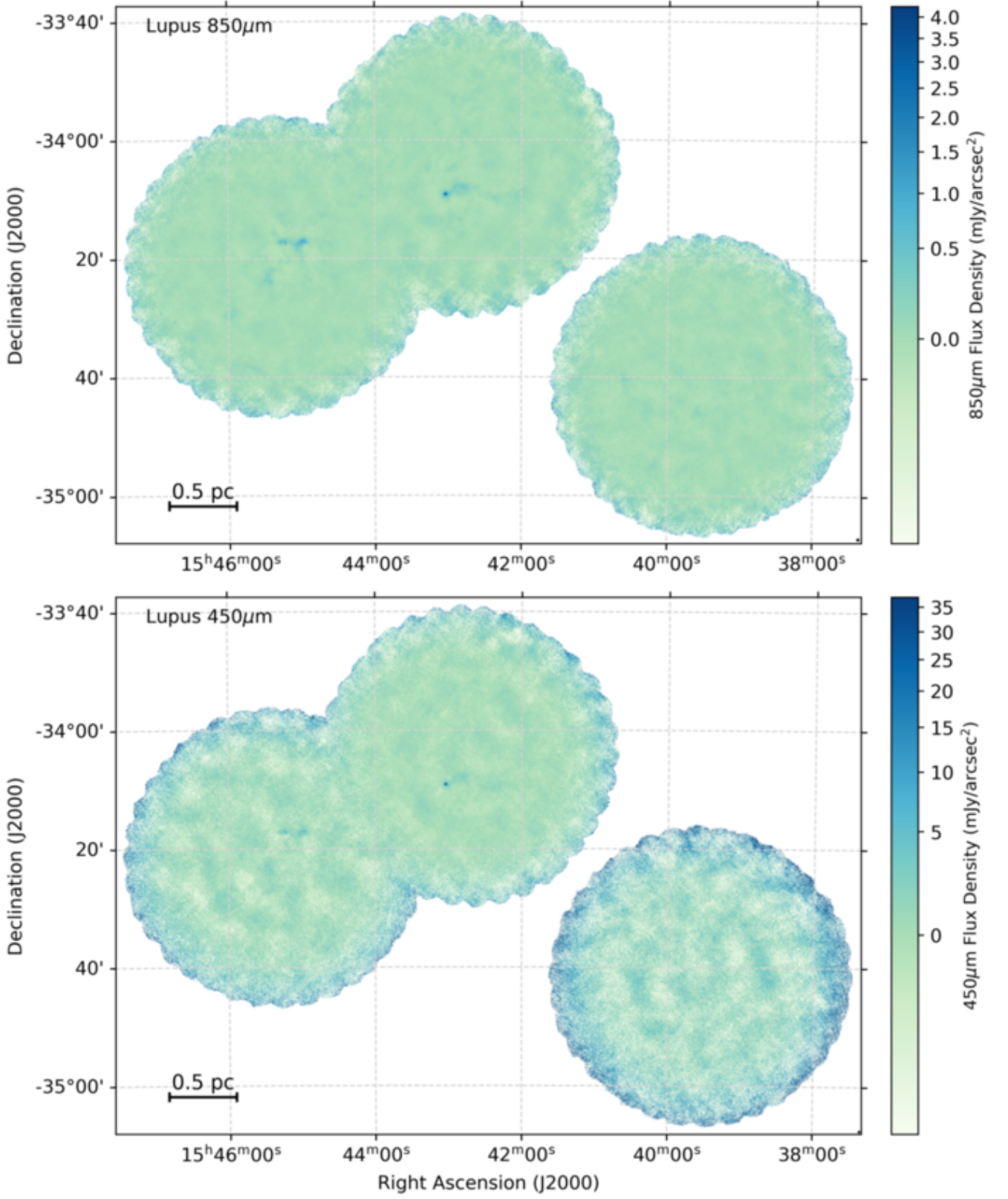


Figure A8. SCUBA-2 850 μ m and 450 μ m IR3 images of Lupus.

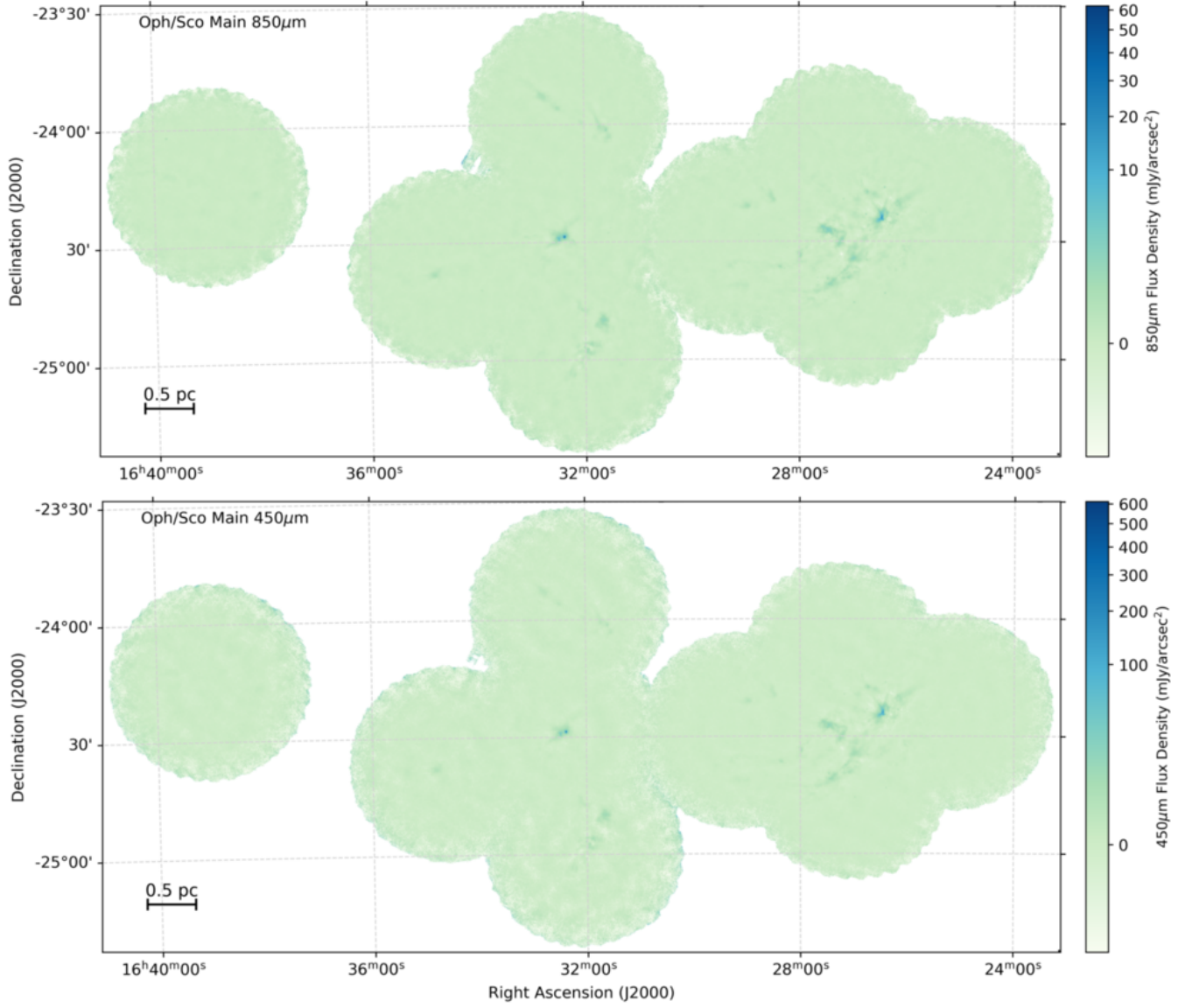


Figure A9. SCUBA-2 850 μm and 450 μm IR3 images of Ophiuchus L1688 (right) and L1689, L1709 and L1712 (left). Colour map is fourth-root scaled.

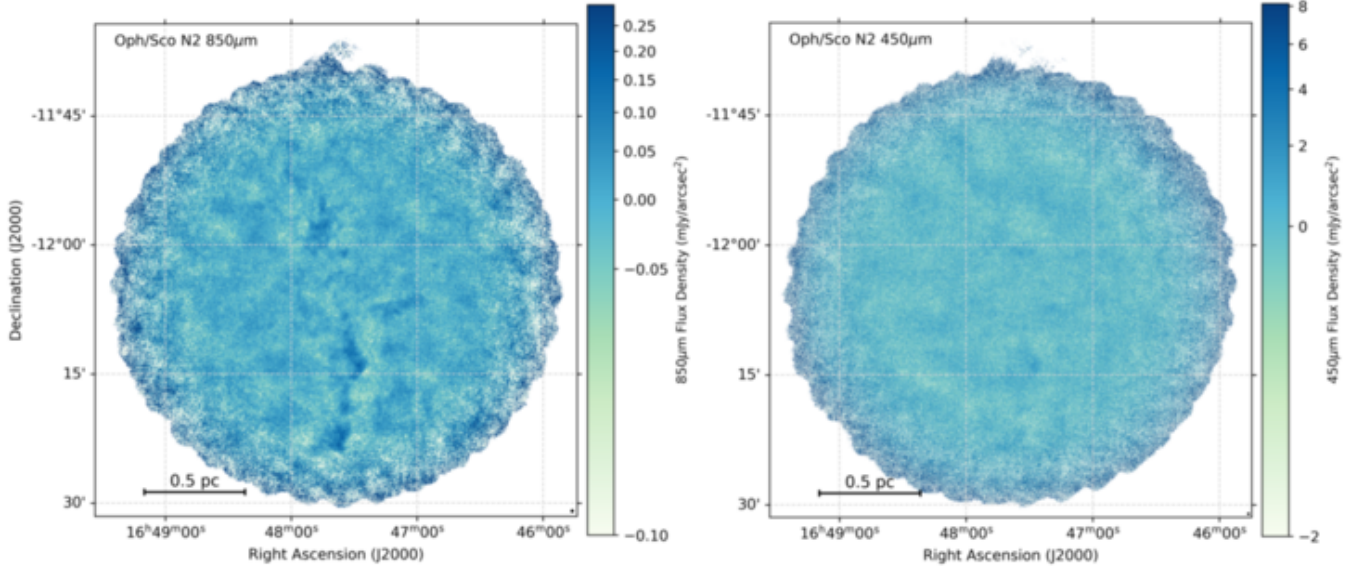


Figure A10. SCUBA-2 850 μm and 450 μm IR3 images of Oph/Sco N2.

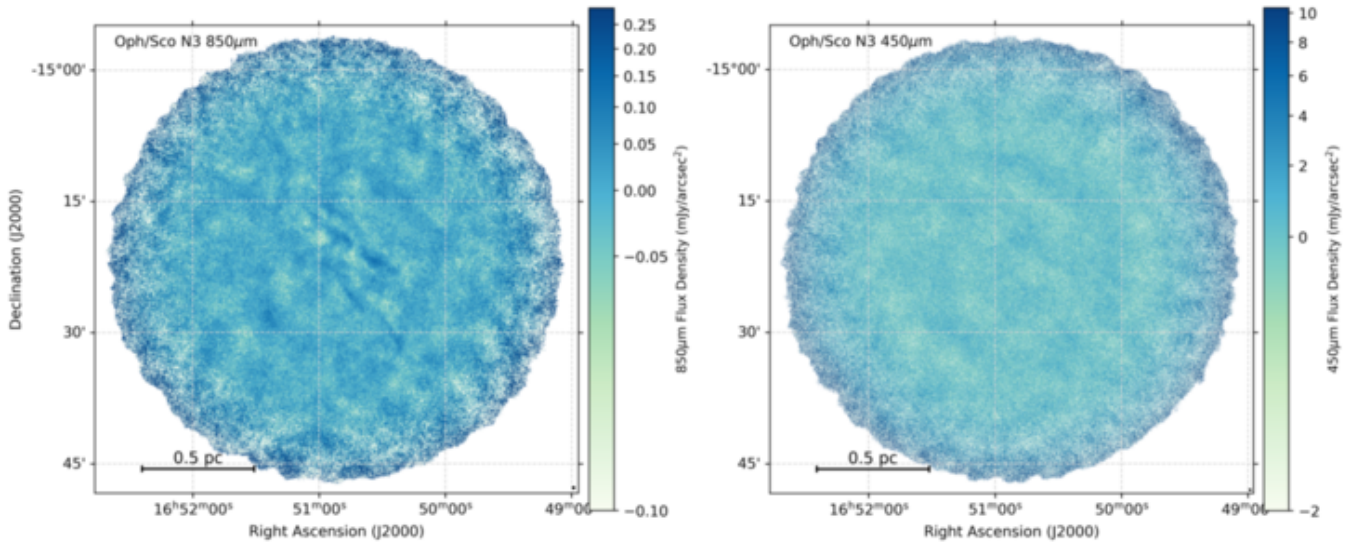


Figure A11. SCUBA-2 850 μm and 450 μm IR3 images of Oph/Sco N3.

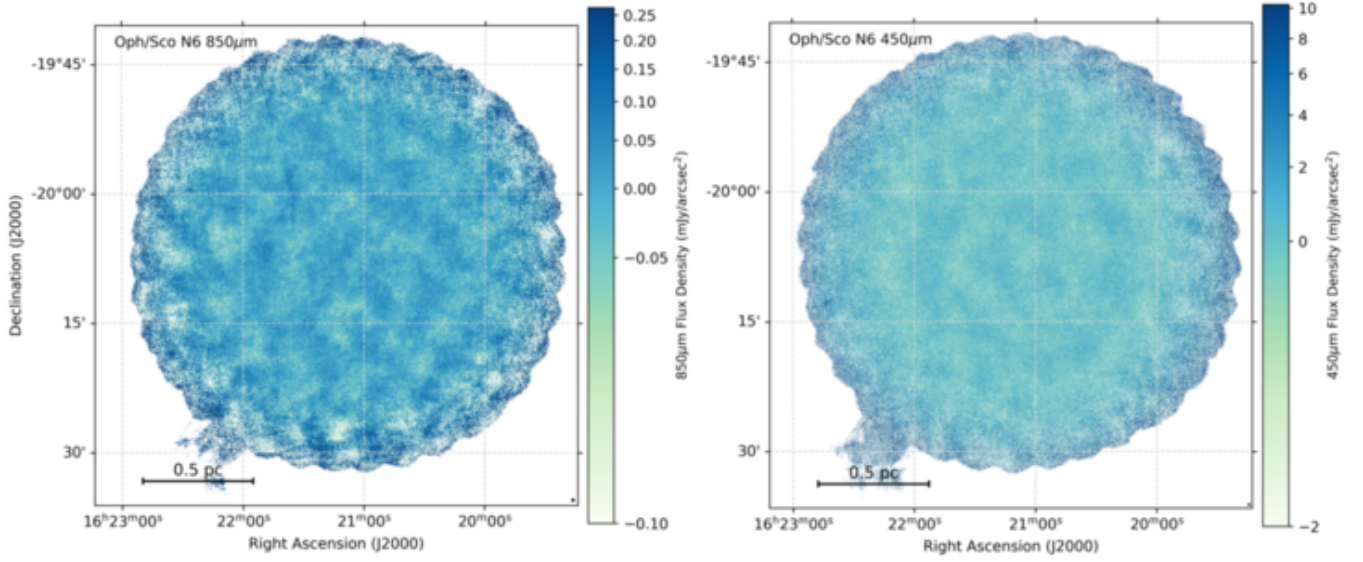


Figure A12. SCUBA-2 850 μm and 450 μm IR3 images of Oph/Sco N6.

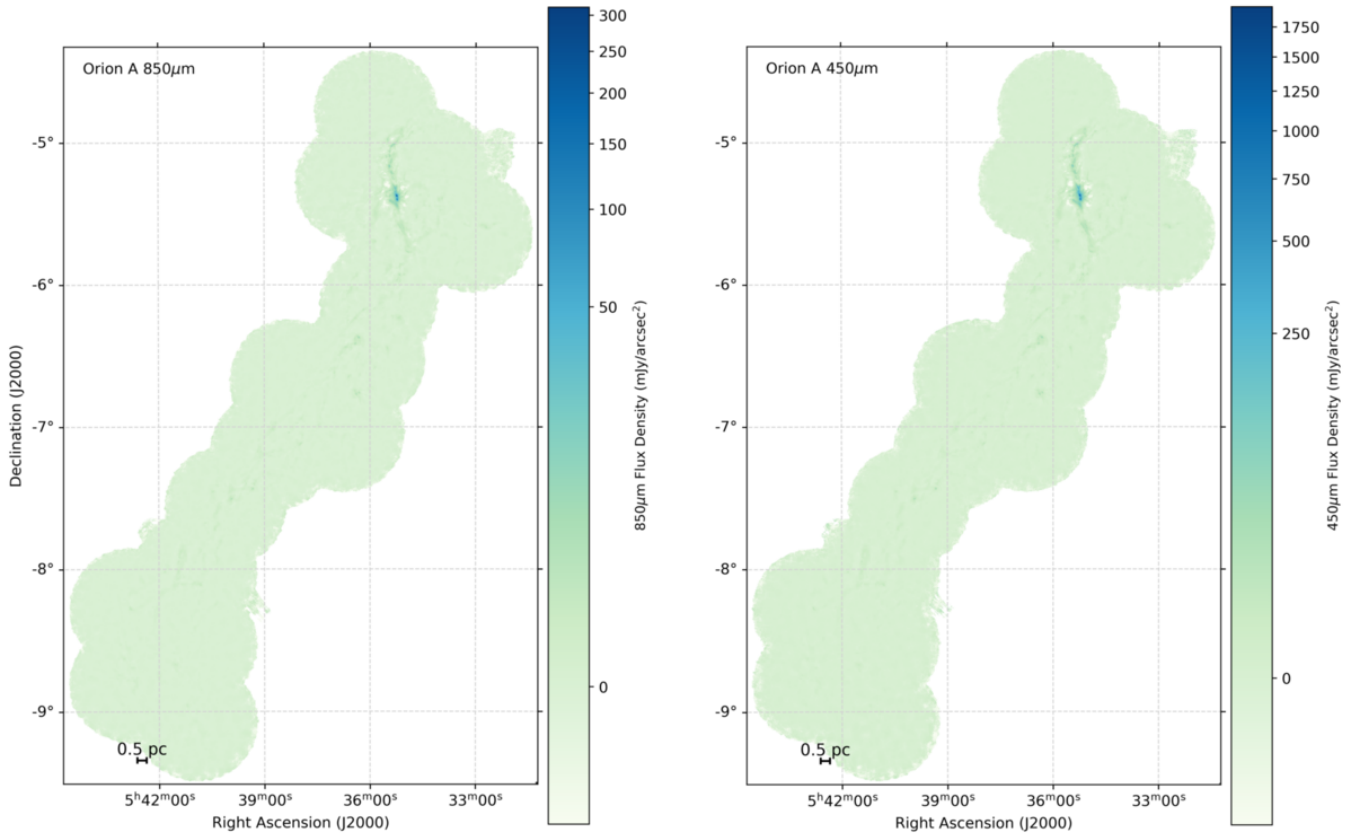


Figure A13. SCUBA-2 850 μm and 450 μm IR3 images of Orion A. Colour map is fourth-root scaled.

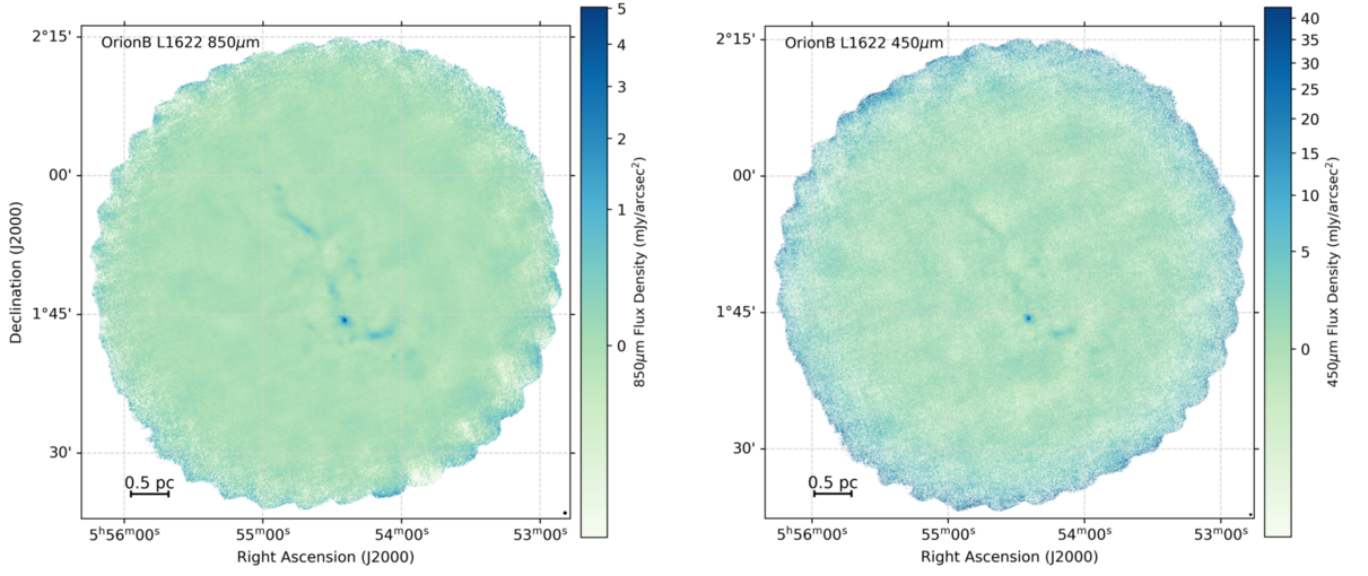


Figure A14. SCUBA-2 850 μm and 450 μm IR3 images of Orion B L1622.

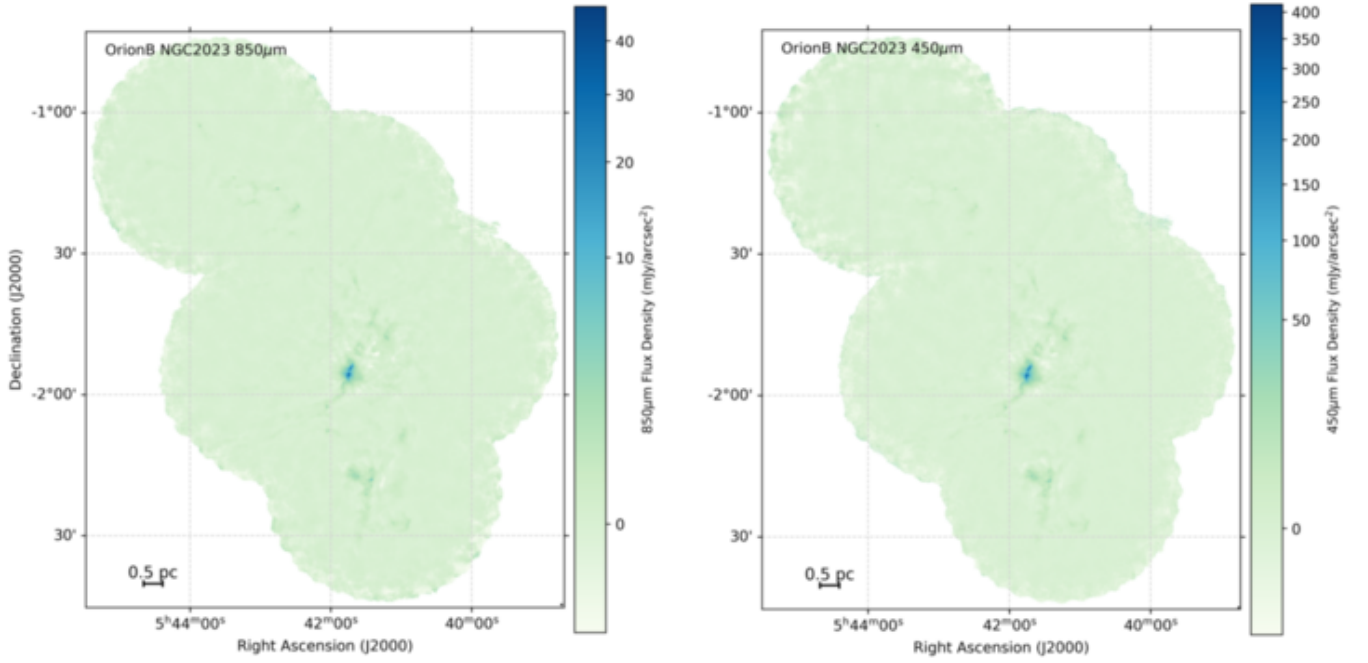


Figure A15. SCUBA-2 850 μm and 450 μm IR3 images of Orion B NGC2023.

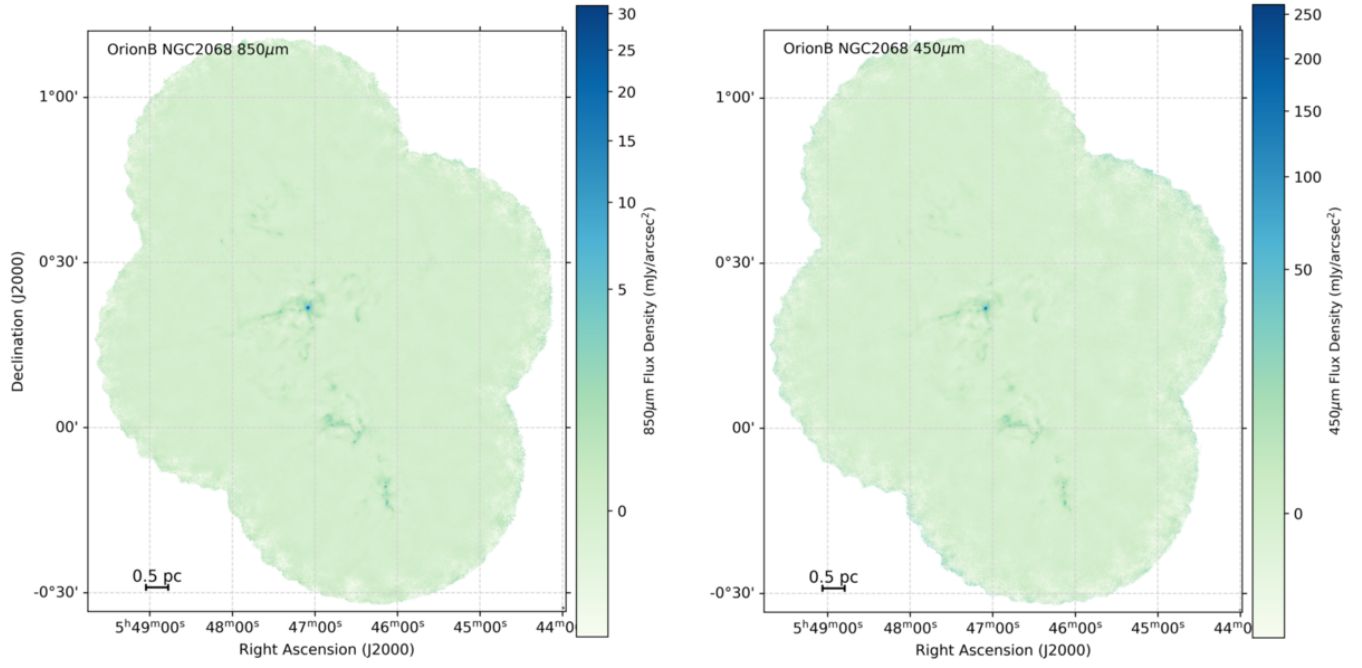


Figure A16. SCUBA-2 850 μ m and 450 μ m IR3 images of Orion B NGC2068.

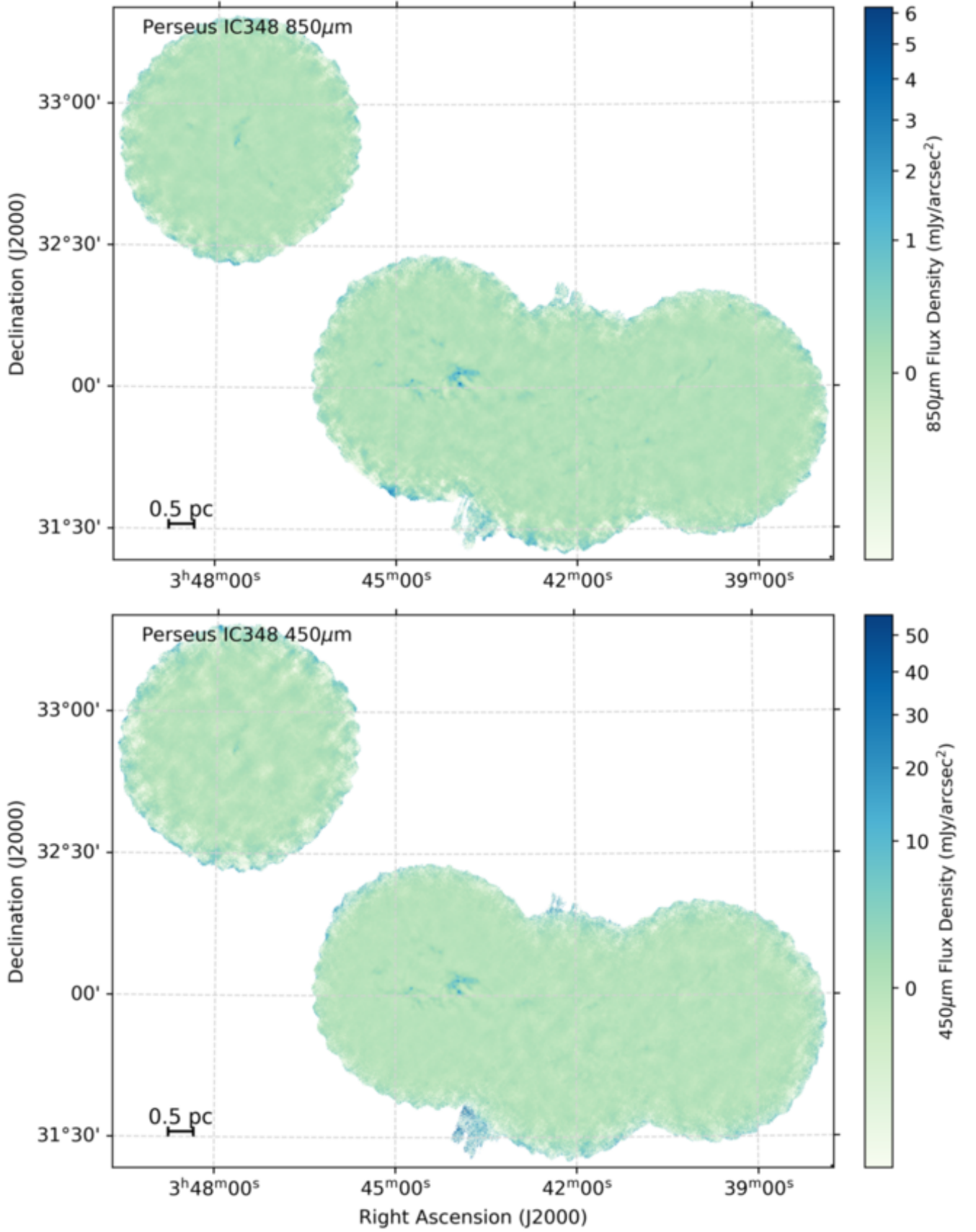


Figure A17. SCUBA-2 850 μm and 450 μm IR3 images of Perseus IC348.

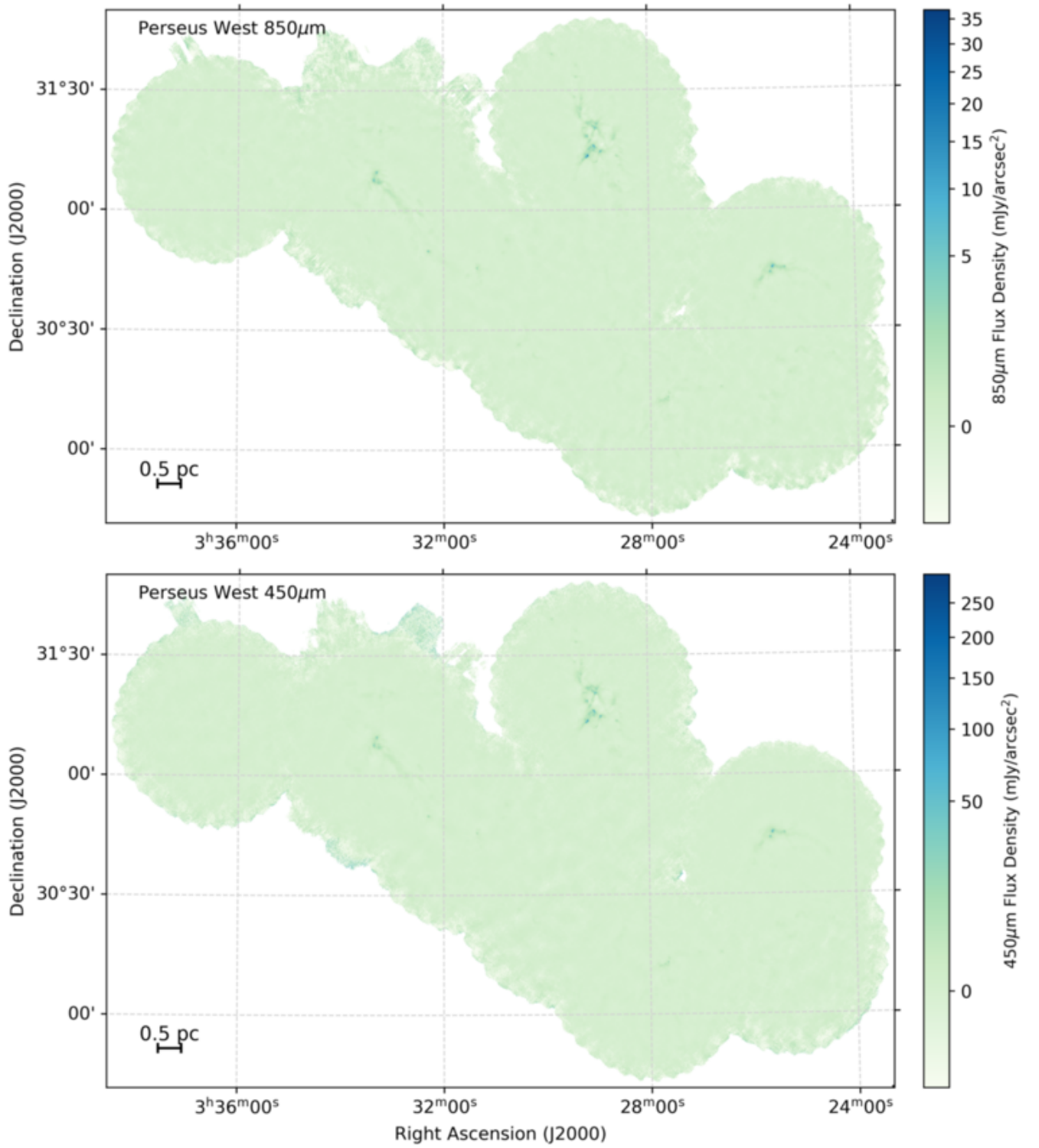
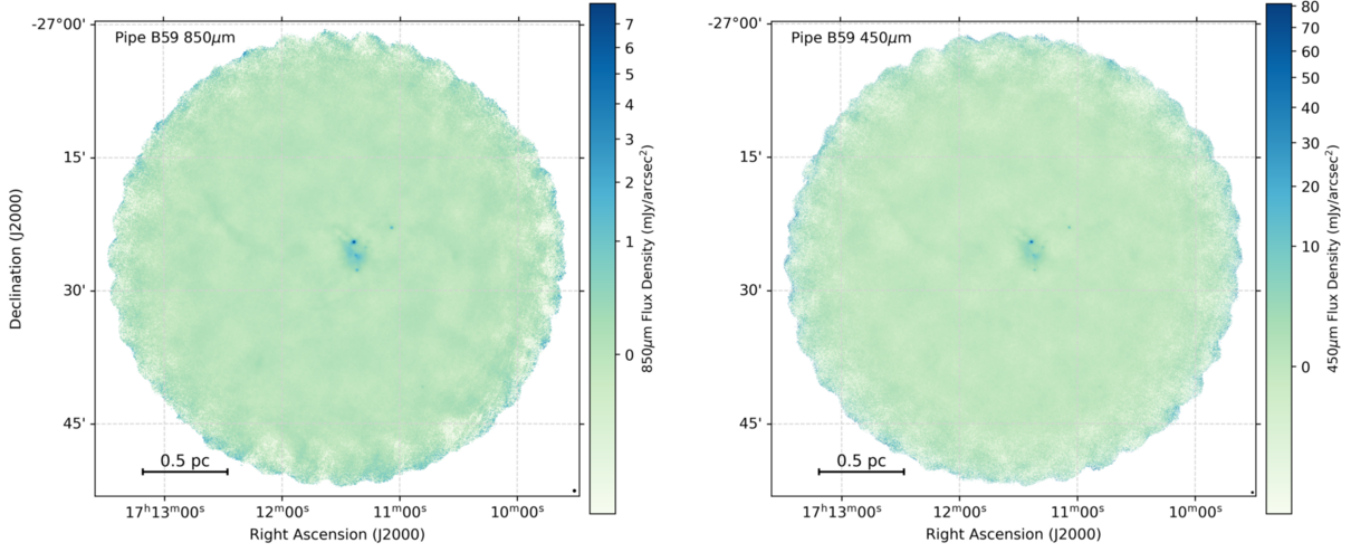
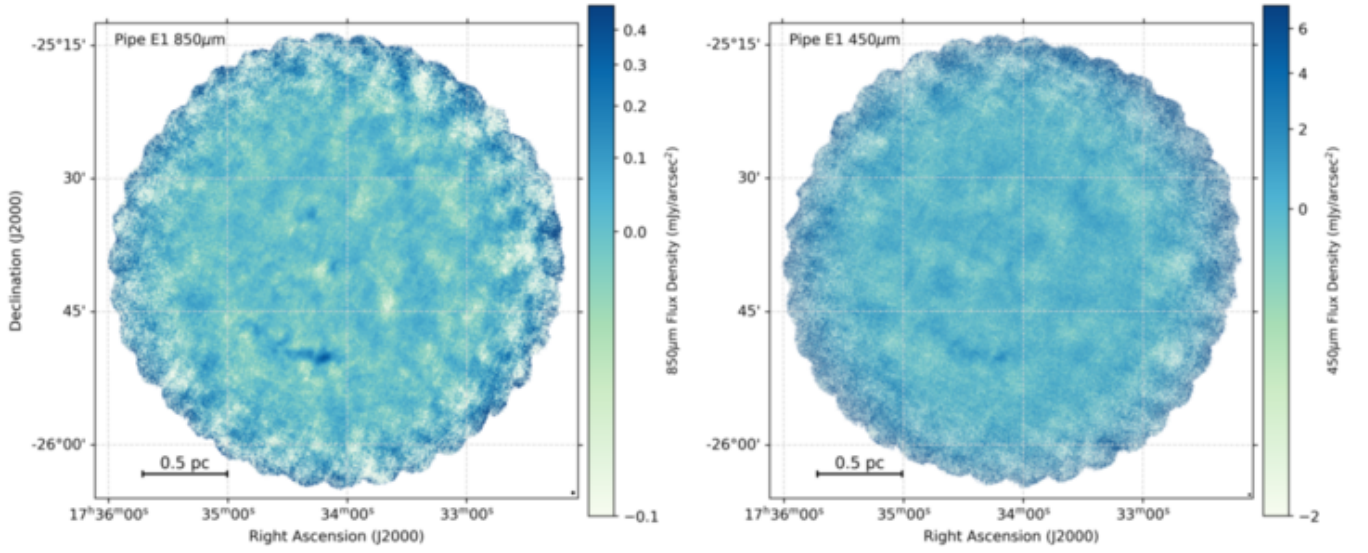


Figure A18. SCUBA-2 850 μm IR4 image of Perseus West.

Figure A19. SCUBA-2 850 μm and 450 μm IR3 images of Pipe B59.Figure A20. SCUBA-2 850 μm and 450 μm IR3 images of Pipe E1.

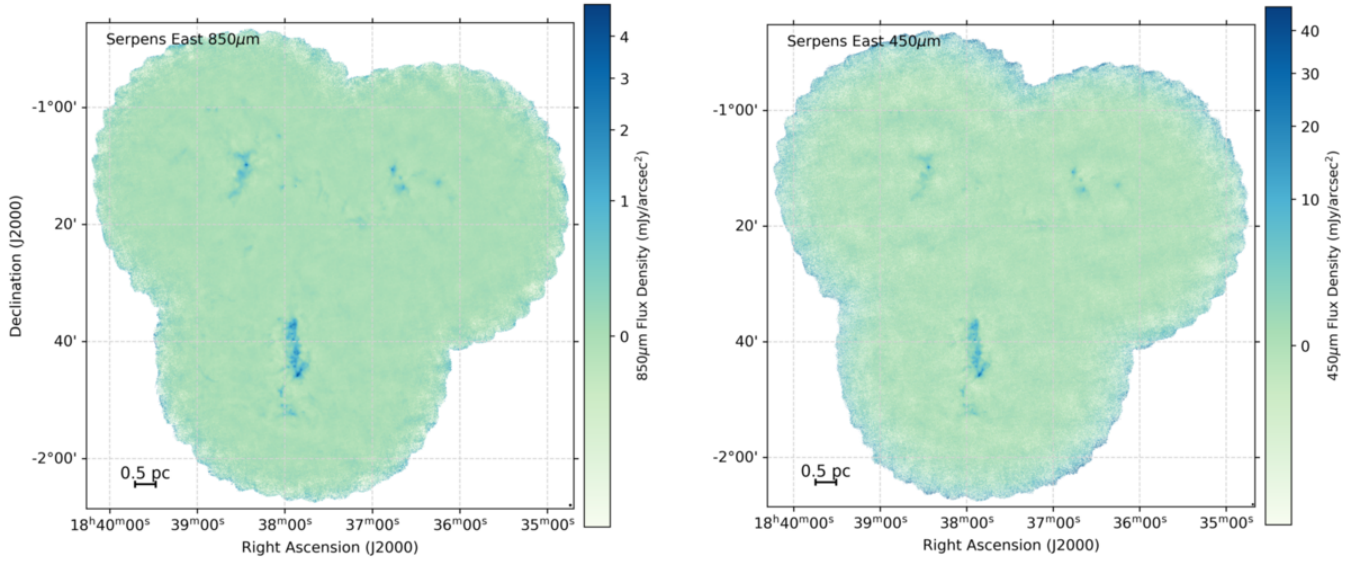


Figure A21. SCUBA-2 850 μm and 450 μm IR3 images of Serpens East.

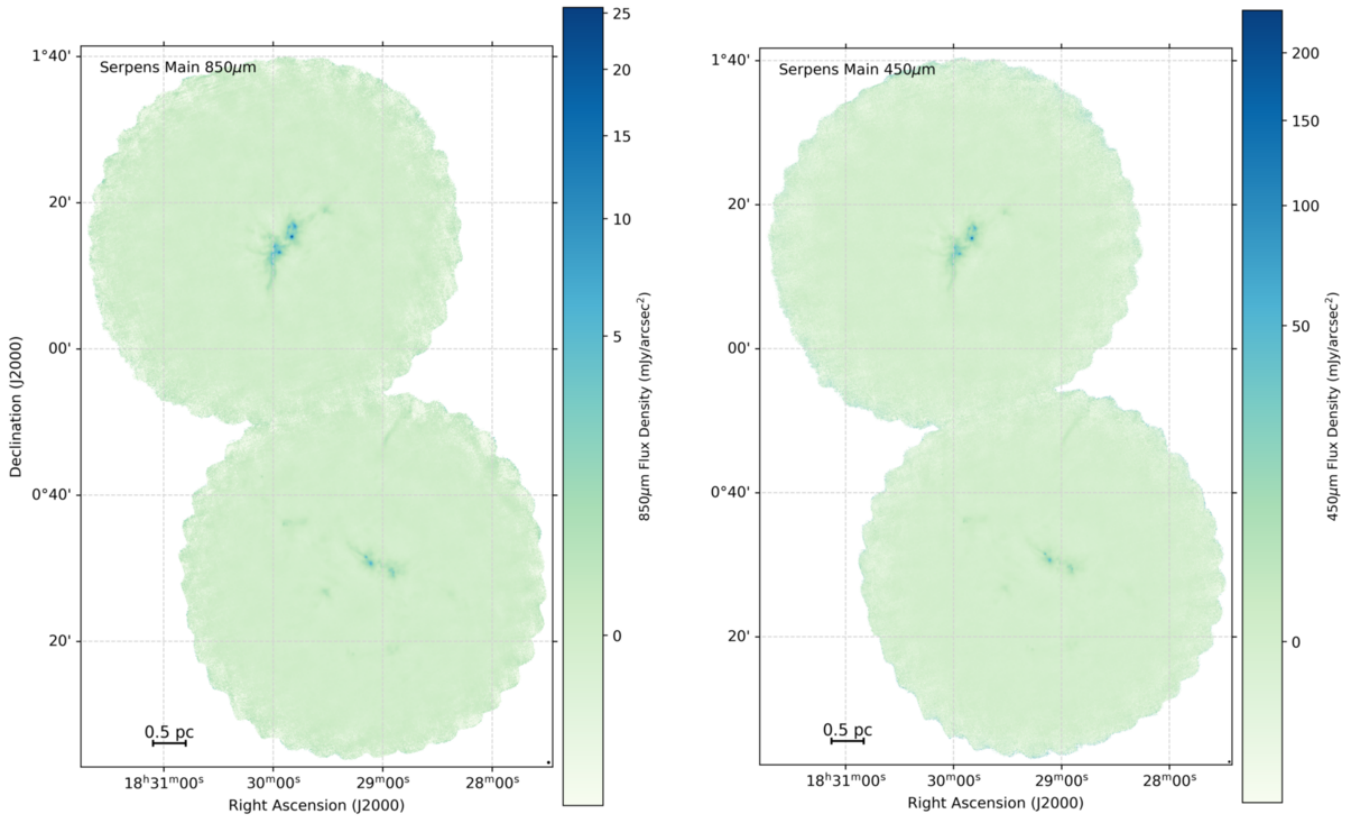


Figure A22. SCUBA-2 850 μm and 450 μm IR3 images of Serpens Main.

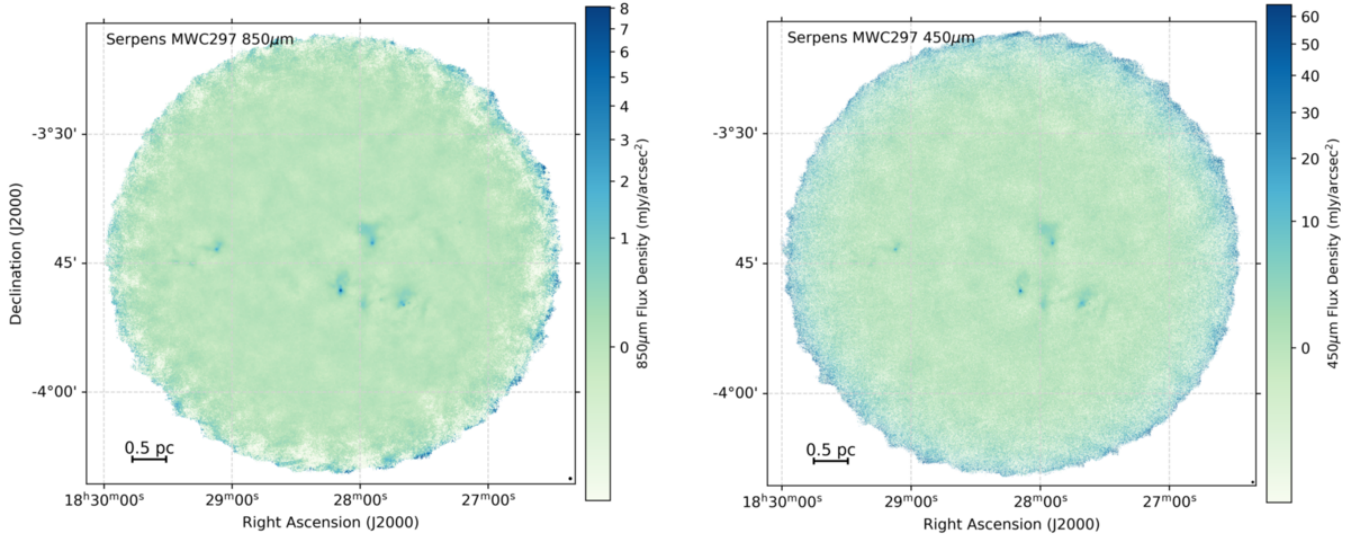


Figure A23. SCUBA-2 850 μm and 450 μm IR3 images of Serpens MWC297.

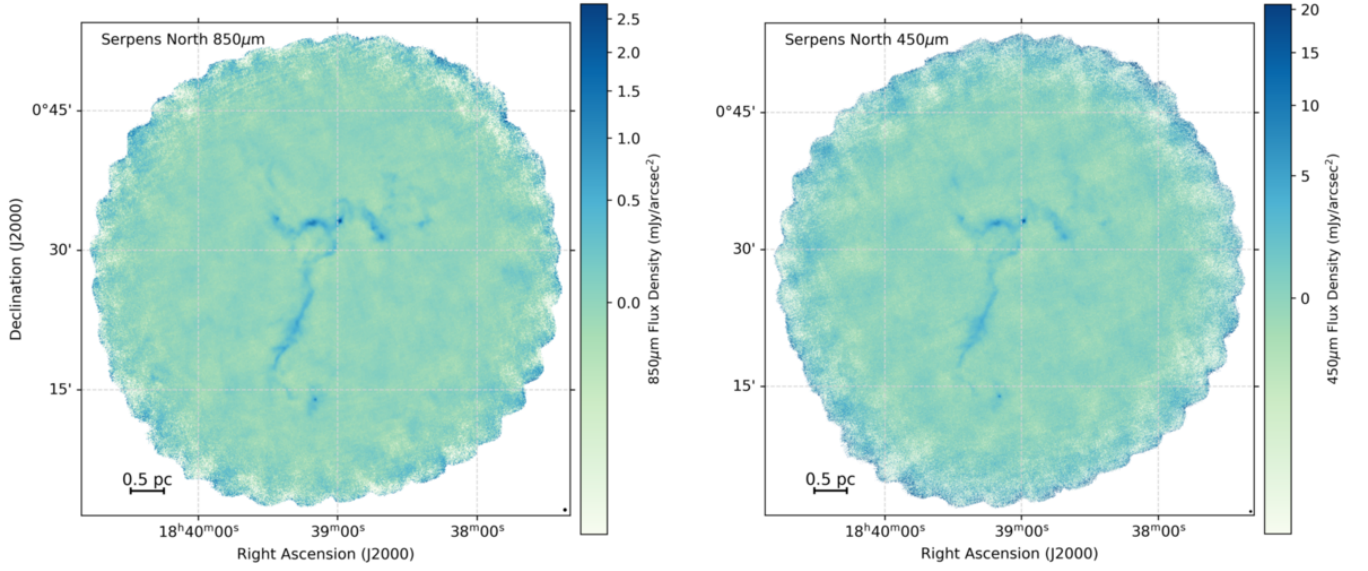


Figure A24. SCUBA-2 850 μm and 450 μm IR3 images of Serpens North.

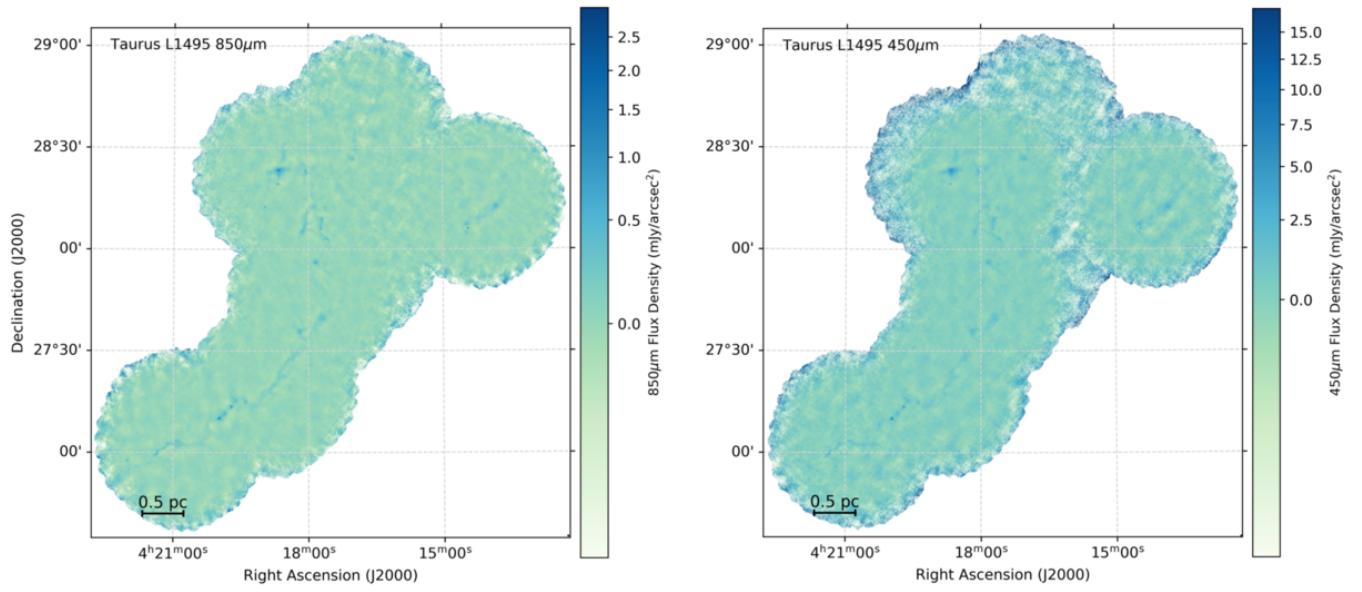


Figure A25. SCUBA-2 850 μm and 450 μm IR3 images of Taurus L1495.

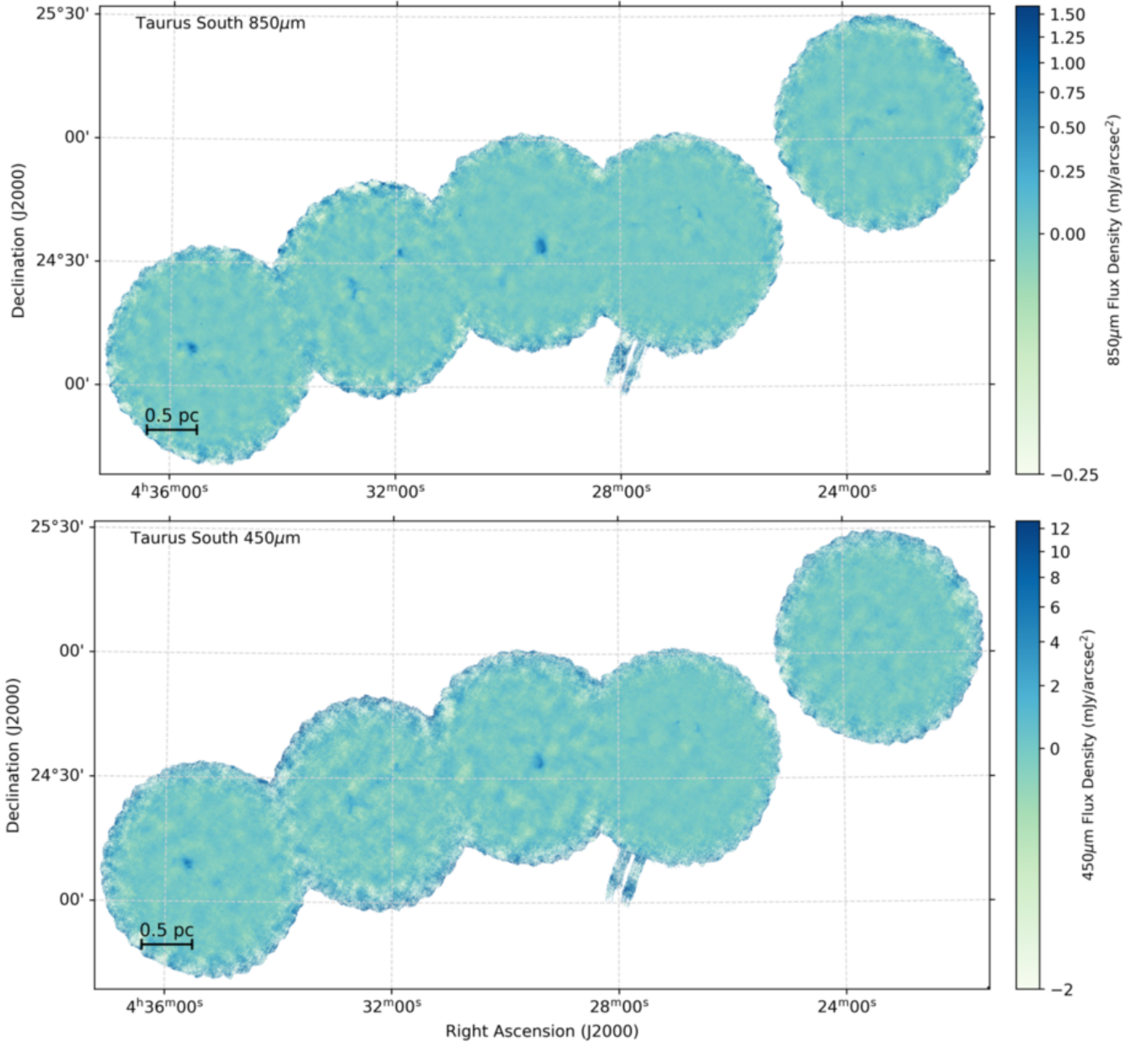


Figure A26. SCUBA-2 850 μ m and 450 μ m IR3 images of Taurus South.

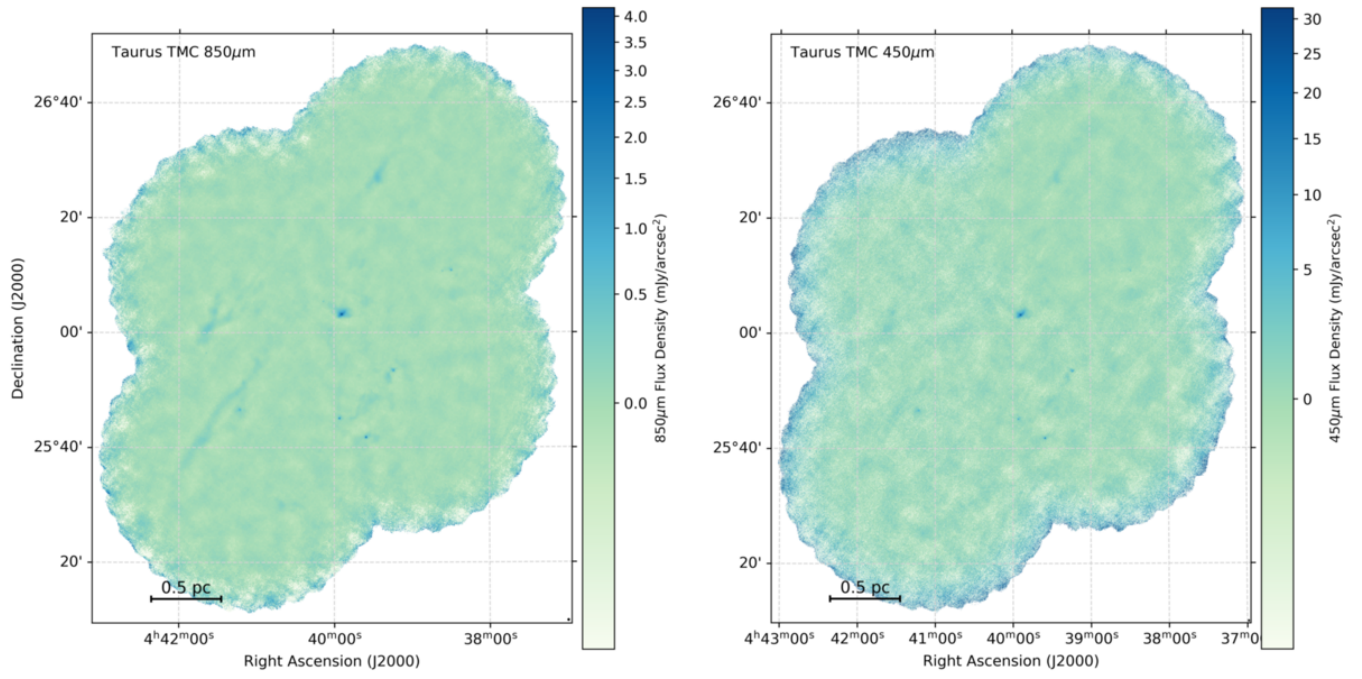


Figure A27. SCUBA-2 850 μm and 450 μm IR3 images of Taurus TMC1.

APPENDIX B: COMPLETENESS TESTING

One question that must be addressed with all ground-based submillimetre observations is the impact of the insensitivity to large-scale emission structures on the accuracy of measurements of smaller-scale emission structures. A first attempt to quantify this for the JCMT GBS was made in Kirk et al. (2018), but this was done under artificial and idealized conditions: artificial Gaussian emission sources of varying peak brightness and size were added to a noise-only field, and were then examined using knowledge of their expected properties. The overall conclusion was that compact sources with Gaussian width $\leq 30''$ and peak brightness at least five times the local noise level were reliably detected, with measured properties lying within 15% of their true input values.

Here, we add several important layers of realism to our completeness testing. First, we model sources as critical Bonnor–Ebert (BEC) spheres, a model which is often found to describe dense cores reasonably well (e.g. Alves et al. 2001). Second, instead of guiding a source-finding algorithm to the input cores, we employ one of the most commonly-used source finders, *getsources* (Men’shchikov et al. 2012), the same algorithm used to produce the GBS core catalogue itself. We also create both 850 μm and 450 μm model emission, and provide both wavelengths as input to *getsources*. This work is the first time that JCMT GBS completeness testing has included model 450 μm data.

These additional layers of testing are essential to interpret our observed core catalogue correctly. For example, interpreting the observed core mass function requires knowledge of the source completeness as a function of mass, as well as by the fraction of mass recovered relative to the true core mass. Kirk et al. (2018) provided results in the best-case scenario, while here we employ a more realistic approach which includes the effects of the source identification algorithm. We note that these current tests still neglect the influence of source crowding and variable backgrounds which could be additional important factors in some of our observed regions.

For our completeness testing, we inserted model Bonnor–Ebert spheres into the Oph/Sco N6 field, an observed GBS field which appears to be devoid of real source emission. This field provides a good worst-case scenario, in that it was one of many areas observed in JCMT Weather Band 2 ($0.05 < \tau_{225\text{GHz}} < 0.08$; Dempsey et al. 2013), and so has poorer 450 μm noise properties than do fields observed in JCMT Weather Band 1 ($\tau_{225\text{GHz}} < 0.05$). We might expect *getsources* to perform slightly better in regions observed in Band 1, since the 450 μm data would have better SNR. However, Band 1 weather was used to observe regions known to contain many bright sources, and so we do not have an equivalent ‘noise-only’ Band 1 pointing to use for completeness testing.

The following subsections describe our artificial source testing procedure in more detail.

B1 General Setup

Much of the basic set-up mimics what was used in Kirk et al. (2018), and the reader is referred there for further details. We inserted model Bonnor–Ebert spheres into the Oph/Sco N6 field, as discussed above. There are two areas in Oph/Sco N6 where potential ($< 3\sigma$) emission is present, which we excluded from the area where artificial sources could be placed. We additionally excluded the outer $3'$ edge of the map for placement of artificial sources as the noise is significantly higher there. These areas are shown in Figure 2 of Kirk et al. (2018). Within the remaining map area, for each set of Bonnor–Ebert sphere model parameters, we placed model sources as described in

Section B2.2. The artificial sources were added directly to the time stream of the raw observations, and the data then processed using the procedure used to reduce the maps used in this work – i.e. that which the GBS has found best recovers extended emission (DR2). Each of the six independent observations of the Oph/Sco N6 field were reduced independently using the DR2 automask procedure. The reduced maps were then mosaicked and masks (identifying areas of likely real emission) created. A second round of reduction was then run using the masks, again following the DR2 external mask procedure, and the resulting images were mosaicked together once more. We did not introduce any telescope pointing errors between the six observations, hence the additional post-processing corrections employed for DR3 were not applicable.

B2 BEC Sphere Models

B2.1 Making critical Bonnor–Ebert sphere models

We generated the flux density distribution of a BEC sphere at 850 μm and 450 μm for each of the range of masses M and distances D which we wished to test. In each case we assumed $T = 15\text{ K}$, $\beta = 1.8$, $\kappa_0 = 0.01\text{ m}^2\text{kg}^{-1}$ at 1 THz.

The density distribution of a BEC sphere of central density ρ_c is given by (Ebert 1955; Bonnor 1956)

$$\rho = \rho_c \exp(-\psi(\xi)), \quad (\text{B1})$$

where ξ is a function of core radius r , such that

$$\xi = r \left(\frac{4\pi G \rho_c}{c_s^2} \right)^{\frac{1}{2}}, \quad (\text{B2})$$

and $\psi(\xi)$ is implicitly defined via the Lane–Emden equation,

$$\xi^{-2} \frac{d}{d\xi} \left(\xi^2 \frac{d\psi}{d\xi} \right) = \exp(-\psi) \quad (\text{B3})$$

for boundary conditions $\psi(\xi = 0) = 0$ and $d\psi/d\xi|_{\xi=0} = 0$. The mass of the sphere within a dimensionless radius ξ_0 is given by

$$M = \frac{c_s^3}{(4\pi G^3 \rho_c)^{\frac{1}{2}}} \int_0^{\xi_0} \exp(-\psi(\xi)) \xi^2 d\xi \quad (\text{B4})$$

For a source of given mass M , we numerically solved these equations for central radius ρ_c and a dimensionless edge radius ξ_0 , assuming a centre-to-edge density contrast of $\rho/\rho_c = 14.1$ – that of a BEC sphere. We then converted ξ_0 into an edge radius $r_0 = \xi_0 (4\pi G \rho_c / c_s^2)^{-0.5}$, and made a lookup table for ρ as a function of radius r .

We next determined the flux density distribution of the BEC sphere on the 850 μm ($3''$) pixel grid. For a given temperature and constant dust properties, the flux density in a given pixel is proportional to the mass in that pixel, using $F_\nu = M \times (\kappa_\nu B_\nu(T)/D^2)$ (Hildebrand 1983).

We first calculated the angular size of r_0 at our chosen distance. If this angular size was less than $3''$, we simply placed all of the mass in the central pixel.

Otherwise, we found the mass in each pixel as follows. We first calculated the distance of all four corners of the pixel from the centre of the map (the impact parameter b of each corner). If all corners of pixel had $b > r_0$, we set the mass in that pixel to zero.

Otherwise, we picked a random position inside the pixel, and calculated the impact parameter b of that position. If $b > r_0$, we set the mass at that position to zero. Otherwise, we made an array of distances x along the line of sight from 0 to the edge of the sphere,

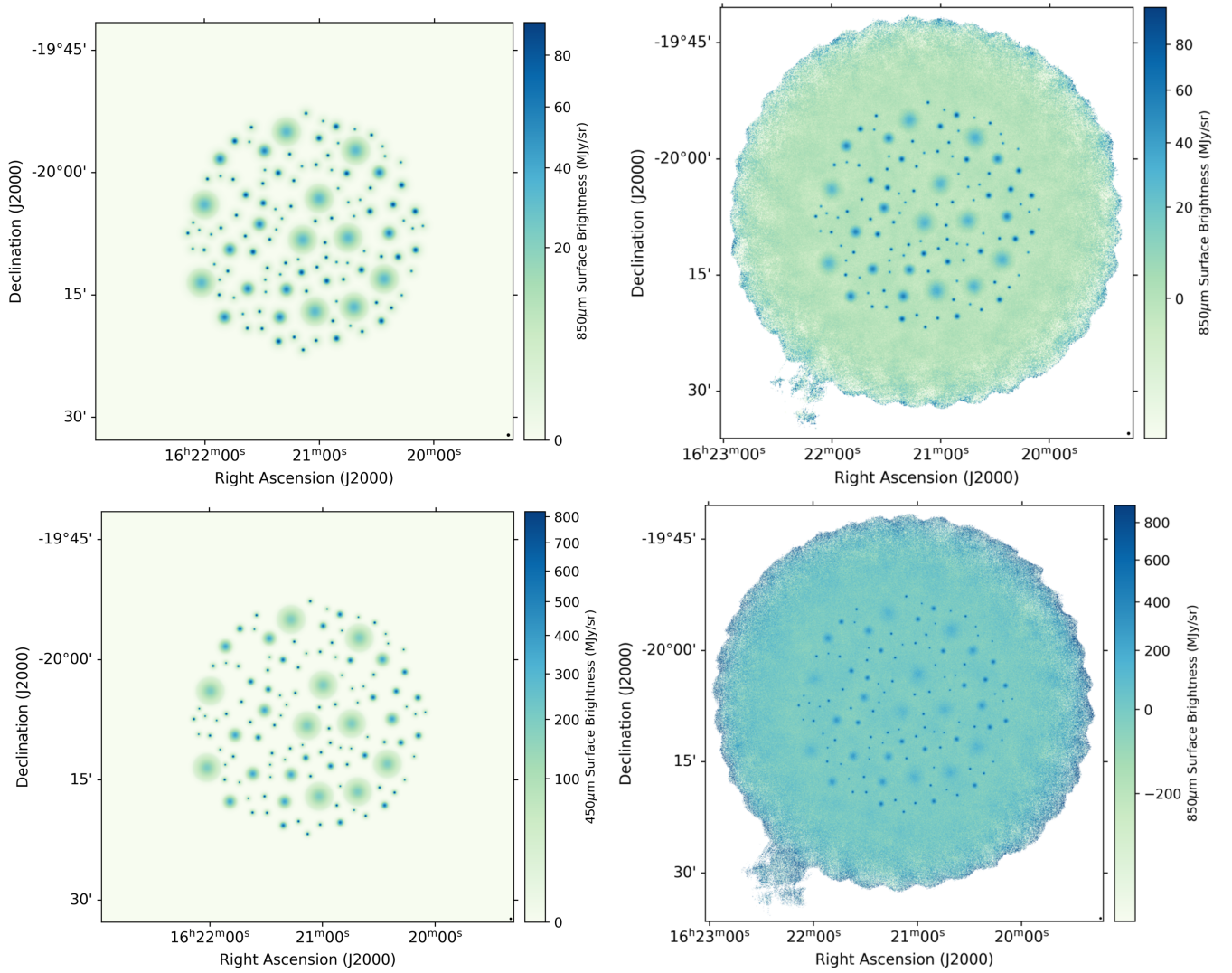


Figure B1. BEC spheres in the mass range $0.1\text{--}2.0\text{ M}_{\odot}$, placed at a distance of 150 pc. *Top left:* 850 μm model sources. *Top right:* 850 μm model sources, after having been inserted into the Oph/Sco N6 field and processed through the SCUBA-2 pipeline. *Bottom left:* 450 μm model sources. *Bottom right:* 450 μm model sources, after processing through the SCUBA-2 pipeline.

where x is defined relative to the plane of the centre of the sphere, and calculated radii for each of these distances, such that $r = \sqrt{x^2 + b^2}$. We then created an array of density values $\rho(x)$ by interpolating our $\rho(r)$ lookup table for our $r(x, b)$ values. We integrated under this $\rho(x, b)$ curve using the trapezium rule, and then doubled this value to account for both hemispheres of the sphere, giving the mass along this line of sight. We repeated this process 1000 time, and took the mean of these 1000 values to find the average mass in the pixel. Pixels with equal central impact parameters were filled by symmetry.

To check the accuracy of our calculation, we summed over all of the pixels in the array. If the returned mass differed from the input BEC sphere mass by $> 1\%$, we repeated the calculation until our required tolerance was achieved.

To create the 850 μm flux density map, we multiplied the mass distribution by $\kappa_{\nu} B_{\nu}(T)/D^2$ where $\nu = \nu(850\mu\text{m})$. We then smoothed the map with the two-component JCMT 850 μm beam model (Dempsey et al. 2013). This gave us the 850 μm flux density map of the BEC sphere at the resolution of the JCMT.

To create the 450 μm map, we reprojected the 850 μm mass dis-

tribution to the 450 μm pixel grid. Since both the 850 μm ($3''$) and 450 μm ($2''$) pixel grids are significantly smaller than the 450 μm primary beam size, this approach does not cause us any loss of 450 μm resolution, while significantly shortening the time required for mass calculations and, through use of exact reprojection routines, the certainty that both wavelengths were centred on precisely the same position. We then multiplied the mass distribution by $\kappa_{\nu} B_{\nu}(T)/D^2$ where $\nu = \nu(450\mu\text{m})$, and smoothed the map with the two-component JCMT 450 μm beam model (Dempsey et al. 2013), giving us the 450 μm flux density map of the BEC sphere at the resolution of the JCMT.

B2.2 Placing BEC spheres on map

We began the process of placing cores by generating a suitable list of x and y coordinates. For each field, we defined a target number of cores of each mass to place, and a maximum number of attempts to make to place sources of that mass. We also wished to ensure that the sources placed did not overlap with one another significantly, and

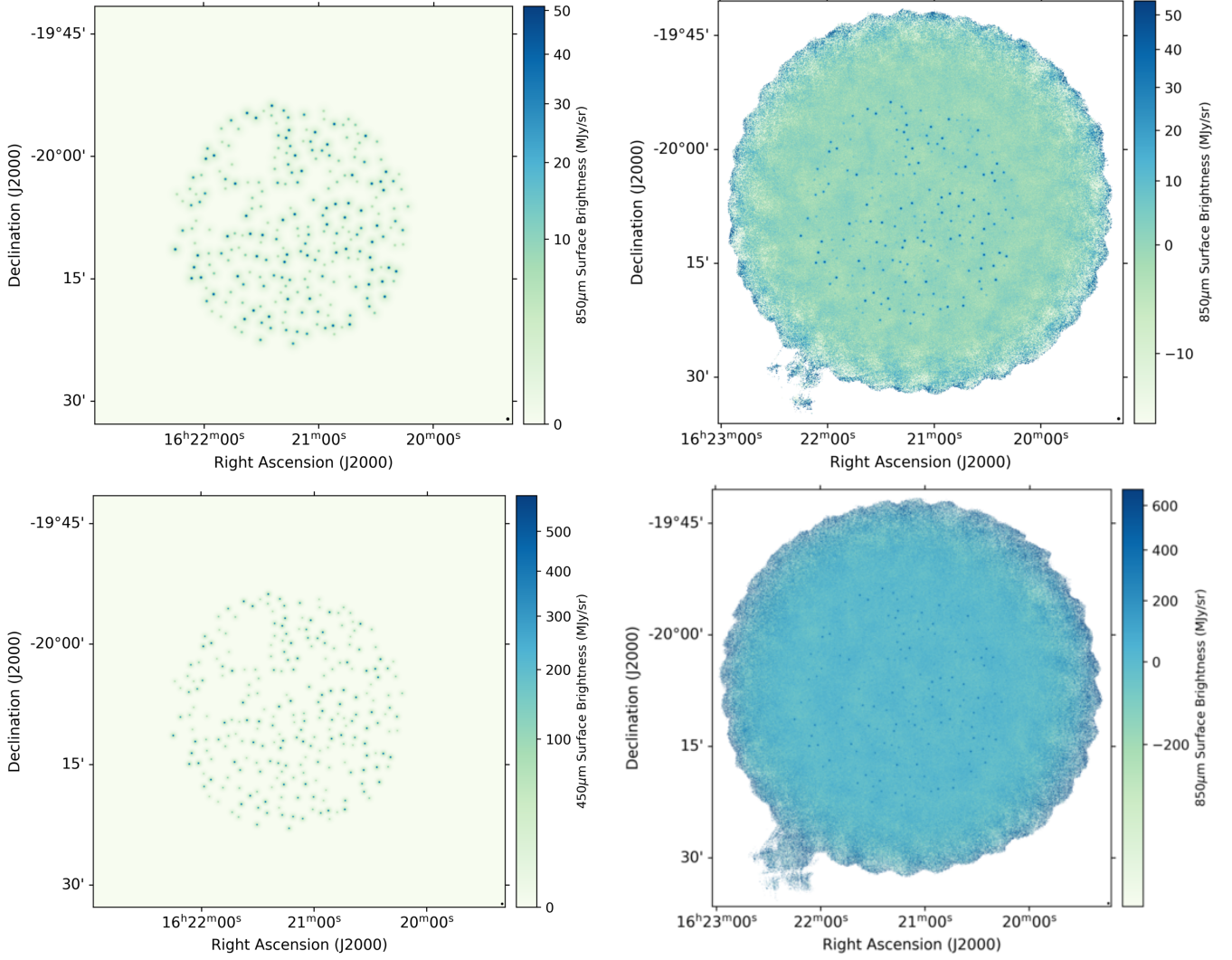


Figure B2. BEC spheres in the mass range $0.01\text{--}0.075\,M_{\odot}$, placed at a distance of 150 pc. Panels as in Figure B1.

did not fall close to the edge of the map. To this end, we defined an ‘exclusion radius’, r_{ex} , for each mass of core, defined as the larger of r_0 and the $850\,\mu\text{m}$ beam FWHM. We further defined, for each mass and distance, an empirical factor M_{ex} by which r_{ex} should be multiplied, in order to prevent significant overlap of sources.

Until either the target number of sources or the maximum number of attempts was reached, the following process was performed:

- (i) Randomly select a pair of x and y coordinates within the field, defined relative to the map centre.
- (ii) If $\sqrt{x^2 + y^2} < 900'' - 3r_{ex}$, discard the position and retry.
- (iii) The (x, y) coordinate pair was compared to the list of previously placed sources, of all masses. If the distance between the source and any other placed source is less than the sum of the $M_{ex} \times r_{ex}$ values of the two sources, discard the position and retry.
- (iv) Otherwise, place a model source at these (x, y) coordinates and record its mass.

This process was then repeated for the next mass under consideration, progressing from highest to lowest mass. The sources placed, along with the target number of sources, maximum number of tries, and r_{ex} multipliers for each mass, are listed in Table B1. We then used the

list of source positions and masses and create an equivalent $450\,\mu\text{m}$ map.

This process was performed using the first of the six observations of the field. This map was then exactly reprojected to the World Coordinate System (WCS) frames of the other five observations using the *reproject* package in Python.

Our fields of model BEC spheres are shown at $850\,\mu\text{m}$ and $450\,\mu\text{m}$ in the top and bottom left-hand panels of Figures B1–B5, respectively.

B2.3 Re-reducing SCUBA-2 field with fake sources added

We produced SCUBA-2 “observations” of our fields of model BEC spheres by adding the maps to our SCUBA-2 observations of the empty Oph/Sco N6 field. To do so, we first ‘uncalibrated’ the maps into pW using the SCUBA-2 flux conversion factors given by Dempsey et al. (2013). The fields of fake sources were added to each of the observations of the Oph/Sco N6 field using the *fakemap* parameter, which allows the user to provide an image of the sky that will produce corresponding additional astronomical signal in the SCUBA-2 bolometer time series, in *makemap* (Chapin et al. 2013), and the data reduction procedure for the field as described in Sec-

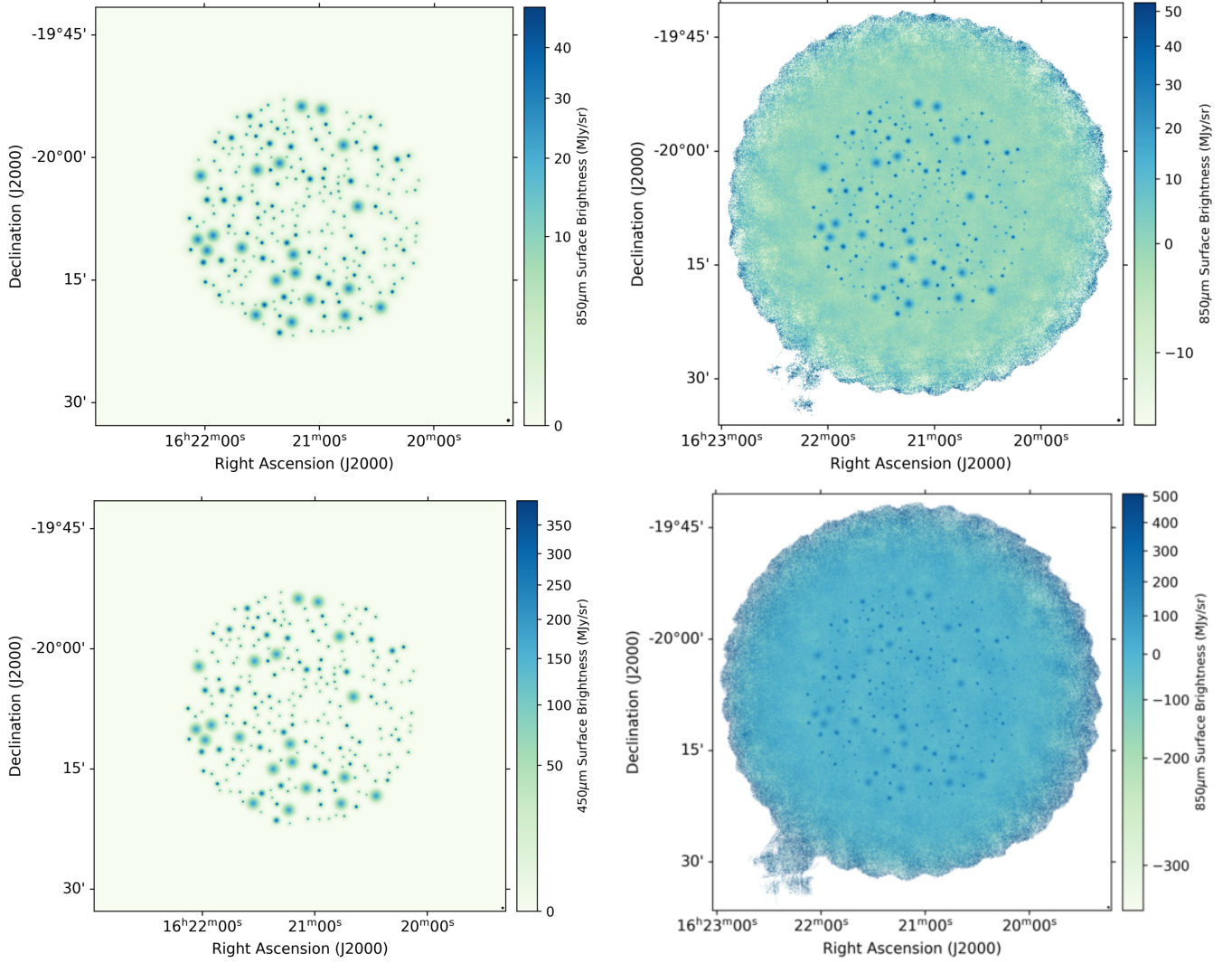


Figure B3. BEC spheres in the mass range $0.1\text{--}2.0\,M_{\odot}$, placed at a distance of 300 pc. Panels as in Figure B1.

tion 2 and by Kirk et al. (2018) was repeated, including creation of a fixed mask. This process is described in detail by Sadavoy et al. (2013). We then calibrated and coadded the reduced maps to produce final maps of fake sources at $850\,\mu\text{m}$ and $450\,\mu\text{m}$. These final maps are shown at $850\,\mu\text{m}$ and $450\,\mu\text{m}$ in the top and bottom right-hand panels of Figures B1–B5, respectively.

B3 Fake Source Identification

We next attempted to identify the model cores in our data. We first ran *getsources* on our fields of fake sources, with a set-up identical to that used on our real maps, as described in Section 3.1. We then applied the selection criteria listed in Section 3.2 the source catalogue returned by *getsources* in order to produce final catalogues of fake sources which have been treated identically to our real data throughout.

The number of sources recovered in each field and for each mass are listed in Table B1.

B4 Results

The results of our completeness testing are described in Section 3.4 in the main body of the paper.

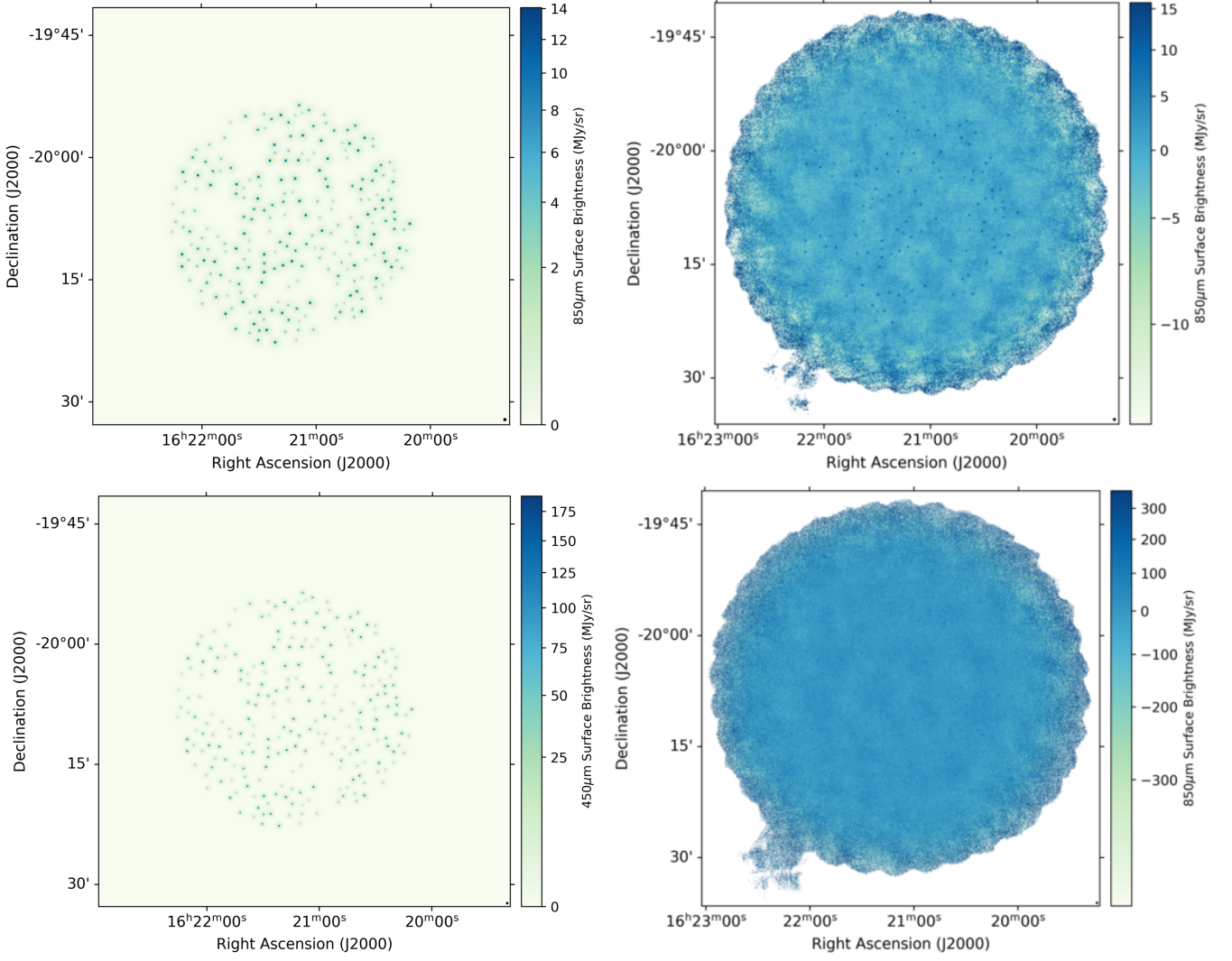


Figure B4. BEC spheres in the mass range $0.01\text{--}0.075\text{ }M_{\odot}$, placed at a distance of 300 pc. Panels as in Figure B1.

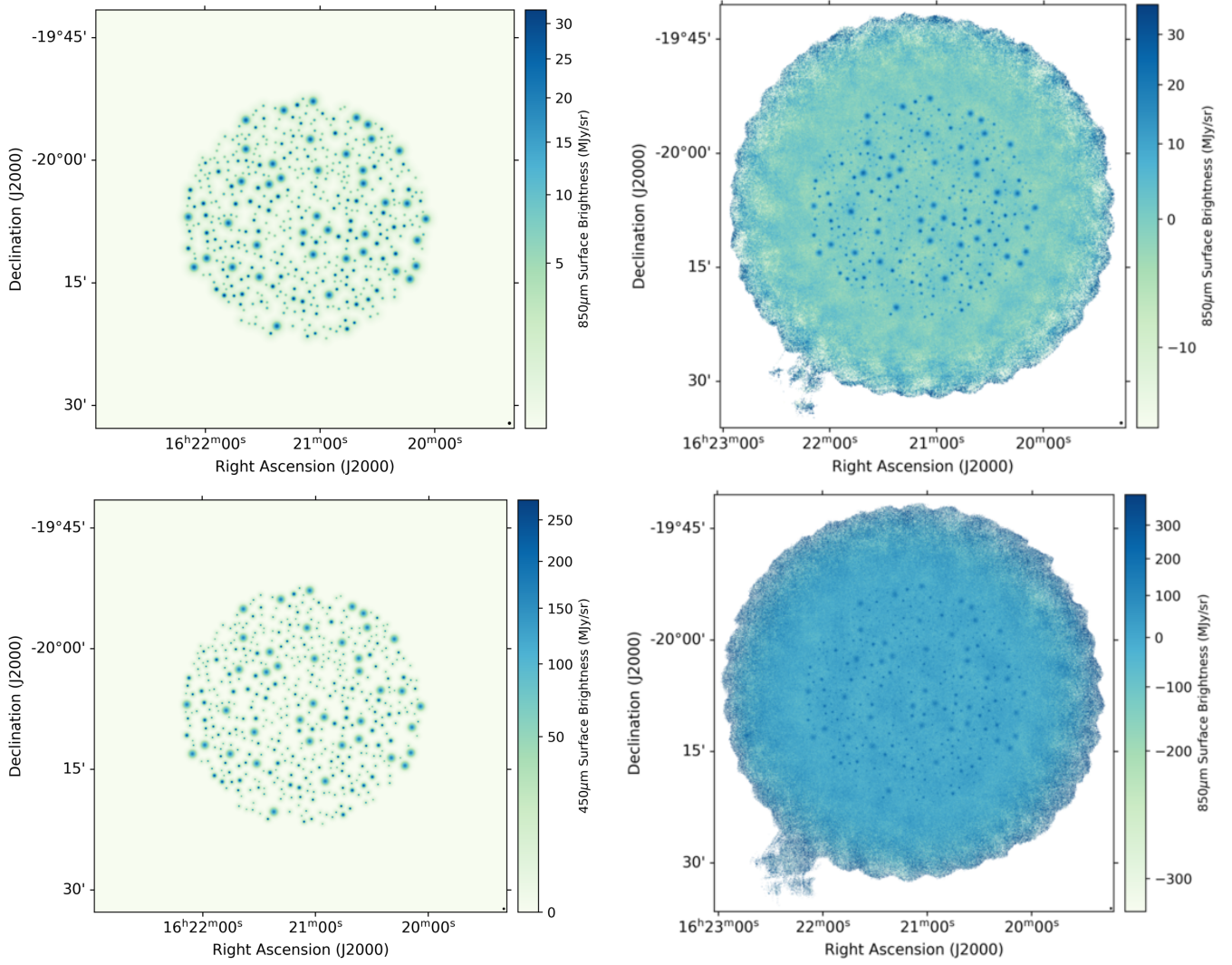


Figure B5. BEC spheres in the mass range $0.1\text{--}2.0\,M_{\odot}$, placed at a distance of 450 pc. Panels as in Figure B1.

Table B1. BE sphere placement properties

150 pc									
Mass (M_{\odot})									
	0.01	0.02	0.05	0.075	0.1	0.2	0.5	1.0	2.0
Target to place	60	60	60	60	40	40	20	10	10
Maximum tries	16000	8000	2000	2000	16000	16000	8000	2000	2000
Exclusion multiplier	8	8	8	8	4	6	8	10	12
Sources placed	60	60	60	60	18	23	20	10	10
Sources recovered	0	51	60	60	18	23	20	10	10
Fraction recovered	0.00	0.85	1.00	1.00	1.00	1.00	1.00	1.00	1.00
$\langle M_{\text{recovered}} \rangle (M_{\odot})$	–	0.014±0.002	0.035±0.002	0.053±0.002	0.069±0.002	0.138±0.006	0.399±0.008	0.86±0.06	1.5±0.2
$\langle M_{\text{recovered}}/M \rangle$	–	0.7±0.1	0.70±0.04	0.71±0.03	0.69±0.02	0.69±0.03	0.80±0.02	0.86±0.06	0.74±0.09
300 pc									
Mass (M_{\odot})									
	0.01	0.02	0.05	0.075	0.1	0.2	0.5	1.0	2.0
Target to place	60	60	60	60	80	80	40	20	20
Maximum tries	16000	8000	2000	2000	16000	16000	8000	2000	2000
Exclusion multiplier	8	8	8	8	3	9	12	15	18
Sources placed	60	60	60	60	60	75	40	20	20
Sources recovered	0	0	1	52	58	75	40	20	20
Fraction recovered	0.00	0.00	0.02	0.87	0.97	1.00	1.00	1.00	1.00
$\langle M_{\text{recovered}} \rangle (M_{\odot})$	–	–	0.042	0.06±0.02	0.069±0.008	0.14±0.01	0.34±0.02	0.79±0.04	1.7±0.1
$\langle M_{\text{recovered}}/M \rangle$	–	–	0.84	0.8±0.2	0.69±0.08	0.69±0.05	0.68±0.03	0.79±0.04	0.83±0.07
450 pc									
Mass (M_{\odot})									
	0.01	0.02	0.05	0.075	0.1	0.2	0.5	1.0	2.0
Target to place	–	–	–	–	160	160	80	40	40
Maximum tries	–	–	–	–	16000	16000	8000	2000	2000
Exclusion multiplier	–	–	–	–	8	12	16	20	24
Sources placed	–	–	–	–	62	27	22	29	40
Sources recovered	–	–	–	–	0	25	22	29	40
Fraction recovered	–	–	–	–	0.00	0.93	1.00	1.00	1.00
$\langle M_{\text{recovered}} \rangle (M_{\odot})$	–	–	–	–	–	0.13±0.02	0.33±0.02	0.72±0.06	1.6±0.2
$\langle M_{\text{recovered}}/M \rangle$	–	–	–	–	–	0.7±0.1	0.65±0.04	0.71±0.06	0.8±0.1

APPENDIX C: ANCILLARY SOURCE CLASSIFICATION PLOTS

The ratio of starless to protostellar cores is shown in Figure C1. The fraction of starless cores which are either robust or candidate prestellar cores is shown for each cloud complex in Figure C2.

APPENDIX D: ANCILLARY MASS AND RADIUS DISTRIBUTIONS

The distributions of starless core masses for each cloud complex as a function of distance are shown in Figure D1, for all cores and for cores with masses above the 90% completeness limit at 450 pc of $0.2 M_{\odot}$. The equivalent distributions of deconvolved starless core radius are shown in Figure D2.

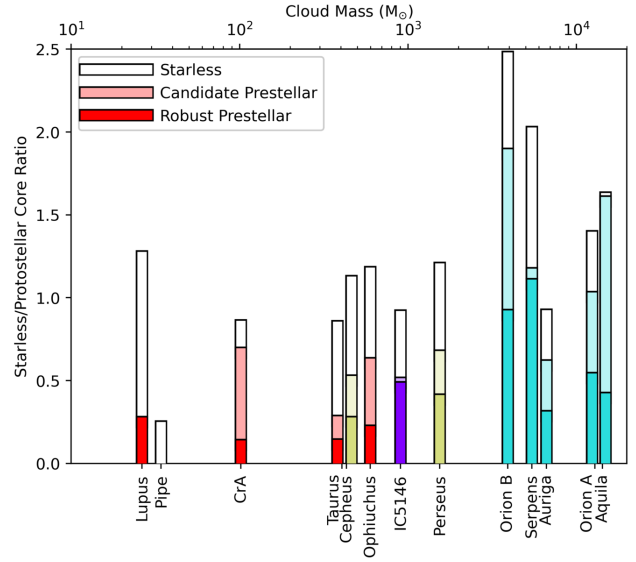


Figure C1. The ratio of starless cores, prestellar cores (candidate and robust prestellar cores), and robust prestellar cores to protostellar cores in each of the cloud complexes that we consider. Note that the bars for Taurus, Cepheus, Orion A and Aquila are slightly offset from their true positions, to avoid overlap. The tick marks associated with these bars show the exact cloud masses.

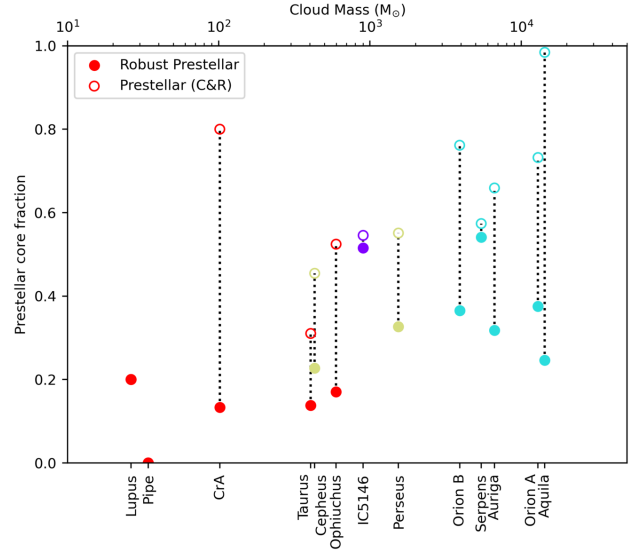


Figure C2. Fraction of starless cores which are prestellar cores (candidate and robust; open circles), or robust prestellar cores (filled circles) as a function of cloud complex mass. Cloud complexes are colour-coded by their distance range.

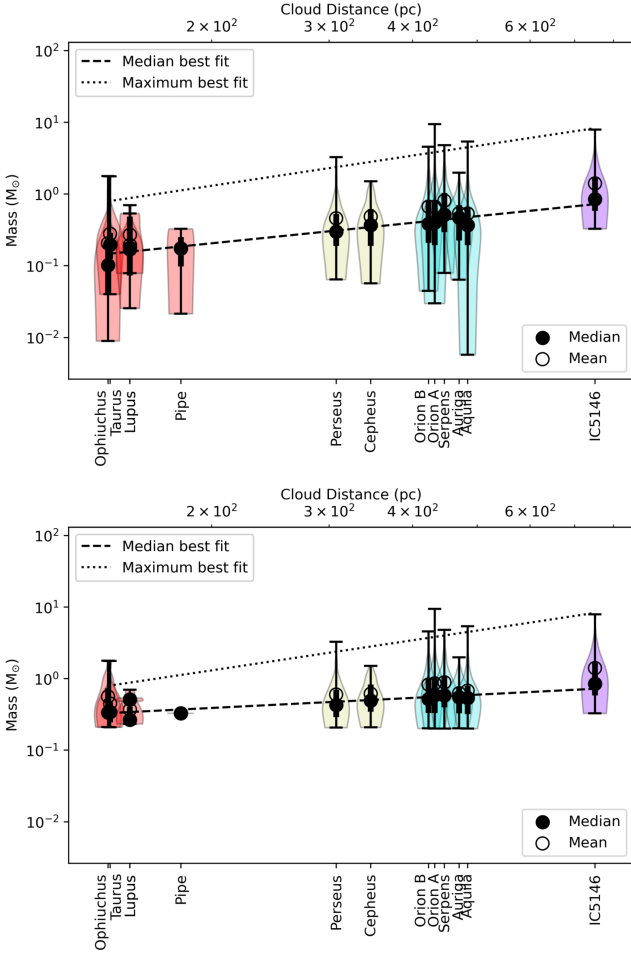


Figure D1. Mass distribution for each cloud complex, as a function of distance. Top: for all starless cores. Bottom: for starless cores with masses above the 90% completeness limit at 450 pc of $0.2 M_{\odot}$. Solid circles show median values; open circles show means. Thick black lines show the interquartile ranges. Dotted line shows the line of best fit to the maximum values in each cloud complex; dashed line shows the line of best fit to the median values.

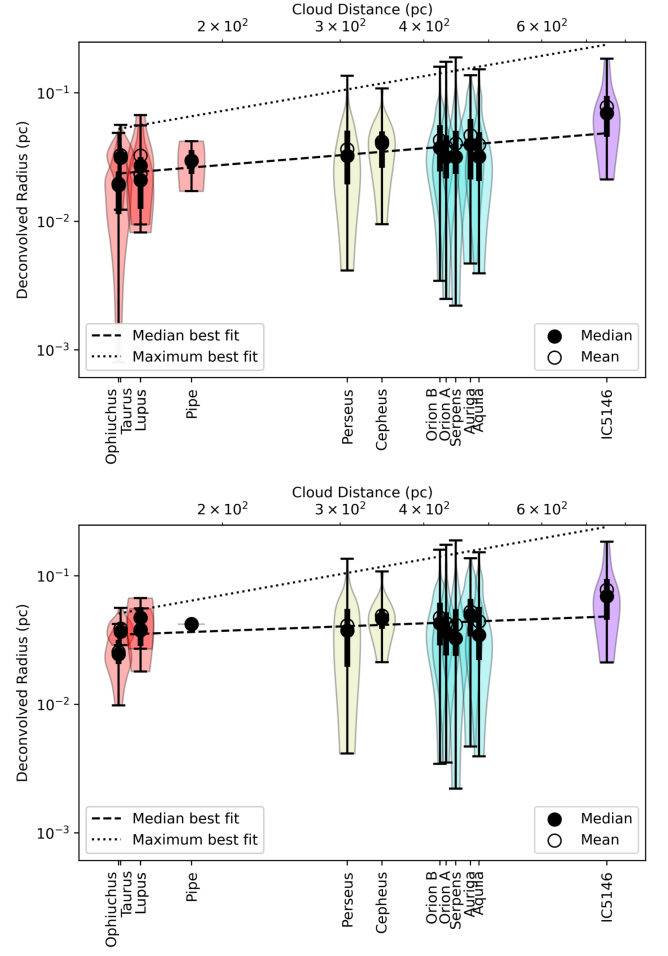


Figure D2. Deconvolved radius distribution for starless cores for each cloud complex, as a function of distance. Top: for all starless cores. Bottom: for starless cores with masses above the 90% completeness limit at 450 pc of $0.2 M_{\odot}$. Solid circles show median values; open circles show means. Thick black lines show the interquartile ranges. Dotted line shows the line of best fit to the maximum values in each cloud complex; dashed line shows the line of best fit to the median values.

APPENDIX E: ANCILLARY CORE MASS FUNCTIONS AND COMPARISONS OF LEAST-SQUARES AND MONTE-CARLO MODELLING

In this section, we show ancillary Core Mass Functions for various subsets of our sample. We first show ancillary results for CMFs plotted by distance (see Section 6.1). Table E1 presents the least-squares best fits to the unbound, candidate prestellar, and robust prestellar cores in our sample. Figure E1 shows the CMF for the far-distance clouds, with cores with temperatures > 15 K excluded. We then show the individual CMFs for each molecular cloud complex that we consider, in Figures E2–E14. Where relevant, the best-fit histogram produced by least-squares (LS) fitting is overplotted. These fits are listed in Table 10 in the text.

E1 Matched-count sampling

As well as the Monte Carlo sampling of the CMFs described in Section 6.1.3, that matched the total mass of the cores in each region, we also investigated a ‘matched count’ sample. In this case, we randomly drew a sample of ‘cores’ equal to the number of cores in the far-distance starless or prestellar sample. From this sample, we then randomly drew a number of ‘cores’ equal to the number of cores in the near-distance starless or prestellar sample, and repeated the exercise for the mid-distance starless or prestellar sample.

Broadly, the matched mass sample and the matched count sample produce very similar mean and median values, with the matched-mass method producing a larger area of the parameter space having at least some consistency with the observed sample.

E2 Comparing Least Squares fits and Monte-Carlo models of CMFs

Figure E16 compares the best-fit least squares (LS) and most-probable Monte Carlo (MC)-derived CMFs for each cloud complex. The two methods produce similar results, although the most probable MC values do not always fall within the LS fitting errors. The LS and MC prestellar CMFs are much more similar to one another than are the LS and MC starless CMFs, likely because the prestellar cores are typically higher-mass, and so their peak masses are better-constrained.

Figures E17 and E18 show the peak masses and widths of the starless and prestellar CMFs, determined using Monte Carlo modelling, as a function of cloud mass.

This paper has been typeset from a \LaTeX file prepared by the author.

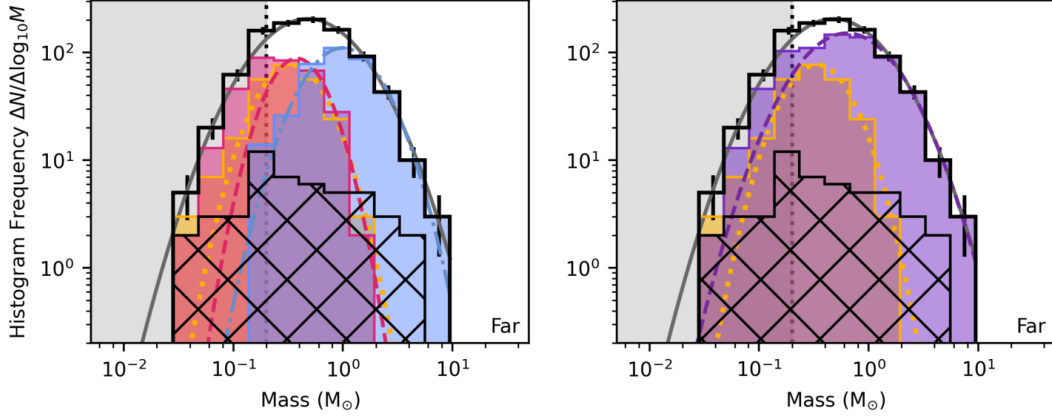


Figure E1. Starless CMF for the far-distance clouds in our sample, with cores in Orion A with temperatures > 15 K excluded. Left: CMFs with fits to full, unbound, candidate prestellar and robust prestellar samples shown. Right: CMFs with fits to full, unbound, and combined candidate and robust (C & R) prestellar samples. In both panels, the unresolved sources are shown as a hatched histogram. Colours of histograms are as in Figure 17.

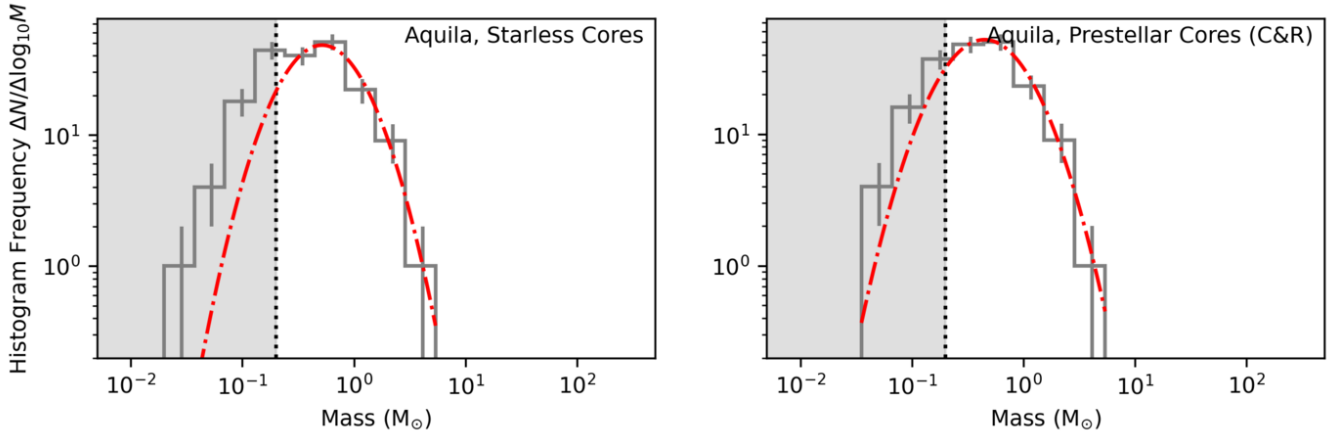


Figure E2. CMFs for Aquila. Left: starless CMF. Right: prestellar (C & R) CMF. Least-squares best-fit model CMFs are shown as red dot-dashed line. Areas below the 90% mass completeness limit are shaded in grey.

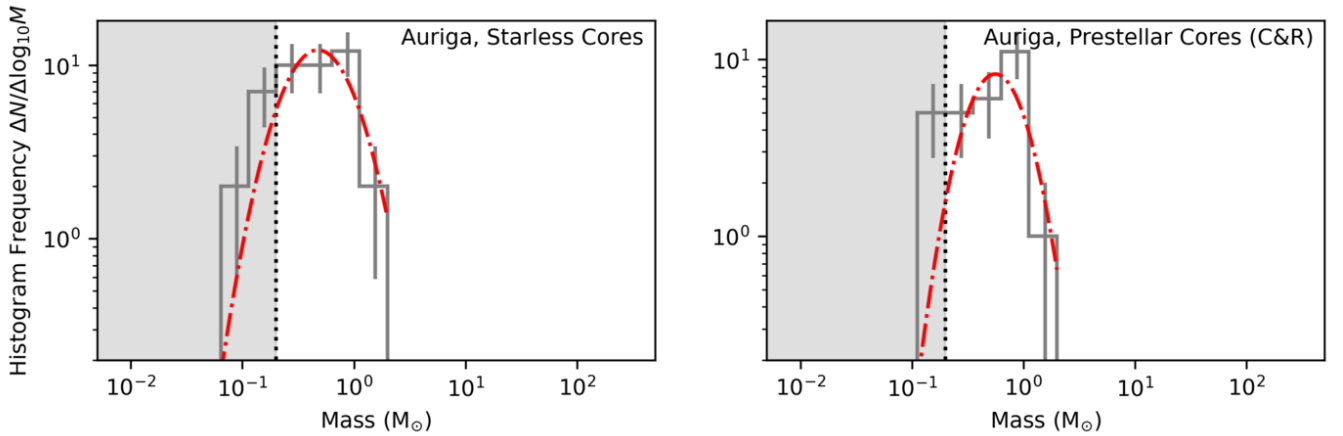


Figure E3. CMFs for Auriga. Left: starless CMF. Right: prestellar (C & R) CMF. Least-squares best-fit model CMFs are shown as red dot-dashed line. Areas below the 90% mass completeness limit are shaded in grey.

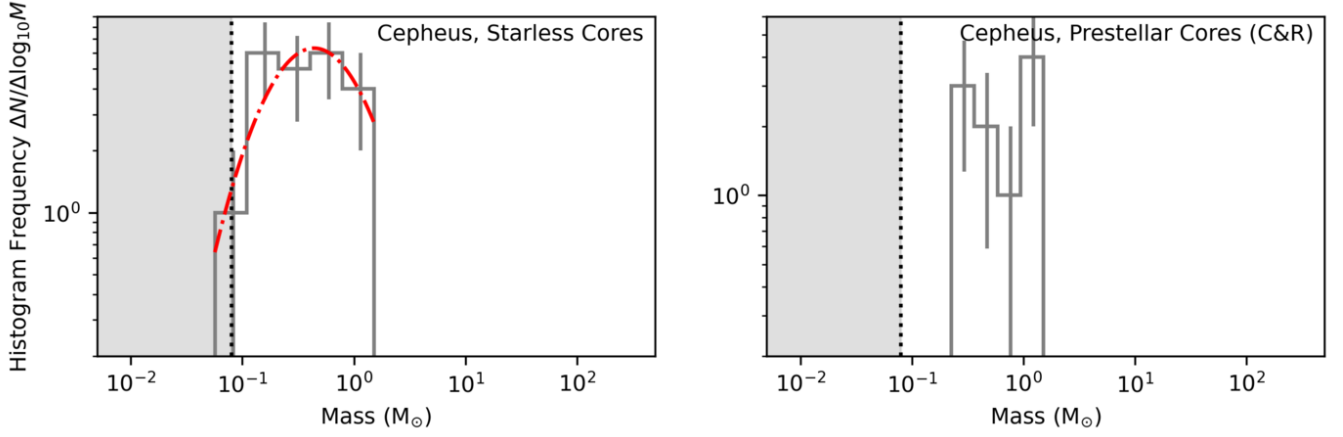


Figure E4. CMFs for Cepheus. Left: starless CMF. Right: prestellar (C & R) CMF. Least-squares best-fit model CMFs are shown as red dot-dashed line. Areas below the 90% mass completeness limit are shaded in grey.

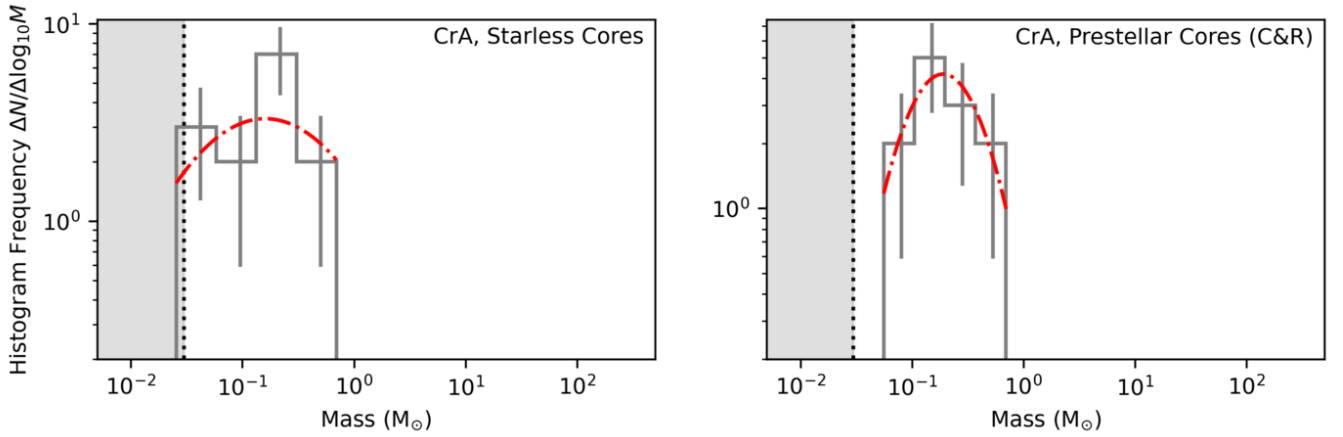


Figure E5. Core mass functions for Corona Australis. Left: starless CMF. Right: prestellar (C & R) CMF. Least-squares best-fit model CMFs are shown as red dot-dashed line. Areas below the 90% mass completeness limit are shaded in grey.

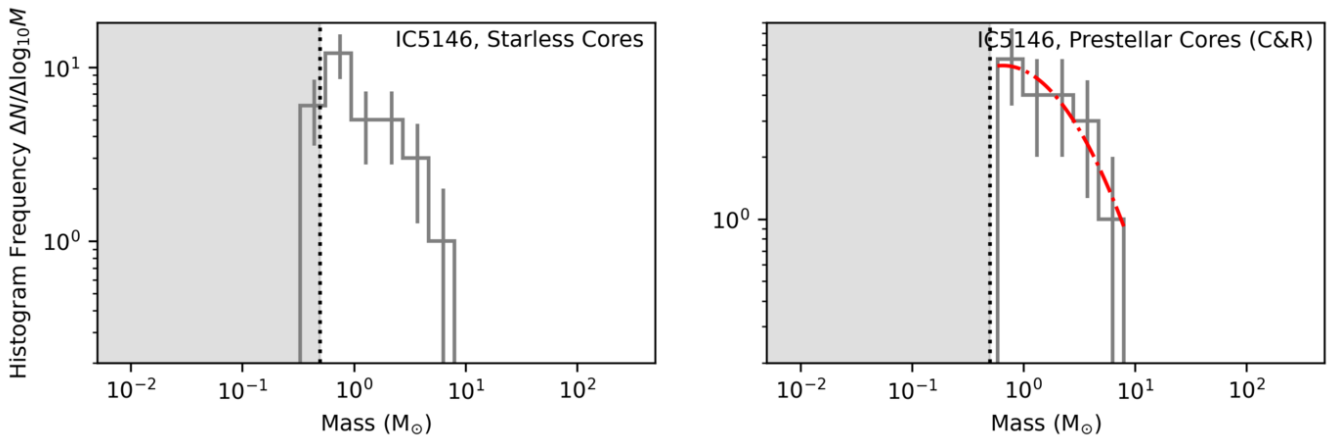


Figure E6. Core mass functions for IC 5146. Left: starless CMF. Right: prestellar (C & R) CMF. Least-squares best-fit model CMFs are shown as red dot-dashed line. Areas below the 90% mass completeness limit are shaded in grey.

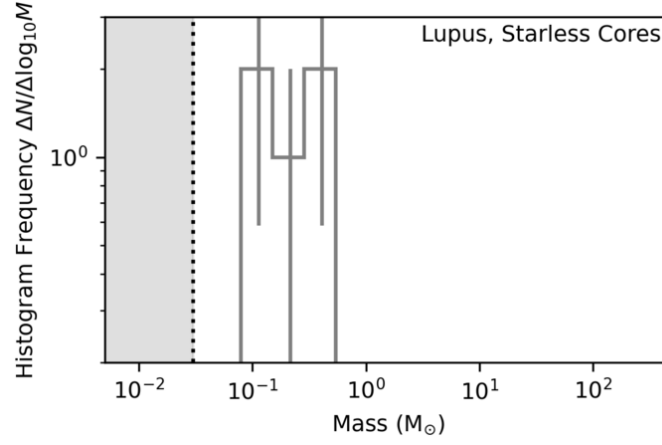


Figure E7. Starless core mass functions for Lupus. Area below the 90% mass completeness limit is shaded in grey.

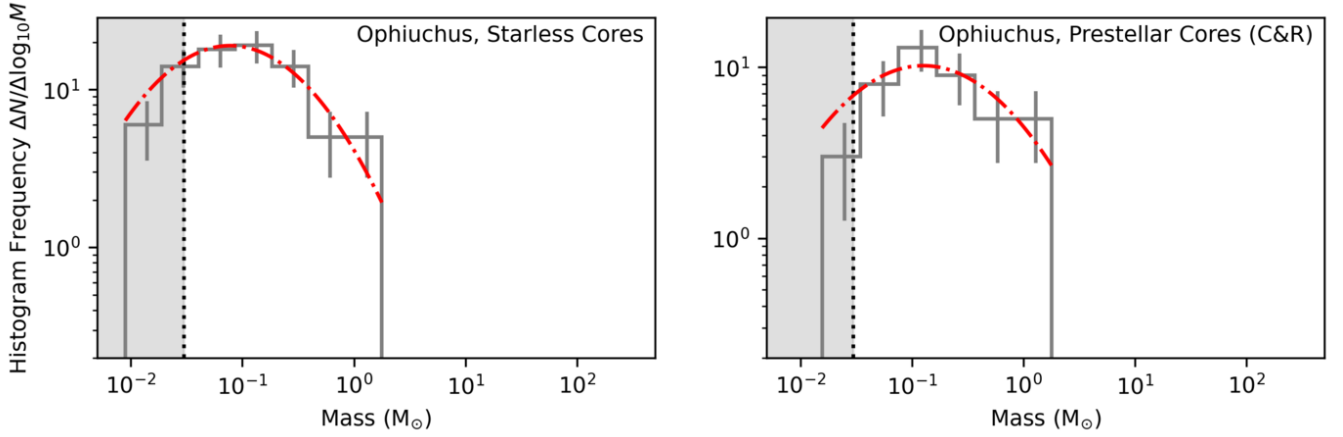


Figure E8. Core mass functions for Ophiuchus. Left: starless CMF. Right: prestellar (C & R) CMF. Least-squares best-fit model CMFs are shown as red dot-dashed line. Areas below the 90% mass completeness limit are shaded in grey.

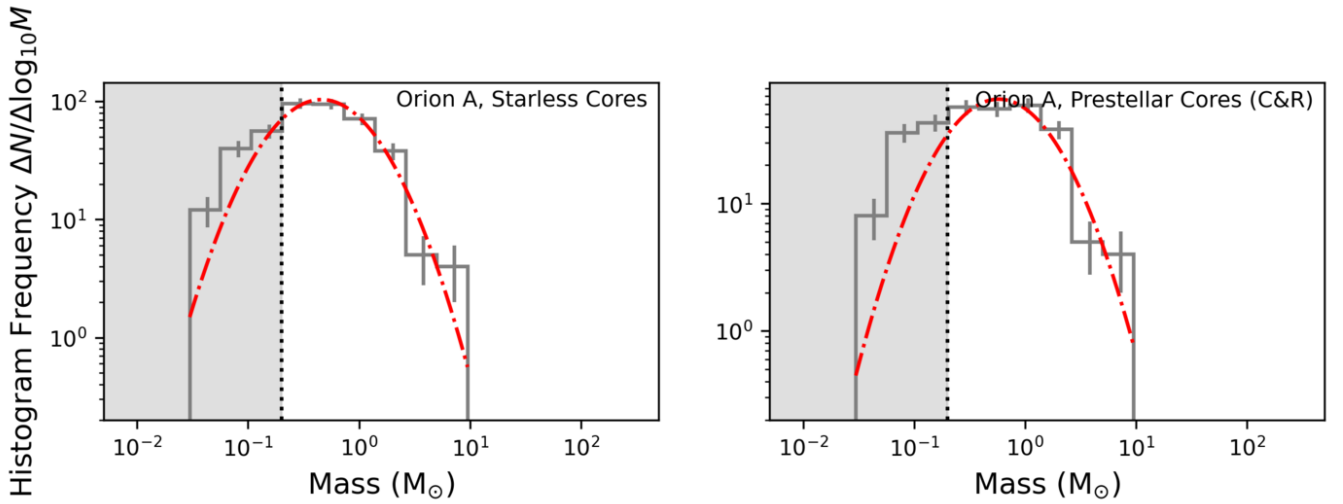


Figure E9. Core mass functions for Orion A. Left: starless CMF. Right: prestellar (C & R) CMF. Least-squares best-fit model CMFs are shown as red dot-dashed line. Areas below the 90% mass completeness limit are shaded in grey.

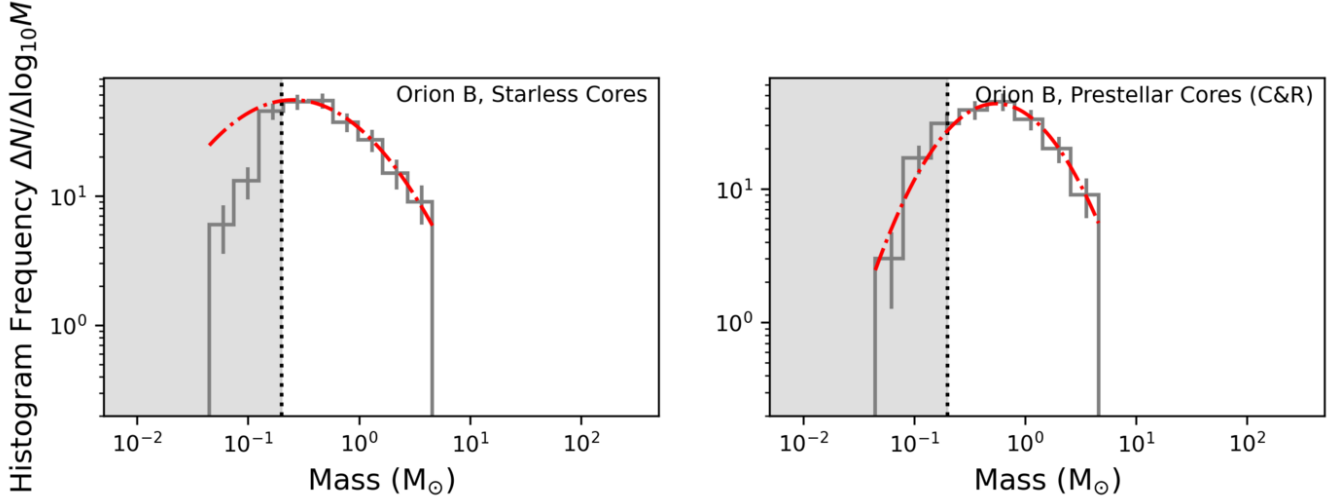


Figure E10. Core mass functions for Orion B. Left: starless CMF. Right: prestellar (C & R) CMF. Least-squares best-fit model CMFs are shown as red dot-dashed line. Areas below the 90% mass completeness limit are shaded in grey.

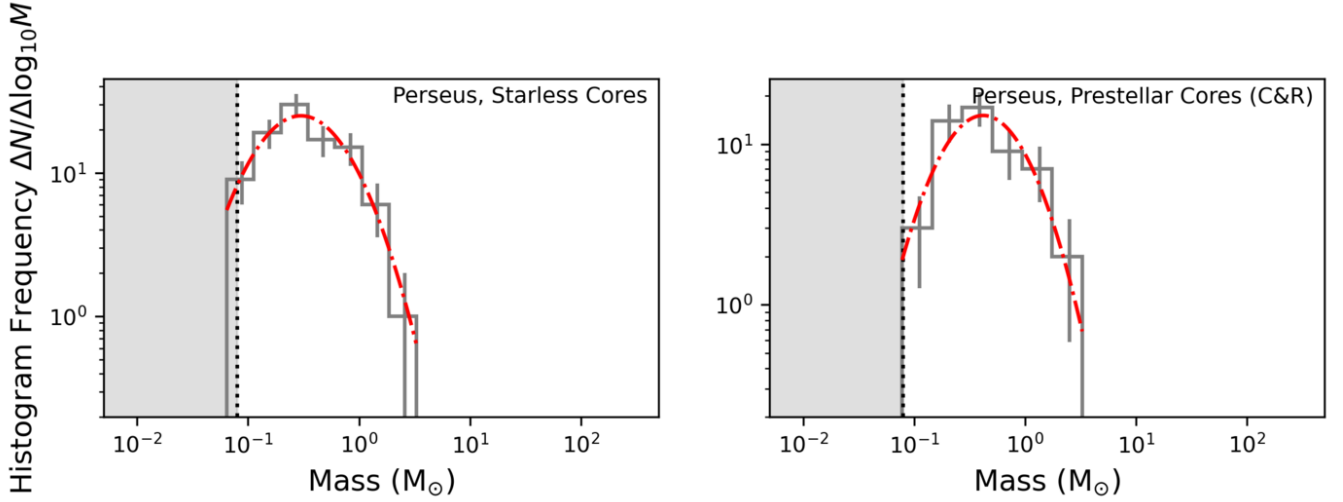


Figure E11. Core mass functions for Perseus. Left: starless CMF. Right: prestellar (C & R) CMF. Least-squares best-fit model CMFs are shown as red dot-dashed line. Areas below the 90% mass completeness limit are shaded in grey.

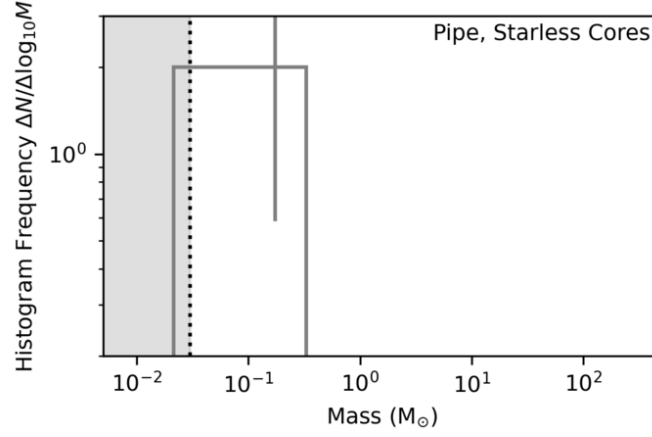


Figure E12. Starless core mass function for the Pipe Nebula. Area below the 90% mass completeness limit is shaded in grey.

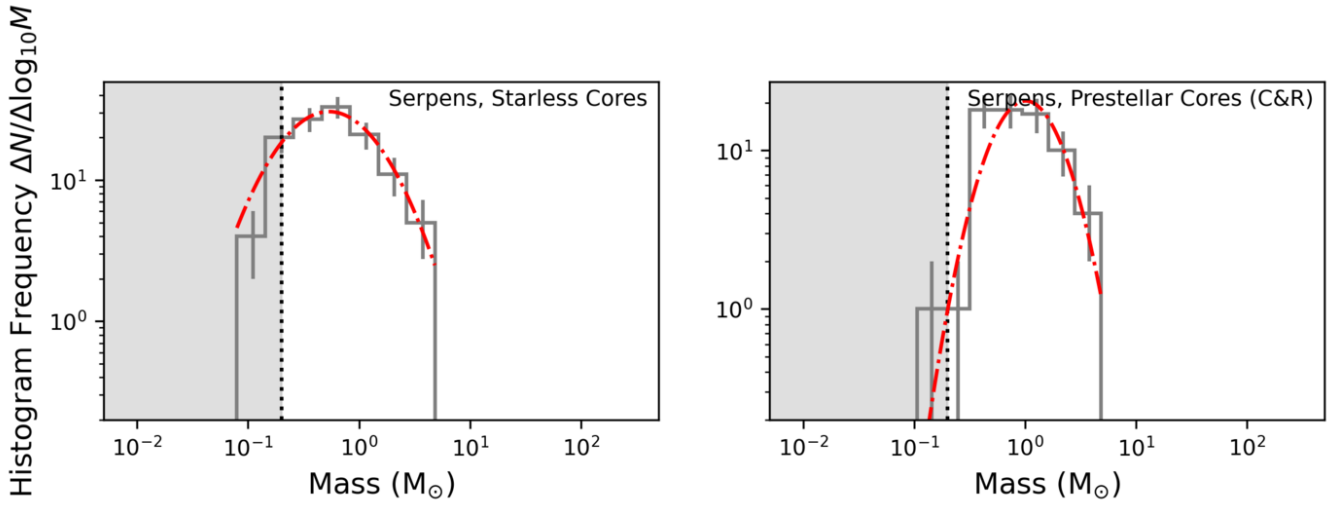


Figure E13. Core mass functions for Serpens. Left: starless CMF. Right: prestellar (C & R) CMF. Least-squares best-fit model CMFs are shown as red dot-dashed line. Areas below the 90% mass completeness limit are shaded in grey.

Table E1. Least-squares best-fit CMFs for each of our distance ranges, for unbound starless cores, candidate prestellar cores, and robust prestellar cores. The final two rows of the table show least-squares best fits to the near- and mid-distance samples, for cores above the far-distance mass completeness limit ($0.2 M_{\odot}$) only.

Range	Unbound			Candidate			Robust		
	A	μ (M_{\odot})	σ ($\log_{10} M_{\odot}$)	A	μ (M_{\odot})	σ ($\log_{10} M_{\odot}$)	A	μ (M_{\odot})	σ ($\log_{10} M_{\odot}$)
0 – 200 pc	16±4	0.12±0.03	0.36±0.08	16±3	0.13±0.01	0.28±0.03	8±1	0.61±0.09	0.38±0.05
200 – 355 pc	15±3	0.2±0.1	0.5±0.2	12.5±0.9	0.25±0.01	0.21±0.01	11±3	0.6±0.1	0.32±0.07
355 – 500 pc	80±10	0.27±0.06	0.30±0.05	100±10	0.31±0.06	0.28±0.05	110±10	0.95±0.05	0.29±0.02
no heated Orion A	77±6	0.34±0.04	0.27±0.03	88±9	0.38±0.04	0.23±0.03	110±4	1.00±0.02	0.30±0.01
> 500 pc	–	–	–	–	–	–	–	–	–
For cores with masses > 0.2 M_{\odot} only									
0 – 200 pc	–	–	–	–	–	–	–	–	–
200 – 355 pc	–	–	–	–	–	–	11±3	0.6±0.1	0.32±0.07

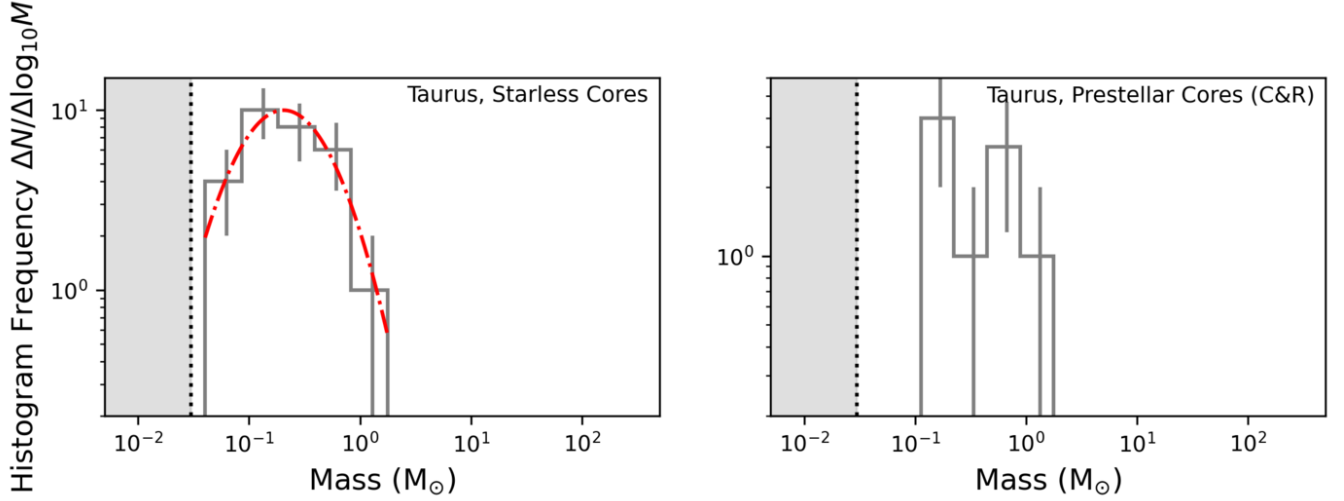


Figure E14. Core mass functions for Taurus. Left: starless CMF. Right: prestellar (C & R) CMF. Least-squares best-fit model CMFs are shown as red dot-dashed line. Areas below the 90% mass completeness limit are shaded in grey.

Table E2. The most probable starless and prestellar CMFs for each distance range that we consider, as determined from Monte Carlo estimation and two-sided KS tests, **using matched-count sampling**. p values show the probability that this model and our sample are drawn from the same underlying distribution.

Range	Starless			Prestellar (C & R)		
	μ (M_{\odot})	σ ($\log_{10} M_{\odot}$)	p	μ (M_{\odot})	σ ($\log_{10} M_{\odot}$)	p
0–200 pc	0.14	0.44	0.80	0.19	0.47	0.77
200–355 pc	0.33	0.36	0.72	0.40	0.35	0.69
355–500 pc	0.40	0.44	0.65	0.56	0.39	0.68

Table E3. The most probable starless and prestellar CMFs for each cloud complex that we consider, as determined from Monte Carlo estimation and two-sided KS tests, **using matched-count sampling**. Median p values, showing the probability that this model and our sample are drawn from the same underlying distribution, are given.

Region	Starless			Prestellar (C & R)		
	μ (M_{\odot})	σ ($\log_{10} M_{\odot}$)	p	μ (M_{\odot})	σ ($\log_{10} M_{\odot}$)	p
Near						
CrA	0.17	0.27	0.77	0.16	0.24	0.87
Ophiuchus	0.10	0.49	0.77	0.15	0.56	0.71
Taurus	0.17	0.26	0.79	–	–	–
Mid						
Cepheus	0.38	0.37	0.83	0.45	0.35	0.79
Perseus	0.31	0.35	0.70	0.38	0.35	0.74
Far						
Aquila	0.39	0.37	0.66	0.41	0.36	0.66
Auriga	0.46	0.31	0.72	0.58	0.24	0.69
Orion A	0.43	0.42	0.53	0.60	0.41	0.53
Orion B	0.35	0.49	0.67	0.55	0.42	0.74
Serpens	0.50	0.40	0.71	0.89	0.27	0.56

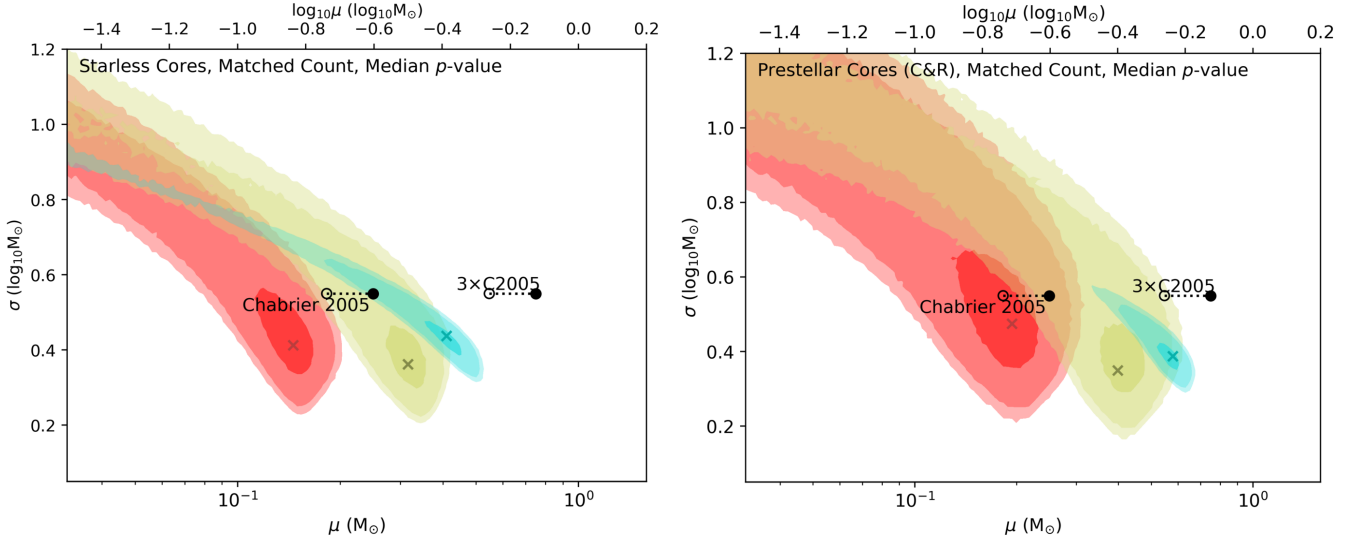


Figure E15. Median p -values for two-sided KS test between model CMFs and starless (left) and prestellar (right) CMFs, using the ‘matched count’ sampling method. Contours show p values of 0.05, 0.1 and 0.5. Red marks near-, green mid- and blue far-distance CMFs. Filled circles mark 1 and $3\times$ the Chabrier (2005) peak system mass ($0.25 M_{\odot}$). Open circles mark $0.73\times$ these values, accounting for the typical flux loss in our SCUBA-2 observations.

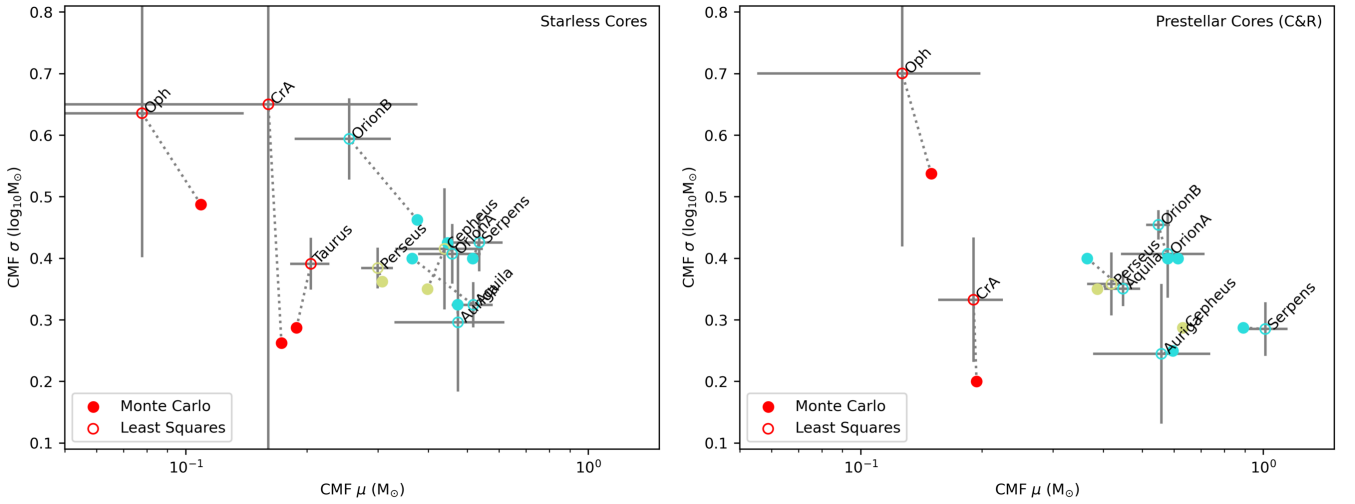


Figure E16. Comparison between the CMF properties (peak mass, μ , and width, σ) determined from LS and MC methods for each cloud complex. Left: starless cores. Right: prestellar (C & R) cores. In both panels, open circles indicate the best-fit LS values, while closed circles indicate the most probable MC values. Cloud complexes are colour-coded by their distance range.

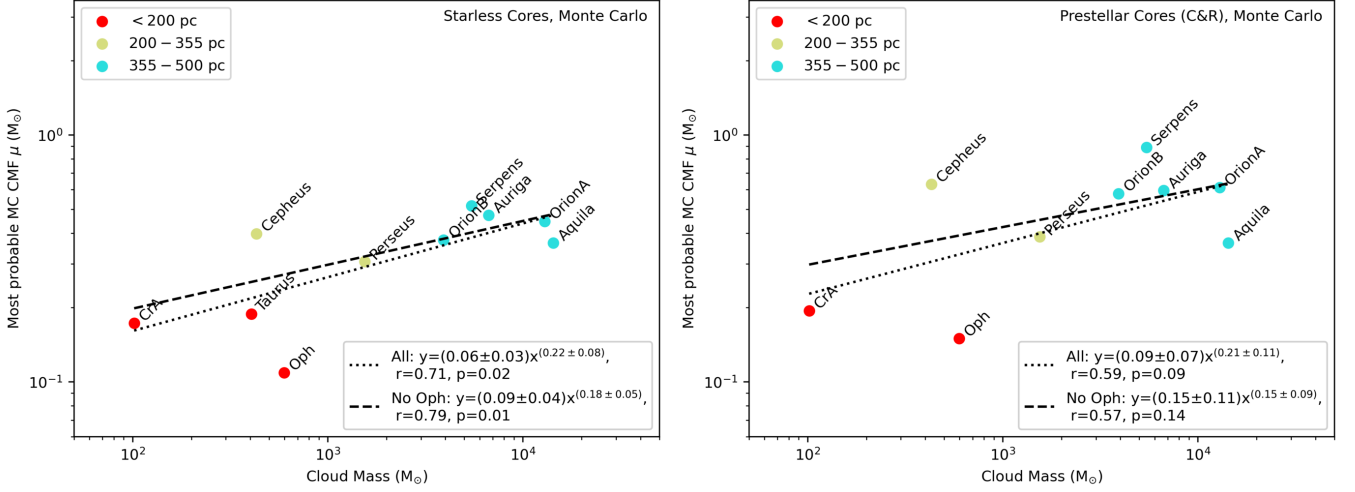


Figure E17. The peak masses of the starless and prestellar CMFs as a function of cloud complex mass, determined using Monte Carlo modelling. Left: starless CMFs. Right: prestellar CMFs. Dotted line shows the power-law model producing the best fit to all data points; dashed line shows the power-law model producing the best fit to the data points with Ophiuchus, which has a notably low peak mass, excluded. Data points are colour-coded by their distance range.

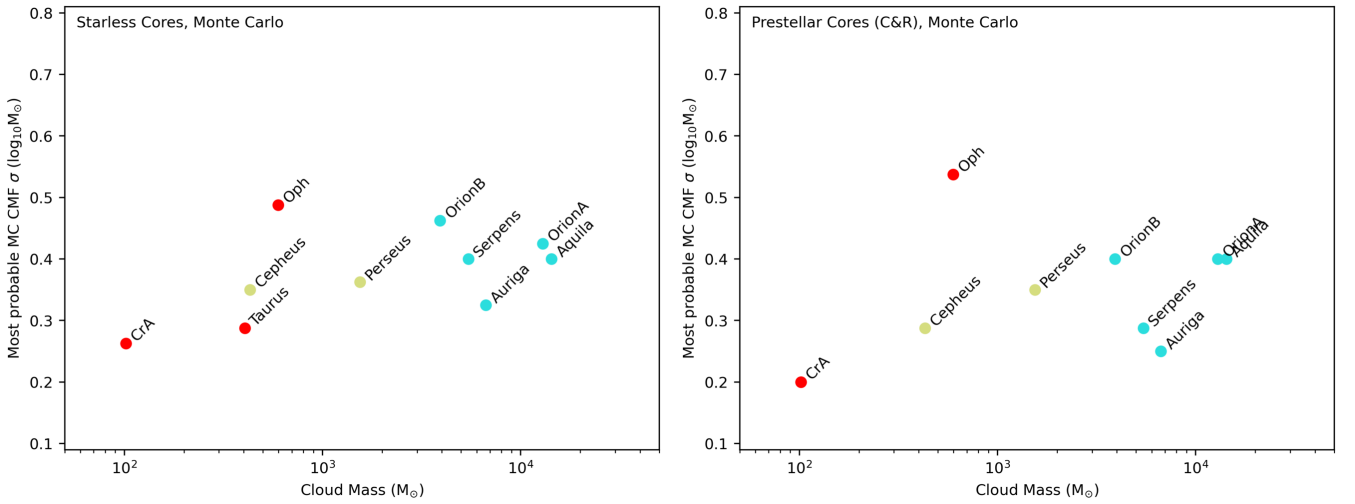


Figure E18. The width of the starless (left) and prestellar (right) CMFs as a function of cloud complex mass, determined using Monte Carlo modelling. Data points are colour-coded by their distance range.